EXTRAGALACTIC X–RAY
ASTRONOMY
WITH GINGA

Jacqueline Anne Butcher

I

UMI Number: U538948

UMI U538948

ProQuest LLC
789 East Eisenhower Parkway
P.O. Box 1346
Ann Arbor, MI 48106-1346

Declaration

I hereby declare that no part of this thesis has been previously submitted to this or any other university as part of the requirement for a higher degree. The work described herein was conducted by the undersigned except for contributions from colleagues and other workers who are acknowledged in the text.

Jackie Butcher

October 1994.

This thesis is dedicated to my parents.

Contents

Apologia pro these meo

This is a thesis in two parts: the first half is concerned with fluctuation studies of the 2–11 keV X–ray background and the second describes observations of clusters of galaxies. These two topics are not closely linked, hence the existence of this prequel to explain to the reader the structure of the thesis. The most obvious common ground between the two parts is that all the data were taken with the Large Area Counters on board the *Ginga* (1987-1991) satellite. Thus this is a thesis describing the analysis of non-imaging, hard (2-20 keV) X–ray observations. The scientific nature of the two topics covered is such that this thesis touches on all areas of extragalactic X–ray astronomy.

The above description may seem to beg the question "what is the contribution of clusters to the XRB ?". This question *is* addressed in Chapter 4, but it should certainly not be regarded as the central aim of this work. The two scientific topics were initially proposed as separate, the analysis was undertaken as two independent projects, liasing with two different groups of collaborators and the final work should be viewed in this light.

The structure of the thesis is simple. The first chapter describes the *Ginga* satellite and data reduction techniques. This chapter is followed by two sets of (Introduction, Data, Implications) chapters which deal with the XRB and clusters respectively and a final (brief) summary chapter.

Unless stated otherwise, all the results in this thesis have been derived assuming a Hubble constant $H_0 = 50 \, \text{km} \, \text{s}^{-1} \, \text{Mpc}^{-1}$ and a decceleration parameter, $q_0 = 0.5$.

Chapter 1

The Ginga satellite and data reduction system

1.1 The *Ginga* satellite

The third Japanese X–ray astronomy satellite *Ginga* (known before launch as Astro-C) was launched from the Kagoshima space centre on 5th February 1987 and re-entered on 1st November 1991 after the decay of the orbit. The orbital inclimation was 31° and the initial apogee and perigee were 670km and 500 km respectively. The satellite payload carried 3 scientific instruments: an all sky monitor (ASM); a gamma-ray burst detector (GBD) and the UK built large area proportional counter (LAC). This thesis only includes analysis of data from the latter instrument. A full description of the *Ginga* satellite is given in Makino *et al.* (1987), and descriptions of the other instruments can be found in Tsunemi *et al.* (1989) and Murakami *et al.* (1989). Figure 1.1 shows a schematic diagram of the satellite. *Ginga* was three-axis stabilised; movement in the spacecraft X-Y plane (defined as parallel to the solar panels) was controlled by a momentum wheel (slewing rate $\sim 15°\mathrm{min}^{-1}$) while three magneto-torquers manoeuvred (at $\sim 4°\mathrm{hr}^{-1}$) and stabilised the Z-axis (perpendicular to the X-Y plane). Power
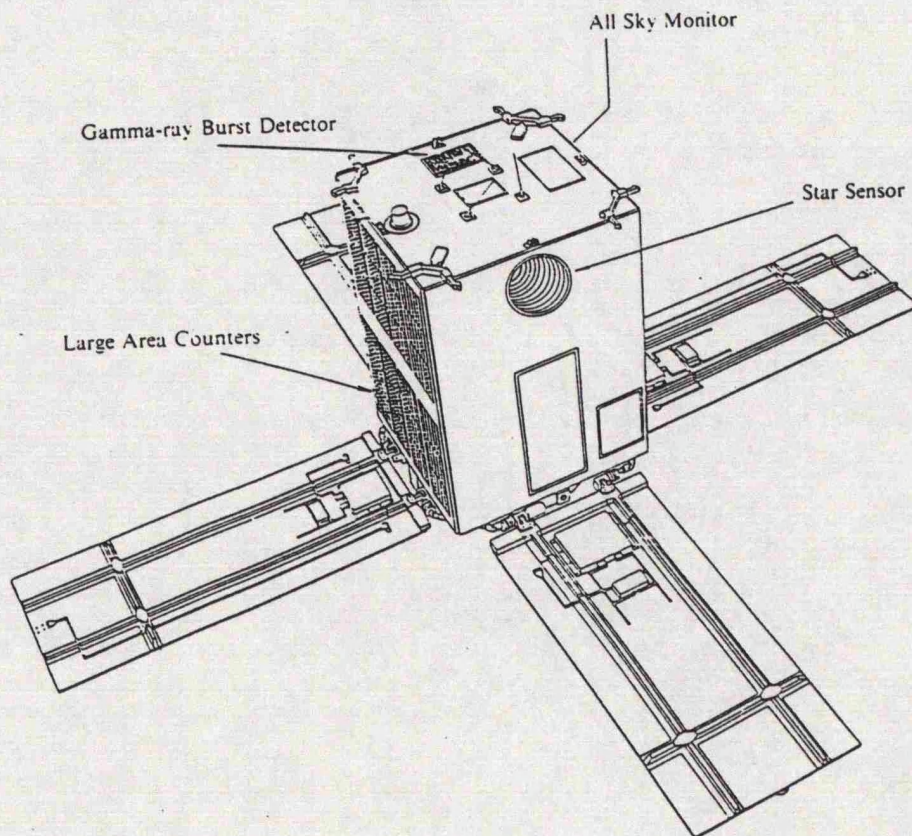
Figure 1.1: Schematic diagram of the *Ginga* satellite taken from Turner *et al.*
1989.

constraints required the angle between the Z-axis and the sun to be less than
135°; ideally this angle should be greater than 90° to avoid scattered solar X–
rays entering the LAC - this constraint was not always obeyed during operation.

The main difference between the *Ginga* satellite and the previous, comparable
X–ray mission *EXOSAT* was the orbit; *EXOSAT* was launched into an highly
elliptical orbit with a 90.6 hour period while *Ginga* was placed into a low earth

orbit with an initial period of $\sim$ 90 minutes. The advantages of a low earth orbit are reduced background levels due to increased shielding of cosmic ray events by the earth's magnetic fields. This effect is to some extent negated by the daily passage of the orbit through the earth's radiation belts in the region of the South Atlantic Anomaly (SAA), as discussed later. Low earth orbits are also disadvantageous for timing studies as sources are occulted by the earth for approximately 1/3 of each orbit. However this does not affect the sources discussed in this thesis.

1.2   The *Ginga* LAC

The LAC on board *Ginga* consisted of 8 identical, sealed proportional counters each with an effective area of $565\,\mathrm{cm^2}$, giving a total effective geometric area of $\sim 4500\,\mathrm{cm^2}$. Each detector had its own anti-coincidence and internal guard monitors and each had a co-aligned stainless steel collimator yielding an elliptical field of view ($1° \times 1.8°$) FWHM. This large field of view was necessary due to the modest pointing stability of the satellite. The collimators were coated with silver to reduce data contamination by iron K fluorescent lines, but this did introduce a silver K fluorescent line at $\sim$ 22 keV. The detector bodies were made from stainless steel with a 62μ beryllium window. Efficient anti-coincidence rejection techniques were primarily responsible for the low internal background rate in the LAC. The detector assembly was shielded by 0.2mm of tin.

1.2.1   Proportional counters

Each detector was separated into two layers known as 'top' and 'mid' which were sensitive to X-rays in the energy bands 1-37 keV and 8-37 keV respectively. The mid layer had twice the gas depth of the top layer. The counter gas was a mixture of 75% argon, 20% xenon and 5% CO_2 at 1.86 atmospheres. Xenon provides increased stopping power for higher energy X-rays but increases the internal

background - the xenon content was thus kept to the smallest possible, efficient level. The energy resolution was 18% at 6 keV and varied as $\Delta E/E \sim 40 E^{-0.5}$ %.

1.2.2   Data modes

After the signal pulses were digitised the pulse height data were analysed into one of 64 channels. The last 32 channels were compressed by a factor 2 for storage and transmission, giving a total of 48 energy channels. The on board computer had several data modes which provided trade offs between temporal and spectral resolution as described below:

- **MPC1**   48 channel energy resolution from both top and mid layers in all 8 detectors. Separation of top and mid layers gives improved signal to noise for weak sources. This mode gives the lowest time resolution.

- **MPC2**   The detectors are grouped in two groups of four; top and mid layer data are combined for each group. There are 48 pulse height channels.

- **MPC3**   Top and mid layer data from all 8 detectors are combined and there are 12 energy channels.

- **PC**   This mode offers the highest timing resolution with 2 very broad energy channels.

There were three different data acquisition rates; Table 1.1 summarises the characteristics of the LAC in different modes and at different bit rates. The main restriction to the use of high bit rate data was the capacity of the on board bubble memory, which confined very high resolution timing studies to orbits when the satellite was in contact with the ground station. All the data described in this thesis were collected with the LAC in MPC1 mode.

Mode	Energy Channels	Time Resolution			Detectors
		Low	Medium	High	
MPC1	48	16s	4s	500ms	8 detectors, 2 layers
MPC2	48	2s	500ms	62.5ms	2 groups of 4 detectors
MPC3	12	250ms	62.5ms	7.8ms	1 group of 8 detectors
PC High	1	62.5ms	15.6ms	1.9ms	2 groups of 4 detectors
PC Low	1	31.3	7.8ms	0.98ms	2 groups of 4 detectors

Table 1.1: Data modes and timing resolution

Count to flux conversion

For an incident spectrum of the form $f_\nu \alpha \nu^{-\alpha}$, with $\alpha = 0.8$, 1 LAC $\mathrm{ct\,s^{-1}}$ corresponds to $2.4 \times 10^{-12}\,\mathrm{ergs\,s^{-2}\,cm^{-2}}$. in 4–12 keV.

1.3   The LAC background

Both the magnitude and the spectrum of the LAC background varied with time in a complex fashion. The main variations were caused by the daily passage through the SAA. Figure 1.2 shows the 2-10 keV light curves in the top and mid layers plus the SUD rates (see below) of a 2 day long blank sky observation made in September 1987. The background increases at times t=60,000s, corresponding to orbits which pass through the SAA, and then decreases exponentially. Due to the position of the ground station contact with the satellite always occured during orbits with high background.

While the satellite orbit was nearly circular (initially $e \sim 0.01$) the altitude of passage through the SAA varied on a 37 day cycle. The particle flux in the SAA depended on the altitude and so the LAC background also exhibited a 37 day periodicity.

The two main sources of the LAC background were the diffuse X–ray background
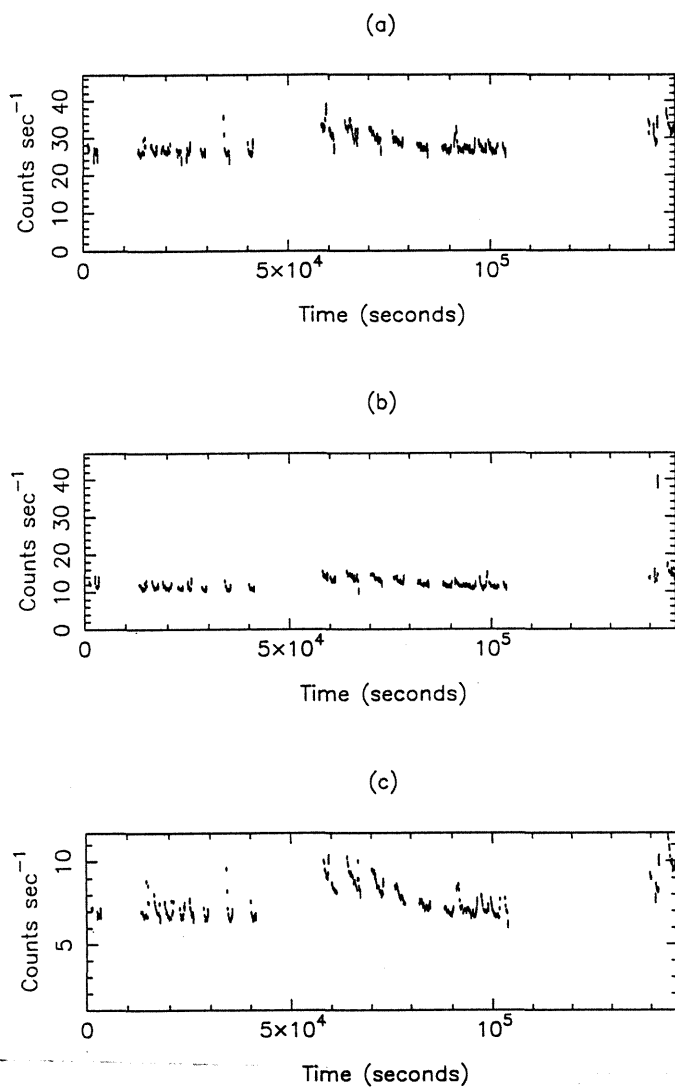
Figure 1.2: Panels a) and b) show the 2-10 keV light curves for a long *Ginga* blank sky pointing in the top and mid layers respectively. Panel c) shows the SUD rate (see below) for the observation.

8

(XRB) and background due to charged particles. Other sources of X–rays were the sun and the bright limb of the earth; the latter was easily removed by requiring the Y-elevation of the satellite from the earth's limb to be > 6°. The remaining three effects are summarised below; a more comprehensive description can be found in Hayashida *et al.* 1989.

Solar Contamination

For values of $\beta < 90°$ solar X–rays could enter the collimator and be reflected into the LAC. These scattered solar X–rays have a very soft spectrum and are easily identified. Sunlit data for $\beta < 90°$ were usually excluded from further analysis although for some pointing directions certain of the LAC detectors are in the shadow of the solar panels and are shielded from solar contamination. In this case all the data from the shielded detectors may be analysed in the normal way.

Diffuse X–ray background

The diffuse extragalactic X–ray background (XRB) contributes $\sim 15 \, \text{ct s}^{-1}$ to the LAC background between pulse height (PHA) channels 4 and 20 (2 to 11 keV). A major residual source of background uncertainty is due to the fluctuations in the XRB. This effect is described in much more detail in Chapters 2 and 3.

Particle background

The particle background is due to the solar wind, cosmic rays and energetic particles trapped in the earth's geomagnetic field. While most of these events could be rejected by anti-coincidence techniques, they could give rise to secondary processes which were more difficult to discriminate against. Interactions between particles and the detector walls may produce gamma rays or may lead to the

9

formation of radioactive isotopes which then decay, again producing gamma rays. These gamma rays may Compton scatter with the detector gas and be detected. At least 3 radioactive components have been identified in the LAC background with e-folding times of 12.5 hr, 1 hr and 8 minutes. A further 0.5 hr period has also been noted (Williams, private communication) but the origin of this is unclear. The LAC was switched off during the satellite passage through the SAA so the 8 minute decay is unimportant in background estimation.

There was no facility for simultaneous monitoring of the off-source background but a number of auxiliary housekeeping (HK) count rates from the LAC and other instruments aboard *Ginga* provided indirect information on the radiation environment of the satellite. The HK parameters relevant to background estimation are now summarised, again Hayashida *et al.* give a fuller description.

- **SUD** 'Surplus to Upper Discriminator'. This measures the number of X–ray like events with energies above the upper discriminator (usually set at 24 keV). To first order the SUD rate scales linearly with the background.

- **SOL2** This is the count rate from the solid state electron detector which is used to automatically switch off the LAC as *Ginga* enters the SAA.

- **PI MONI** The count rate for the LAC anode wires not directly illuminated via the collimator. Under normal circumstances the PI MONI rate scales linearly with SUD.

- **COR** The cut off rigidity is the momentum per unit charge that a particle must have in order to penetrate to a given point in the earth's magnetosphere, hence the background count rate is anticorrelated with COR. The parameter is calculated from a model of the earth's magnetic field and the satellite orbit.

10

Parameter	Selection Criteria
β, SUNSHINE	If $\beta < 90°$ then usually SUNSHINE = 0 (see text)
SUD	< 14
PI MONI	less than 3σ from best fit line in the SUD–PI MONI plane
COR	10–20
SOL	< 15
YELEV	> 6°

Table 1.2: Data selection criteria.

1.4   Data Reduction

A consistent data selection procedure, summarised in Table 1.2 was followed during data analysis. Regions of low COR rate were excluded, in order to avoid cosmic ray contamination. During the initial data sorting the SUD rate was required to be less than 15 ct/s for both source and background observations. Wherever possible final source spectra were prepared from non-contact orbit data only (*i.e.* lower SUD rates and fewer background counts). Soft electron events were eliminated by rejecting data points lying further than 3σ from the best fitting correlation in the SUD-PI MONI plane. Since neither clusters of galaxies nor the XRB exhibit time variability it was possible to further clean the data by using the SUD-LAC count rate correlation.

1.4.1   Background Modelling

A typical (and ideal) *Ginga* observation included one day spent pointing at the source and one day pointing at an adjacent region of 'blank' sky. These blank sky

observations were used to create a model of the background which in turn was used to reconstruct the background count rates during a source observation. The parameters of this model are the relevant auxiliary count rates each of which is associated with a spectral form. The model used for estimating the background is

$$C(E,t) = F_1(E) + \sum_{i=2}^{n} P_i(t) \times F_i(E) \tag{1.1}$$

where, C(E,t) = LAC count rate due to the background,

$F_1(E)$ = constant (diffuse) background spectrum + mean particle background,

$F_i(E)$ are the spectra of the various time dependent components of the background and P_i are the HK parameters with which each $F_i(E)$ scales. The P_i may be either count rates such as SUD and PI MONI or calculated parameters such as COR and parameters describing the radiation caused by the passage through the SAA.

During the mission lifetime there evolved several different ways of modelling the background. In particular there were two different ways of modelling the radioactive decays. One method, described in Hayashida *et al.* (1989) and widely used in Japan, was to use the Mid layer count rate between 2–10 keV as a measure of the scaling of the radioactive components. The detection efficiency for X–rays in the mid layer was low in this energy range, but was still sufficient to prohibit this method for strong sources. This method was not used in the work described in this thesis. The other approach involved calculating pseudo HK parameters describing the scaling of the radioactive components, using a knowledge of their half-lives.

There are also several different approaches to determining the spectral coefficients of the background. Method I as described in Hayashida *et al.* (1989) uses a blank sky pointing immediately before or after the source observation. This has the advantage that background variations due to the 37 day cycle may be ignored, hence estimation of the particle background is improved. The blank sky observation should be at least 18 hours long in order to model the 12.5 hour decay; in practice it was often found that background observations adjacent in time to

12

the source observation were inadequate. In this case method II in Hayashida *et al.*
(1989) was employed; this involved fitting background observations taken over a
period of several months. The 37 day periodicity of the radio-active components
must be modelled – such modelling requires many blank sky observations covering
all phases of the orbit. The background observations used were taken from the
background database described in Chapter 3. In the case of fitting N files the
model used is

$$C(E,t) = F_1(E) + F_2(E) + \cdots F_N(E) + \sum_{i=N+1}^{i=N+n} P_i(t) \times F_i(E) \qquad (1.2)$$

The time dependent components are related to the same HK parameters as in
method I. The time independent components include the diffuse background in-
tensity at each of the different pointing positions; these could be averaged to
give an estimate of the mean diffuse background level. This method generally
gives less good results for the mid layer, but has the advantage that the effect of
fluctuations in the XRB are minimised. This latter method was used for most
of the observations presented in this thesis. An intermediate method (which will
be referred to as method I.5) was also sometimes used. Two or more blank sky
observations, close in time to the source observations are fitted simultaneously
without any attempt to model the 37 day periodicity. In fact, since clusters of
galaxies are not time-variable X–ray sources it is sometimes possible to include
the source observation in this fitting procedure but to omit the relevant constant
component which will represent (source+diffuse background spectrum) from the
averaging.

1.4.2 Aspect Correction

The LAC collimator was calibrated early in the mission by scanning across the
Crab Nebula. A grid of transmission coefficients for off-axis positions was com-
puted from this slew data which could be used to renormalize off-axis point source
observations. At lower energies the transmission is spread out in the X-axis due to
reflection of off-axis X–rays from the collimator surfaces. This effect introduced

an energy dependence into the transmission efficiency.

Accurate aspect correction for observations of nearby clusters of galaxies would require an accurate knowledge of the surface brightness distribution out to 1° and any attempt to correct for the energy dependent reflection effect must presuppose some particular temperature-radius distribution. For these reasons it was not felt appropriate to attempt full aspect correction of the data and most spectral analysis was done on the original pulse height data (individual exceptions are discussed in more detail in the text). Derived cluster parameters such as luminosity were corrected for the effects of off-axis response.

1.5   Spectral Analysis

An example of a background subtracted pulse height spectrum is shown in Figure 1.3. It is not possible to derive the form of the incident X–ray photon spectrum by simply deconvolving the pulse height spectrum with the instrument response since no unique solution exists. Instead a trial photon spectrum, characterised by a number of free parameters, is convolved with the instrument response to give a predicted pulse height spectrum which is compared to the data. The goodness of fit is measured by the χ^2 statistic (Bevington 1969) and the parameters are adjusted iteratively until a minimum in the χ^2 surface in the parameter space is found. Errors are calculated by searching the parameter space for values which give the appropriate change in χ^2. This change depends on the number of parameters in the model (Lampton, Margon & Bower 1976) and may be reduced by considering one or more parameters to be 'of no interest'. The errors quoted in this thesis are 68 % confidence for one uninteresting parameter unless otherwise stated. Such errors are larger than the commonly quoted $\chi^2 + 1$ which underestimates the joint errors when several free parameters are fitted (Lampton, Margon & Bower 1976), and thus provide conservative upper limits to the 1σ errors.

Mid

Top
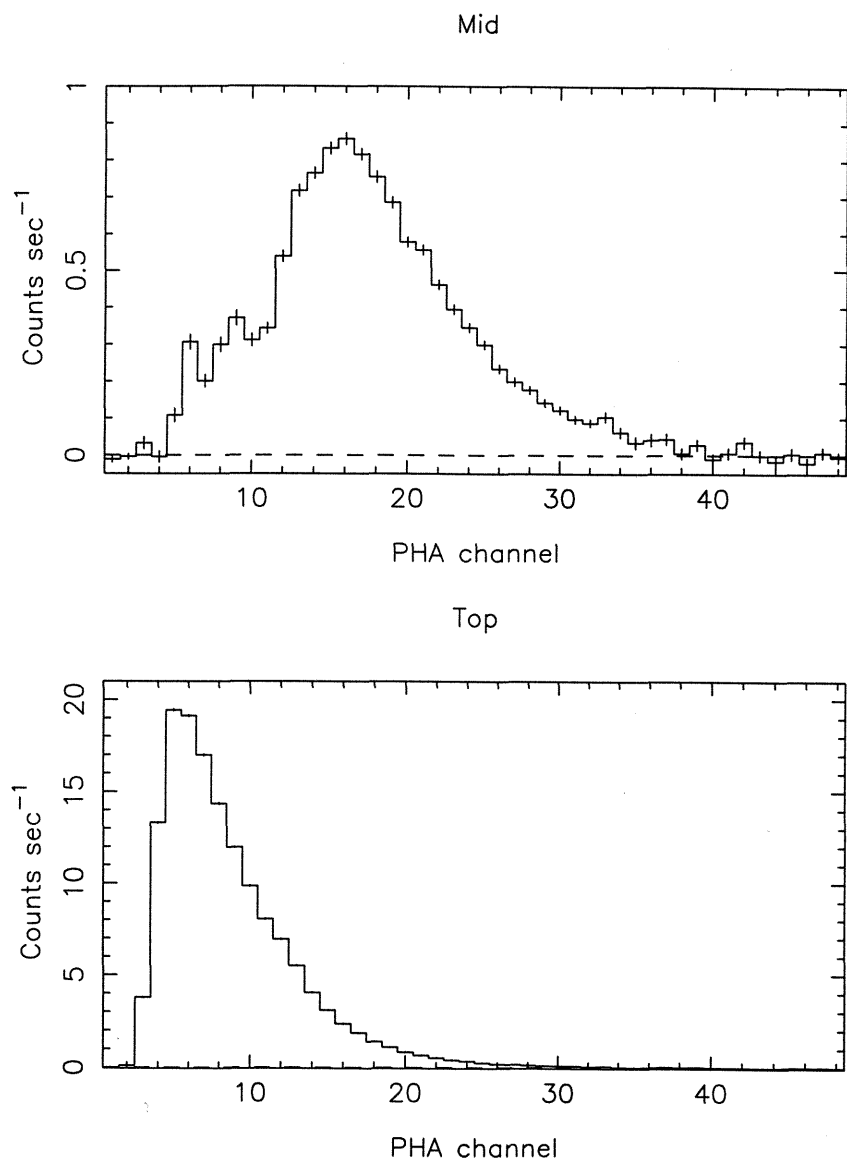
Figure 1.3: An example of a background subtracted pulse height spectrum from the *Ginga* LAC. The source is the Coma cluster. The upper panel shows the count spectrum from the mid layer of the LAC and the lower panel shows the count spectrum in the top layer.

Chapter 2

The X–ray Background

Overview

The known properties of both the soft and hard X–ray backgrounds are described and theories for their origin are reviewed. The *Ginga* spectrum of a starburst galaxy is presented and shown not to resemble that of the XRB.

2.1 Introduction

The discovery of the X–ray background (Giacconi *et al.* 1962) predates that of the microwave background (Penzias & Wilson 1965). The origin of this latter radiation has an almost universally accepted explanation as the relic radiation from a hot big bang; there is no such consensus of opinion over the X–ray background and the origin of the bulk of the emission at energies greater than 2 keV remains unknown. After the discovery that extra-galactic objects such as AGN and clusters of galaxies were X–ray emitters, it became apparent that at least some of the XRB was contributed by discrete sources. The main goals in studying the XRB are to understand the spatial density and distribution and the spectra of these discrete sources and to discover how much (if any) of the background is truly diffuse. The most direct approach to answering this question is to image the sky

16

for sufficiently long to resolve as many point sources as possible. The imaging detectors on *EINSTEIN* and ROSAT have made possible the direct resolution of at least 30% of the soft (0.5-2 keV) X–ray background (Griffiths *et al.* 1988, Shanks *et al.* 1991). Above 3 keV direct imaging of sources has not been possible, due to the lack of imaging X–ray optics. Most of our knowledge of the XRB between 2-500 keV comes from the all sky survey carried out by the *HEAO-1* satellite which carried experiments specially designed to study the spectrum and isotropy of the XRB, although the large field of view of the detectors limited the angular resolution for source detection. The factors above have led to a situation where the spectrum of the extragalactic XRB is known with great precision above 3 keV (below this energy the galactic contribution becomes more substantial and is difficult to quantify), while the point source contribution may be most accurately estimated in the soft band. Thus it is natural to divide the XRB into two energy bands, from 1 to 3 keV and 2-3 to 200 keV (with this latter part being further divided at about 10 keV). Indeed recent results suggest that the origins of the major part of these backgrounds may not be the same.

Discrete source contributions to the XRB are described in terms of their source counts or $N(S)$ relationship. The relevant mathematical details are given in the appendix.

The next sections review our knowledge of the XRB.

2.2   2–10 keV band

2.2.1   Resolved sources

The Ariel V, Uhuru and *HEAO-1* satellites performed all sky surveys from which the form of the 2–10 keV source counts for bright, extragalactic sources could be deduced (Warwick & Pye (1978), Schwartz (1979) and Piccinotti *et al.* (1982), respectively). The inferred $N(S)$ relationships for all three sets of data were

consistent with each other and with the Euclidean form, although the best fit values of γ were slightly steeper than -2.5. In particular the source counts were consistent with

$$N(S)dS \approx 2.2^{+0.3}_{-0.2} \times 10^{-15} S^{-2.5} dS \, \text{sr}^{-1} \qquad (2.1)$$

down to a limiting sensitivity of $3.1 \times 10^{-11} \text{ergs s}^{-1} \text{cm}^2$ (Piccinotti *et al.* 1982).

2.2.2 The unresolved background

Although data from earlier satellites (Ariel V, Uhuru) were used to study the XRB, it was the *HEAO-1* satellite which provided the base for much of our current understanding (or lack of it!) of the hard XRB, so it is relevant to briefly describe this satellite. The properties of the 2–10 keV background are then described.

HEAO-1 was launched in 1977 and carried experiments specifically designed to separate the X–ray sky background from the internal background. The A2 (Cosmic X–ray) experiment, described in more detail by Rothschild *et al.* (1979), consisted of 6 gas proportional counters which, between them, covered the energy range 0.1-60 keV. Efficient cosmic-ray rejection techniques were employed. The most important feature of the detectors for observing the XRB was that the detectors were dual collimated; each had a field of view of $3° \times 3°$ while the secondary field of view was either $3° \times 6°$ or $3° \times 1.5°$. Since the diffuse XRB flux scales with solid angle, while the internal background remains constant, the XRB spectrum may be calculated by subtracting the raw spectrum in the small field of view from the raw spectrum in the large field of view.

Gas filled proportional counters have little stopping power for X–rays above ~ 60 keV and the higher energy A4 experiment employed solid scintillation detectors. The internal background was reduced by anti-coincidence techniques.

Brightness

The intensity of the X–ray background at 10 keV is $3.2\,\mathrm{keV\,keV^{-1}\,cm^{-2}\,s^{-1}\,sr^{-1}}$ (Marshall *et al.* 1980). This is only a small fraction of the background intensity measured in the microwave band.

Spectrum

Below 10 kev the XRB spectrum is consistent with a power law spectrum with $\alpha = 0.4$, but this is too flat at higher energies. Between 2–10 keV this is flatter than the 'canonical' photon spectral index of 0.7 for AGN (Turner and Pounds 1989) and this is the origin of the much discussed spectral paradox. The spectrum of the XRB between 2-60 keV, measured by the A2 experiment is very well fit by an optically thin thermal bremsstrahlung continuum model with kT=40 keV (Marshall *et al.* 1980). Data from the A4 experiment show that this model is appropriate to energies ~ 100 keV (Gruber *et al.* 1984, 1992). No known X–ray sources have spectra of this form at the present epoch. Figure 2.1 shows the spectrum of the X–ray and γ–ray backgrounds as measured by HEAO-1 and rocket instruments.

Above 100 keV up to a few hundred keV the spectrum is much steeper and can be fit to a power law with $\Gamma \simeq 0.7$ (Gruber 1992).

Isotropy

• **Large scale**

At energies greater than 3 keV, at high galactic latitudes, the galactic contribution to the background is small and significantly softer (characteristic temperature 9 keV) than the total background (Iwan *et al.* 1982). After this is removed the XRB is essentially isotropic at large angular scales; the largest residual anisotropy, with intensity of about 0.5% of the XRB intensity, is a dipole (at 95% confidence)
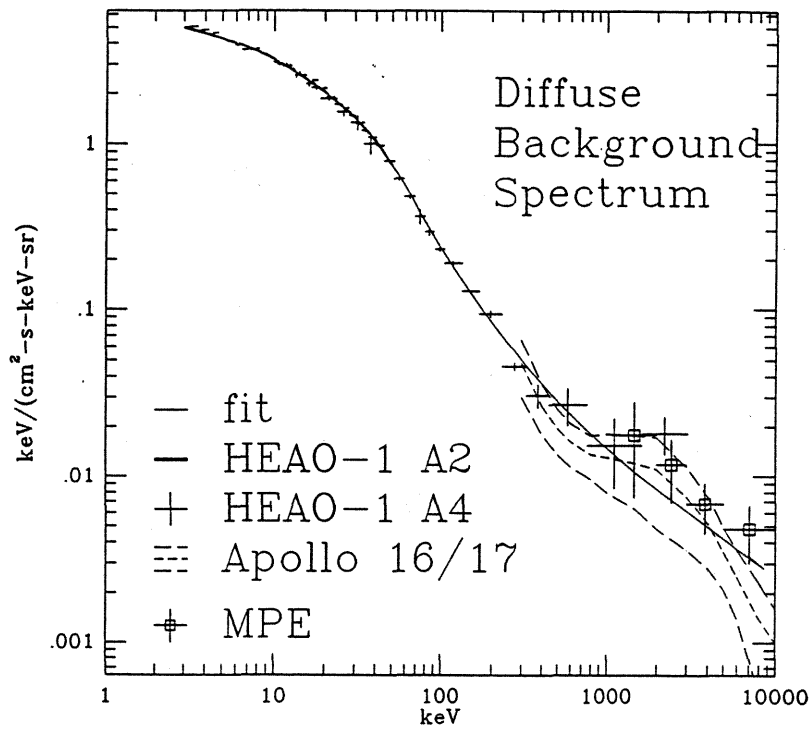
Figure 2.1: Energy spectrum of the hard, diffuse background. The data is from the HEAO-1 satellite and from rocket missions. (Taken from Gruber (1992)).

centred on galactic coordinates $l = 282°$, $b = +30°$. If interpreted as due to the Compton-Getting effect then the direction and inferred velocity are not inconsistent with those derived from the microwave background dipole (see Strukov & Skulachev (1988) for a review of the microwave band dipole). However, given the relatively large directional uncertainties, this large scale anisotropy is also consistent with an explanation based on a possible component of the extragalactic background associated with the Supergalaxy (Boldt 1987). Mushotzky & Jahoda (1992) report an enhancement in the XRB in the direction of the Great Attractor (although a galactic origin is not ruled out). They also point out 3 areas of apparently low background intensity in the south of the sky, 2 of which are 'probably' associated with voids in the ACO distribution of clusters.

- **Fluctuations**

The small scale isotropy of the XRB is limited by surface brightness fluctuations due to discrete sources. Poisson fluctuations in the number of discrete sources per beam cause intensity fluctuations greater than those predicted from pure photon noise. The study of such fluctuations was pioneered at radio wavelengths. The technique makes possible the statistical study of sources below the flux limit of a survey (Scheuer 1974, Condon 1974). The shape of the fluctuation distribution depends on the index γ of the number-flux relation for the sources, while the width of the fluctuation distribution about the mean is determined by the effective solid angle. The fluctuation analysis technique is described more fully in the appendix. It has been applied to Uhuru data by Fabian (1975) and to Ariel V data by Warwick & Pye (1978). Shafer (1983) performed a very comprehensive study of XRB fluctuations using the *HEAO-1* A2 data; his results provided the best constraints on the extragalactic source counts until until the study presented in this thesis.

The fluctuations measured by HEAO-1 are consistent with those predicted by extrapolating the log N–log S relation for the bright sources (Piccinotti *et al.* 1982) down to lower flux levels (Shafer 1983).

• ACF

The isotropy of the XRB may also be examined by analysing the auto-correlation function (ACF) of the fluctuations. Persic *et al.* (1989) found that the ACF of the HEAO-1 A2 data is compatible with zero on all scales from $3° - 27°$. More recently, Mushotzky & Jahoda (1992) reported the first detection of a signal in the ACF at these energies; $\omega(\theta) \simeq 3 \times 10^{-5}$ on scales of $10° - 18°$ at 99% confidence.

2.3   The soft X–ray background

Until the launch of *ROSAT* in June 1990, most of the data on the XRB below 3 keV was from the HEAO-2 satellite, renamed as the *EINSTEIN* Observatory after its launch in 1978. The satellite carried an imaging X–ray telescope and hence provided opportunities to resolve discrete sources with vastly improved angular resolution. The two detectors relevant to the study of the XRB were the Imaging Proportional Counter (IPC) and the High Resolution Imager (HRI). The positional accuracy of the IPC was approximately 1 arcminute while for the HRI it was $\sim$ 5 arcseconds. Both detectors were equally sensitive to soft, point sources but the HRI was less sensitive to extended and harder sources. A more complete description of the satellite is given in Giacconi *et al.* (1979a).

2.3.1   Resolved sources

The original deep surveys carried out by *EINSTEIN* were in the directions of Draco and Eridanus using both the HRI and IPC. Giacconi *et al.* (1979b) reported the detection of 43 sources but a complete optical identification programme was not possible and the identities of most of these sources remained unknown. A reanalysis of the deep survey data, using improved flat fielding techniques, only detected 11 of the original 43 sources plus one additional source (Hamilton *et al.* 1991).

A deep survey carried out in the Pavo region detected a total of 24 sources with the HRI and IPC (Griffiths *et al.* 1983, Griffiths *et al.* 1988). Fourteen of these objects were found to be quasars with a mean redshift of 0.9 and a mean absolute visual magnitude $M_v \sim -25$. This puts them on the QSO side of the $M_b = -23$ division between Seyferts and QSOs defined by Schmidt & Green (1987).

The Extended Medium Sensitivity Survey (EMSS) (Gioia *et al.* 1990a) is an extension of the original medium sensitivity survey of Maccacaro *et al.* (1982). It contains all the serendipitous sources detected in *EINSTEIN* IPC fields at high galactic latitude ($|b| > 20°$). It covers an area of 780 square degrees and contains 835 sources. The sensitivity level varies between 5×10^{-14} and 10^{-11} ergs s^{-1} cm^{-2} in the energy band 0.3–3.5 keV. Optical identification work on the sample is now complete and the sample composition is shown in Table 2.1.

class of source	number
AGN (including BL Lacs)	55.4%
Clusters of galaxies	12.2%
Normal Galaxies	2.5%
Stars	25.8%

Table 2.1: Composition of the *EINSTEIN* EMSS.

Shanks *et al.* (1991) obtained a 27000 second ROSAT PSPC exposure of a field containing optically studied UVX quasars. Combining these results with an observation of another, similarly selected field, they detect ~ 50 quasars out of a total of ~ 85 sources in the inner regions of the detector. The mean redshift of the quasars is 1.5, significantly higher than that for the AGN in the EMSS.

Hasinger *et al.* (1991) have analysed 8 high galactic latitude ROSAT fields and have found that up to 50% of the XRB between 1.2-2 keV is directly resolved into sources. Although optical identifications for the sources are not available, the authors argue that contamination by galactic sources should be less than 10% and that most of the remaining sources are likely to be AGN.

2.3.2 The unresolved background

Spectrum

The spectrum of the XRB below 3 keV is poorly determined; the galactic contribution is substantial and difficult to remove. Micela *et al.* (1991) analysed many IPC fields and concluded that the XRB intensity is a factor of ~ 2.5 above the extrapolation of the $\alpha = 0.4$ power law seen between 2-10 keV. Wu *et al.* (1991) obtained similar results by analysing IPC fields using a different procedure.

Fluctuation Analysis

Hamilton & Helfand (1987) analysed fluctuations in IPC fields on arcminute scales. They showed that the source counts must flatten below the Euclidean and that there must exist a very smooth component of the XRB corresponding to a source density of $>\sim 5 \times 10^3 \mathrm{deg}^{-2}$. These results were confirmed by Barcons and Fabian (1990). Barcons & Fabian (1989) performed an autocorrelation function analysis on these data and found no evidence for any positive signal of cosmic origin.

2.4 The origin of the XRB

2.4.1 Diffuse emission

The discovery of the thermal form of the spectrum of the XRB prompted much interest in models where the XRB is due to optically thin, thermal bremsstrahlung from an hot intergalactic medium (IGM), (see *e.g.* Cowsik & Kobetich 1972, Field & Perrenod 1977, Guilbert & Fabian 1986 and Barcons 1987). In these models the gas is heated (by supernovae winds or by explosions) at redshift z and then cools by adiabatic expansion. One immediate problem with these mod-

els is that the residual background (after subtracting the integrated contribution from known classes of resolved sources) is not necessarily thermal but is even flatter than the total XRB spectrum (see *e.g.* Boldt 1987, Giacconi & Zamorani 1987). There are also enormous energetic problems associated with models of this type. Setti (1990) estimates that each galaxy needs to donate 10^{64} ergs to the IGM. These energy requirements may be somewhat alleviated by requiring the heating to take place at higher redshifts but another serious problem is the sheer mass of gas involved. The IGM would have to contain at least 25% of the closure density of the universe, in contradiction with standard hot big bang nucleosynthesis theories which require $\Omega_b \sim 0.016 h^{-2}$ in order to explain the observed light element abundances (Olive *et al.* 1990). This constraint may be relaxed by requiring that the gas be clumped; hot, dense blobs sitting in a hotter, but less dense medium. This would produce fluctuations in the XRB (Barcons & Fabian 1988) and would also be expected to distort the Wien region of the microwave background through inverse Compton scattering. The COBE satellite, launched in 1990, detected no such deviation from the blackbody spectrum (Mather *et al.* 1990) and finally ruled out hot IGM models as the source of the bulk of the XRB (they can contribute no more than 3%). Thus it seems most probable that the background is the integrated emission of unresolved sources.

2.4.2 Discrete source contributions

The known classes of extragalactic X–ray sources are galaxies (including starbursts), clusters of galaxies and AGN (including Seyferts and QSOs). Their possible contributions to the XRB are now considered in turn.

Normal galaxies

One of the most important discoveries by the *EINSTEIN* satellite was that elliptical galaxies contained substantial fractions of hot ($\sim 10^7$K) gas which emitted thermal bremsstrahlung at X–ray wavelengths. X–ray emission from spiral

25

galaxies comes mainly from hard X–ray binaries. For a comprehensive review
of the X–ray properties of normal galaxies see Fabbiano (1989) and references
therein. They are not generally strong X–ray emitters; the mean L_x to L_{opt} ra-
tio is 1.5×10^{-7} for spirals and 3.5×10^{-7} for ellipticals (Trinchieri & Fabbiano
1985). Giacconi & Zamorani (1987) use these ratios together with the deep op-
tical counts of Tyson (1984) to estimate that normal galaxies contribute $\sim 13\%$
of the XRB at 2 keV.

Clusters of galaxies

Hot gas in clusters of galaxies emits thermally at X–ray wavelengths. The spectra
are much softer than that of the XRB with typical temperatures between 2 and
12 keV (see Chapter 6). Strong, negative, luminosity evolution of clusters has
recently been discovered (Edge *et al.* 1990, Gioia *et al.* 1990b) which precludes a
significant contribution to the XRB from clusters at higher redshifts. Estimates
of the cluster contribution to the hard XRB are typically $\sim 2 - 10\%$.

AGN

Estimates of the AGN contribution to the soft X–ray background vary between
a minimum of 35% and 100% depending on the assumed X–ray source counts,
mean spectral index and evolution of the sources (Setti 1990, Schmidt & Green
1986). Many of these estimates, however, refer to the contribution of the sources
to the nominal monochromatic background at 2 keV. This value is calculated by
extrapolating the measured 3-40 keV bremsstrahlung down to 2 keV which may
not be appropriate given the upturn in the spectrum discussed above. Hence the
estimated contributions are too large in some cases.

Griffiths *et al.* (1988) find a minimum AGN contribution of 30% to the back-
ground at 2 keV (including the excess over the nominal extrapolation) while Mac-
cacaro *et al.* (1991) use the data on AGN from the EMSS to derive a contribution

of $\sim$ 36%, which is reduced if the true background exceeds the extrapolation. The *ROSAT* results discussed above show that the minimum AGN contribution in the soft band is 30%.

Danese *et al.* (1992) summarise the implications of ACF studies for the sources contributing to the XRB. The smoothness of the soft XRB implies that the QSOs must be less strongly clustered than clusters of galaxies and that sources clustered as strongly as galaxies can contribute no more than 60% of the soft XRB.

Above 3 keV the contribution of AGN to the XRB is more controversial. The pre-*Ginga* view of 2-10 keV AGN spectra was that of a simple power law spectrum, with energy indices tightly clustered around a mean on 0.7 (Mushotzky 1984b, Turner & Pounds 1989). *Ginga* observations of QSOs show that this mean is also appropriate for more luminous objects (Williams *et al.* 1992). This is much steeper than the XRB spectrum in the same energy range and has led various authors either to invoke the existence of a completely new class of X–ray source or to appeal to spectral evolution of AGN and require their spectra to have been harder in the past. Fabian, Canizares & Barcons (1989) conclude that AGN cannot produce more than $\sim$ 40% of the background between 2-10 keV, but even this size of AGN contribution still produced a significant spectral paradox as the residual background after subtracting the known spectra of the AGN contribution is even flatter. Schwartz & Tucker (1988) showed that if the mean AGN spectrum flattened above 10 keV then cosmological spectral evolution of AGN is not necessary and the 3-20 keV XRB may be reproduced by AGN with reasonable density evolution.

Ginga observations of AGN *have* detected a flattening of the hard X–ray spectrum of Seyfert galaxies. This is commonly interpreted as reprocessed ('reflected') emission from a thick slab of cold material (see *e.g.* Pounds *et al.* 1990, Nandra 1992). These reflected components seem to be less important in the spectra of high luminosity AGN (Williams *et al.* 1992). Fabian *et al.* (1990) have used Compton reflection models to fit the background spectrum up to the bump at a

few MeV, although the model underestimates the XRB intensity below 8 keV. Rogers & Field (1991) point out that the model can be adjusted to fit the XRB above 3 keV by steepening the unreflected incident power law, but this is at the expense of being able to extrapolate the fit up to MeV energies.

Danese *et al.* (1992) show that if low luminosity AGN contribute more than 50% of the hard XRB then their correlation length must be $r_o < 20\,\mathrm{Mpc}$.

Starburst galaxies

Recently there has been much interest in the possible contribution of starburst galaxies to the XRB (Griffiths & Padovani 1990). It has been suggested that the low metal abundance of starburst galaxies would reduce the opacity of massive X–ray binaries (MXRB) and increase the contribution of these sources to the total emission from the galaxy. In this case we would expect starburst galaxies to have hard X–ray spectra resembling those of MXRB (typically described by a thermal bremsstrahlung with kT > 15 keV). Griffiths & Padovani estimate that 20-50% of the 3-20 keV XRB may be produced by star-forming galaxies at epochs $z \sim 0.5 - 1$, and that many of these galaxies may be dwarf galaxies. A problem with this model is that the 2-10 keV spectra of nearby starburst galaxies do not appear to have this flat form. *Ginga* observations of NGC 253 and M82 have revealed spectra with kT $\sim$ a few keV (Ohashi *et al.* 1990). These authors conclude that hot gas emission (probably from supernova remnants) must dominate over that from MXRB.

The spectral results are confirmed by analysis of a *Ginga* observation of NGC 5408. This is a dwarf irregular galaxy with very low metallicity and enhanced starburst activity. It was observed with *EINSTEIN* by Stewart *et al.* (1982) who found it to have a (0.5-3 keV) X–ray luminosity of $\sim 10^{40}\,\mathrm{erg\,s^{-1}}$. NGC 5408 was observed by the LAC on *Ginga* from 06:10 UT on July 11th 1989 to 04:20 UT on July 12th 1989. A 'universal' background subtraction was performed and an upper limit to the 2-10 keV count rate is $1.37 \pm 0.07\,\mathrm{ct\,s^{-1}}$. In order to check

for the possible contaminating effects of bright sources, a scanning observation was performed just after the source observation. There was a confusing QSO, PKS 1355-416, in the field of view of the LAC at a collimator transmission efficiency of about 25 per cent. The *EINSTEIN* IPC count rate for this source was $0.169 \pm 0.017 \, \text{ct s}^{-1}$, four times greater than that of NGC 5408, so we expect the greatest possible contamination from this source to be 50 per cent in the IPC band. However during the scan the transmission efficiency for this source rose to 50 per cent and this rise was not mirrored in the 2-10 keV scan light curve, so on this basis PKS 1355-416 is not expected to dominate the emission in this band. The statistical error on the count rate is much less than the fluctuation noise and to test the effect of this latter uncertainty 10% of the spectrum of the diffuse XRB was added to the pulse hight data which were refitted. Simple thermal bremsstrahlung and power law models were tested. The line of sight absorbing column was initially included as a free parameter but in all cases gave results consistent with the galactic value of $0.6 \times 10^{21} \text{cm}^{-3}$ and so was fixed at this value. The best fitting model parameters for thermal and non-thermal fits are presented in Tables 2.2 and 2.3 and the corresponding incident spectra are shown in Figure 2.2..

All errors are 90% confidence with one parameter taken to be of no interest. Both thermal and power law models provide statistically acceptable fits to the data. The thermal model is preferred for the original data, and the temperature of $2.97^{+1.14}_{-1.15}$ keV is consistent with the limit inferred from the IPC data (Stewart *et al* 1982), although lower than the temperatures found for the starbursts NGC 253 and M82 in Ohashi *et al.* (1990). The best fit power law model has a very steep ($\Gamma = 2.88^{+1.12}_{-0.50}$) spectrum, strengthening the belief that PKS 1355-416 does not dominate the 2-10 keV spectrum.

Adding ten per cent of the diffuse background increases the best fit temperature of a thermal model to $KT = 5.44^{+1.53}_{-1.24}$ keV and reduces the upper limits to the line equivalent width and the absorbing column density. The slope of a power law model is flattened to $2.17^{+0.44}_{-0.17}$

	kT (keV)	Equivalent width of $K\alpha$ (eV)	N_H (10^{21}cm^{-2})	χ^2_r (d.o.f)
Original data	$2.97^{+1.14}_{-1.15}$	120^{+1800}_{-120}	< 12	0.54 (8)
Including 10% diffuse background spectrum	$5.44^{+1.53}_{-1.24}$	68^{+610}_{-68}	< 3.2	0.99 (8)

Table 2.2: Results of thermal bremsstrahlung fits

	Γ	Equivalent width of $K\alpha$ (eV)	N_H (10^{21}cm^{-2})	χ^2_r (d.o.f)
Original data	$2.88^{+1.14}_{-0.50}$	< 1490	$7.0^{+25}_{-7.0}$	0.67 (8)
Including 10% diffuse background spectrum	$2.17^{+0.44}_{-0.17}$	< 570	$1.5^{+12}_{-1.5}$	0.49 (8)

Table 2.3: Results of power law fits
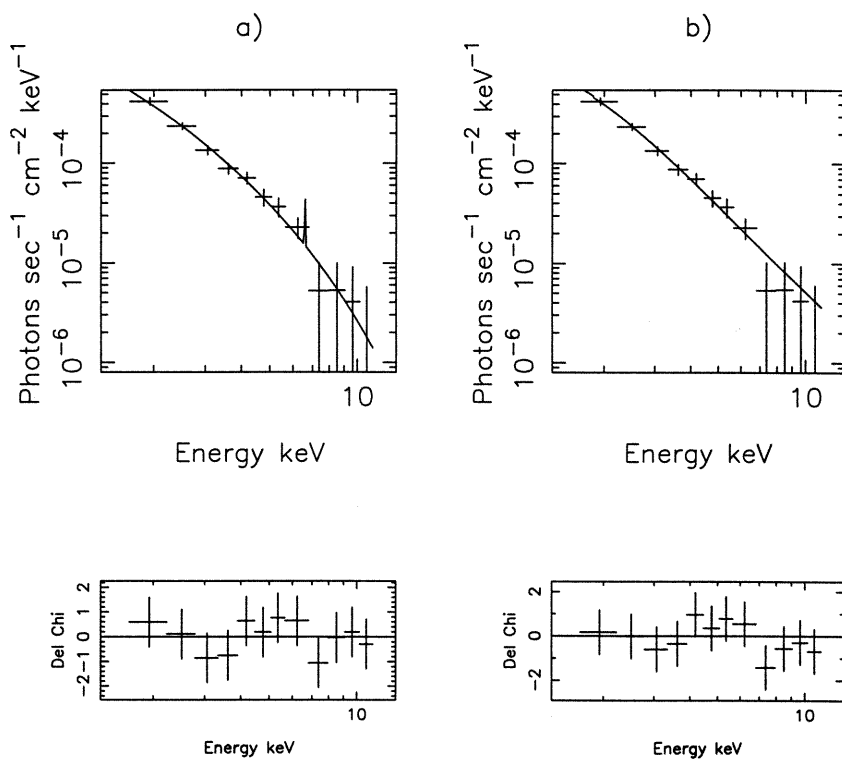
Figure 2.2: Best fitting model spectra: a) thermal model. b) power law model.

Even with the large statistical uncertainties involved the best fitting spectra do not resemble those of MXRB and are too steep for local starburst galaxies to contribute significantly to the hard X–ray background if the few so far observed are representative, although they could make a contribution in the soft band. Daly (1991) comes to a similar conclusion by considering arguments based on energetics.

In order for star-forming galaxies to contribute significantly to the XRB above 2 keV there must be evolution. However Gruber *et al.* (1992) report a very hard mean X–ray spectrum from the 53 brightest 60 micron IRAS sources (which the authors assume to be starburst galaxies although there are few optical IDs available).

2.5   Summary

None of the classes of sources described above are ideal candidates for producing the XRB. The source counts of clusters of galaxies fall off too rapidly and their spectra are ill-matched to the XRB spectrum. Starburst galaxies may be contributing, but only if the source spectra of the three local starbursts are atypical of the population or if there is significant evolution. In any case, one would expect starburst galaxies to be clustered like normal galaxies.

AGN seem the most likely candidates of the known sources. The discovery of the flattening of the spectra above 10 keV has removed some of the spectral objections, however the restrictions on the clustering properties of sources producing the XRB apply equally to both AGN and starburst galaxies.

Chapter 3

Analysis of the Ginga

Background Fluctuations

Overview

This chapter describes the datasets and the analysis methods used in an independent study of the background fluctuations. The results of fitting model P(D) curves to the observed fluctuation distribution are described and limits on the excess variance due to source clustering are discussed. Finally the spectrum of the fluctuations is derived.

A preliminary study of XRB fluctuations using *Ginga* data has been presented by Hayashida (1990). The work described here is the result of an independent and parallel study, preliminary results from which have been reported in Warwick & Stewart (1989) and Warwick & Butcher (1992).

3.1 Data

The data used in the fluctuations analysis comes from two types of observation: dedicated raster scans of the background and blank sky observations taken as

part of the normal background monitoring programme. The data reduction was different for the two sources of data and they are discussed in more detail below. The data were all taken in MPC1 mode and only data from the top layer of the LAC are used.

3.1.1 Dedicated Observations

Three sets of dedicated raster scans of blank sky were made in January 1988, July 1988 and March 1989. Independent sky regions were observed at the rate of one per satellite orbit; the typical exposure time per pointing was $\sim$ 2000 seconds. The three areas of sky observed in this way were the north and south galactic poles and the north ecliptic pole. Figure 3.1 shows the pointing directions for these raster scans. Each set of data was fitted to a model of the form given in equation 1.1. A simulated background model was generated and subtracted and then the spectrum for each pointing position was extracted. Data from the contact (high background) orbits were excluded and a total of 62 raster pointings were obtained.

3.1.2 The *Ginga* background database

As discussed in Section 1.3, *Ginga* had no facility for simultaneous background measurement during a source observation; a typical *Ginga* observation consisted of one day pointing at the source and another day pointing at a nearby region of 'blank' sky. Over the lifetime of the mission there thus accumulated a large database of potentially useful background observations.

This chapter describes the analysis of 70 such observations of independent sky regions made between June 1987 and August 1989. The observations are all at high galactic latitude ($|b| > 25°$) and are chosen so that there is no solar contamination. The typical exposure of an observation is $\sim$ 15000 seconds. Where there existed multiple pointings in the same direction the one with the largest exposure
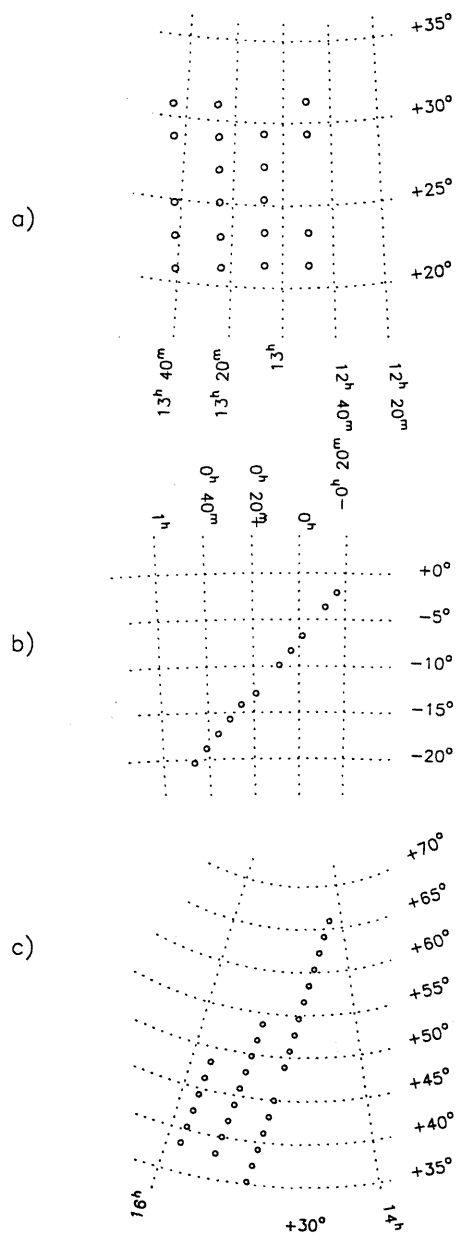
Figure 3.1: Pointing directions for the three sets of raster scans.

was used. Figure 3.2 shows the distribution of these observations over the sky. It should be noted that the distribution of these pointings is neither uniform nor random but follows, to first order, the distribution of X–ray sources above the *Ginga* limiting sensitivity.

Estimating the internal background for the database observations was not a trivial process. As the observations were spread over a long time period it was necessary to model the variations in internal background caused by the 37 day precession of the satellite orbit (Hayashida *et al.* 1989). Such modelling requires many observations spread over all phases of the orbit. There is also a long term drift of the internal background due to the decay of the satellite orbit which could not be adequately included in the fitting procedure. To minimise the effect of this long term drift whilst trying to optimise the modelling of the 37 day component the 70 observations were divided into 2 groups containing 36 and 34 pointings, each group spanning 13 months. The two groups were fit to models of the form, *eg.*

$$I(E,t) = a_1(E) + a_2(E) + \cdots + a_{35}(E) + \sum_{i=36}^{41} a_i(E) \times x_i(t) \qquad (3.1)$$

The time dependent components are related to the same LAC parameters as for the dedicated observations, although the intensity of components due to the induced radioactivity have been calculated allowing for the 37 day variation. The time independent components represent the mean particle background plus the diffuse background intensity at each of the different pointing positions; these were averaged to give the mean diffuse background intensity. This mean was then subtracted from each constant component in turn to produce the fluctuations.

The resulting 70 fluctuations were then examined for residual systematic effects such as the long term drift in internal background mentioned above. Figure 3.3 shows the residual fluctuation level in the 2-10 keV band against time for all 70 fluctuations. The top panel shows data from the mid layer and the lower panel shows data from the top layer of the LAC. A clear discontinuity can be seen in the mid layer data: this is due to the separate modelling of the two sets of data, which renormalises the zero point. The detection efficiency for X–rays from the

36
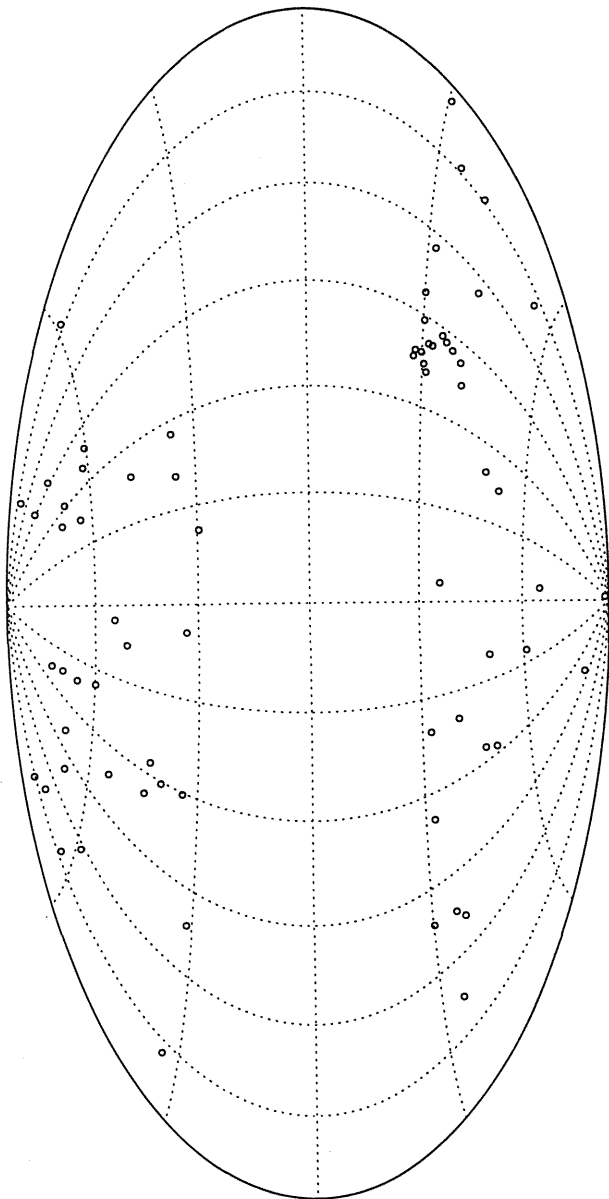
Figure 3.2: Distribution of database pointings in galactic coordinates. The concentration in the bottom right hand corner corresponds to background observations made during the regular monitoring of SN 1987A.

diffuse XRB is low in the mid-layer: this long term drift is therefore a measure of the changes in the particle background. The residual fluctuation level in the mid layer is significantly correlated with time for both of the sets of data (using Spearman rank correlation). The effect is more significant for the second set of data (August 1988–September 1989) showing that the particle background was changing (reducing with the natural decay of the orbit) more rapidly during this time. There is no statistically significant trend in the top layer data used in the fluctuation analysis.

The fluctuations were also examined for the effects of galactic latitude. Figure 3.4 shows the mean count rates for the data divided into 10° bins in galactic latitude; no trends can be seen.

The 'Universal' background models

A common problem in analysing source observations, especially in the latter part of the mission, was the lack of a sufficiently long, contemporaneous background observation. The database observations described above were used to create the so-called 'Universal' subtraction coefficients. The data were fitted in 4 month sections, at 2 month intervals (so that nearly every observation fell into the middle two months of an 'Universal' background subtraction period) and the model coefficients were determined using equation 3.1. The constant components were averaged to give the mean (particle + diffuse) contribution.

Diffuse XRB spectrum

By utilising data from periods when *Ginga* was pointing at the dark earth (when the LAC should be registering counts purely from the internal background) it was possible to estimate the count rate and spectrum of the diffuse XRB. Unfortunately, the amount of dark earth data was small and this limited the accuracy of the results. The count rate due to the XRB was 15 cts/sec in the energy range

38

Mid

Time (MJD)

Top

Time (MJD)
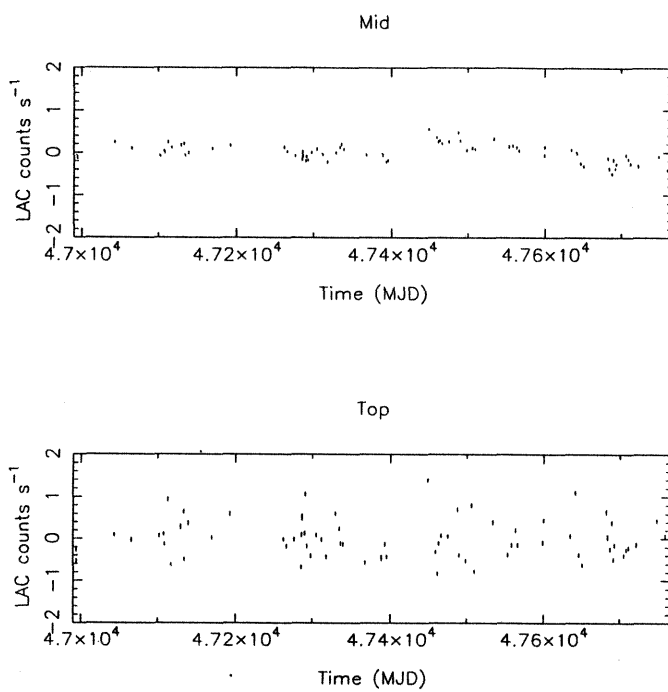
Figure 3.3: Fluctuation level against modified Julian data for the database observations. The discontinuity in the mid layer date (top panel) just after day 47400 is due to the division of the data into two sets for modelling the particle background.
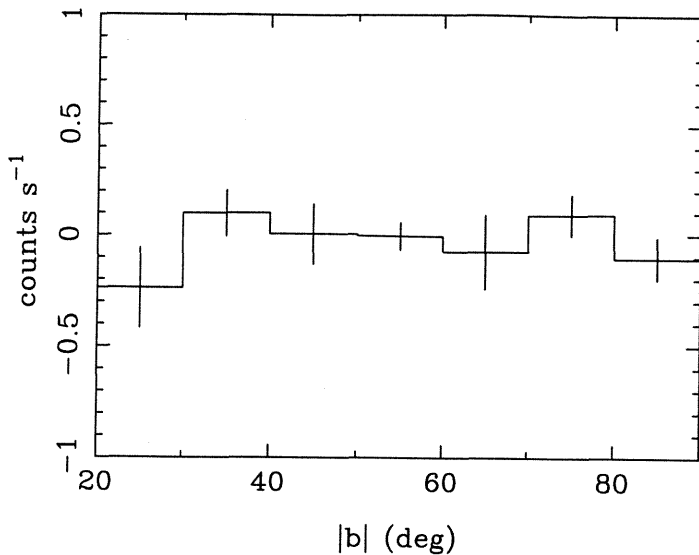
Figure 3.4: Mean 4–11 keV count rates for the fluctuation data binned by galactic latitude. No trends are visible in the data.

2–11 keV. The pulse height data were fit with a model power law spectrum using standard χ^2 minimisation techniques. Figure 3.5 shows the incident 2-10 keV spectrum for the best fitting power law model. The derived spectral parameters were $\alpha = 0.61^{+0.06}_{-0.03}$ and $N_H < 2.8 \times 10^{21}\,\mathrm{cm}^{-2}$. This is slightly steeper than the energy index $\alpha = 0.4$ reported by Marshall *et al.* 1980. As discussed in the previous chapter, the isolation of the diffuse XRB spectrum and normalisation was much more straightforward with HEAO-1. Collimator reflection may distort the spectrum measured by *Ginga*; Hayashida (1989) shows that this effect will increase the measured value of α by ~ 0.05 for α in the region considered here. Part of the discrepancy in spectral indices would also be explained if the dark earth were actually a faint source of hard X–rays (Peterson 1975).

3.2 Fluctuation Distribution

The fluctuation counts were summed into two energy ranges: LAC pulse height channels 4-7 (2-4 keV) and pulse height channels 8-20 (4-11 keV). The motivation
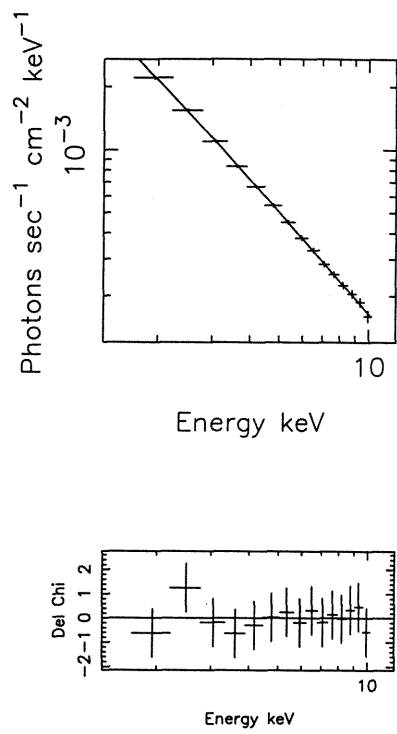
Figure 3.5: The best fitting power law model and residuals to the spectrum of the diffuse XRB.

for the separation into two energy bands was twofold:

- there was worry over the possible effects of collimator reflection on the observed P(D) curves - this effect would be restricted to the soft band.

- Preliminary results (Warwick & Stewart 1990) had shown a mismatch between the normalisations of the log N – log S derived from the EMSS and that derived from the *Ginga* fluctuations. If collimator reflection were to prove unimportant then comparing results in the two energy bands could yield important information to help reconcile the two.

Figure 3.6 shows the P(D) distributions for the 5 datasets in the two energy bands and Figure 3.7 shows the final P(D) distributions summed from all 5 datasets. The 90% confidence limits for $\Delta I/I$ in the two energy bands are 5% in both bands.

3.2.1   K-γ Fitting

The P(D) distributions were fit to models of the *differential* source counts given by:

$$N(S)dS = KS^{-\gamma}dS \qquad (3.2)$$

ie. $\gamma = 2.5$ corresponds to the Euclidean form of the source counts. Trial log N–log S relationships were convolved with the beam shape, using the Fourier techniques detailed in the appendix, to produce model P(D) curves. Equation A.27 in the appendix gives the general solutions to the $P(D)$ distribution and briefly describes how the method was used in the form of a computer program handling discrete calculations (see also Shafer (1983)). These model $P(D)$ distributions cannot be directly compared to the observed fluctuation distributions as they do not include the effects of counting statistics (see Shafer (1983) for a more detailed discussion). The model P(D) curves were convolved with a gaussian of standard deviation $\sigma = 0.1$ cts/sec in the hard band and $\sigma = 0.12$ cts/sec in
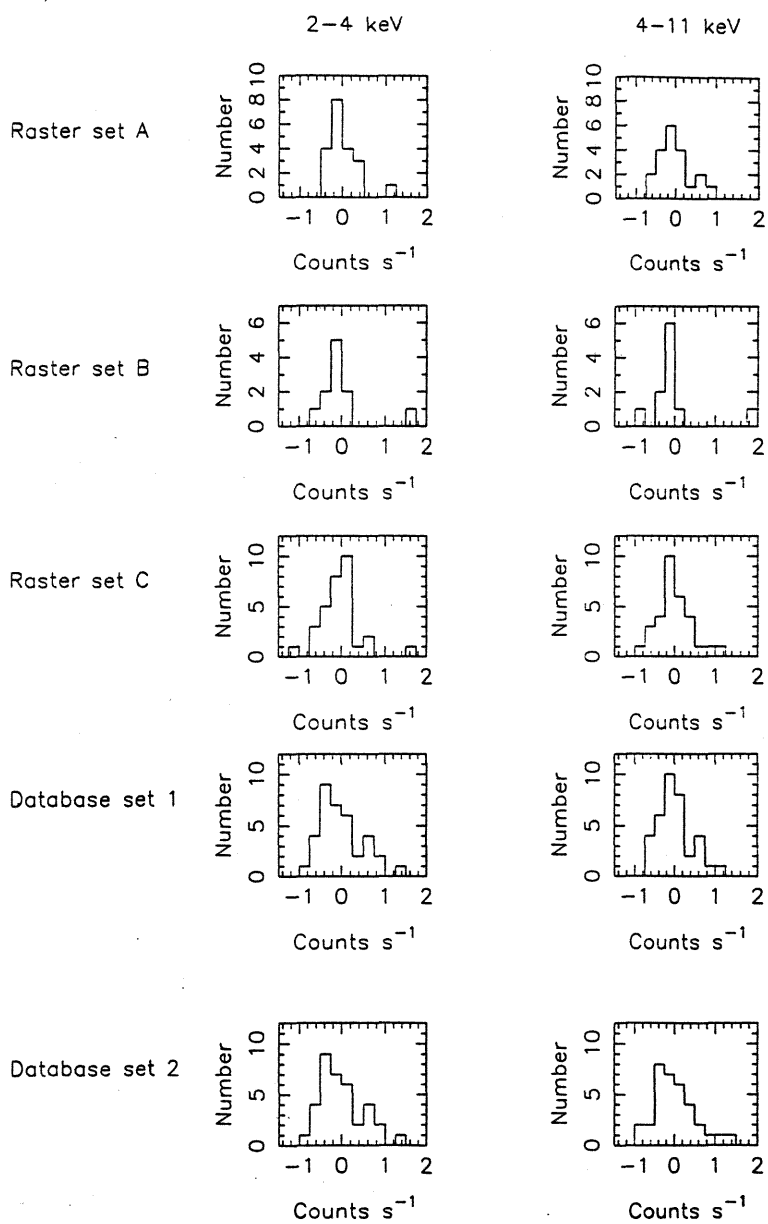
Figure 3.6: Two colour P(D) distributions for the 5 datasets.
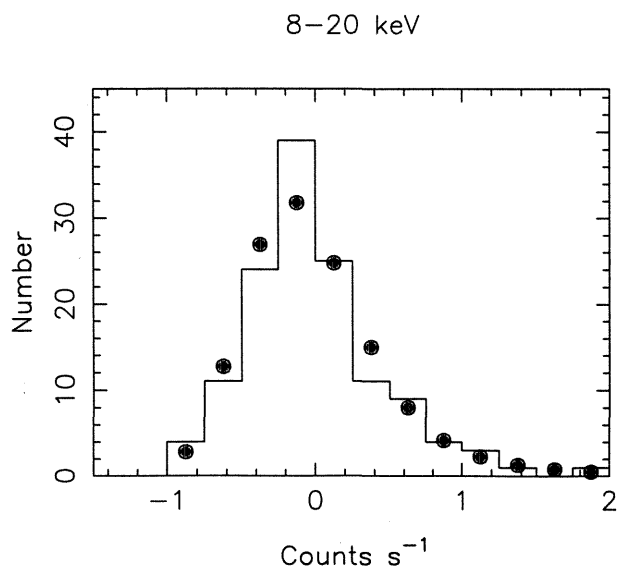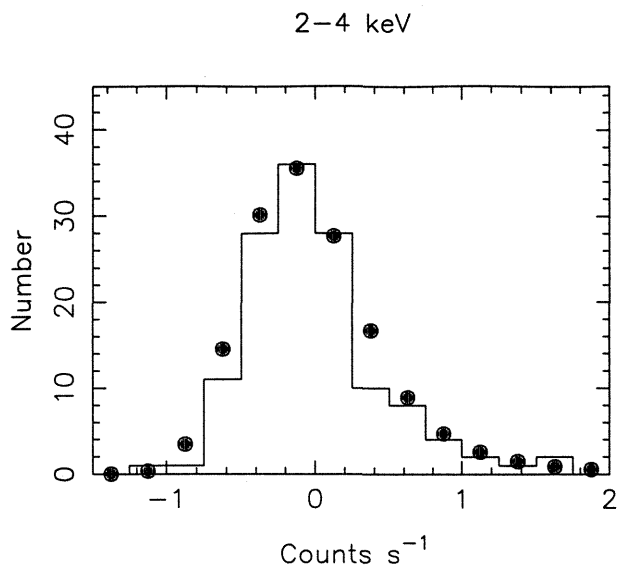
Figure 3.7: Final two colour P(D) distributions. The dots represent the best fitting K, Γ distribution described in the text.

	2–4 keV		4-11 keV	
	γ	K	γ	K
Best fitting model	$2.53^{+0.15}_{-0.13}$	210^{+53}_{-36}	$2.58^{+0.18}_{-0.14}$	210^{+60}_{-38}
Best Euclidean model	2.5	218^{+54}_{-36}	2.5	234^{+56}_{-41}

Table 3.1: normalisation and slope for the best fitting source counts model and for the best fitting Euclidean model. K is in units of $(\mathrm{LAC\,ct\,s^{-1}})^{\gamma-1}\,\mathrm{sr}^{-1}$.

the softer band, to include the effect of counting statistics and systematic errors. These are the appropriate statistical errors for the short, $1-2\times10^3$ second scan observations while for the longer pointings the value is dominated by the systematic errors in the background modelling procedure. For the database pointings the value of σ was estimated by comparing observations of the same region of sky. The results are not sensitive to the exact value of σ within appropriate limits. The models were then compared to the observed distribution using the χ^2 statistic. The log N–log S curves were truncated at low fluxes to avoid overproducing the XRB.

Figure 3.8 shows the confidence contours for the slope and normalisation of the differential source counts in the two colours.

The best fit parameters are in Table 3.1. They are consistent with the Euclidean form in both colours although, as discussed in the appendix, this fact alone must imply a modest degree of evolution of the source counts since cosmological effects should cause non-evolving source counts to deviate from the Euclidean form. Butcher et al. (1994) point out that these results are entirely consistent with those obtained by using maximum likelihood methods.

3.2.2 Excess Variance

If the sources giving rise to the fluctuations are clustered then the variation in the number of sources per beam is enlarged and the expected fluctuation
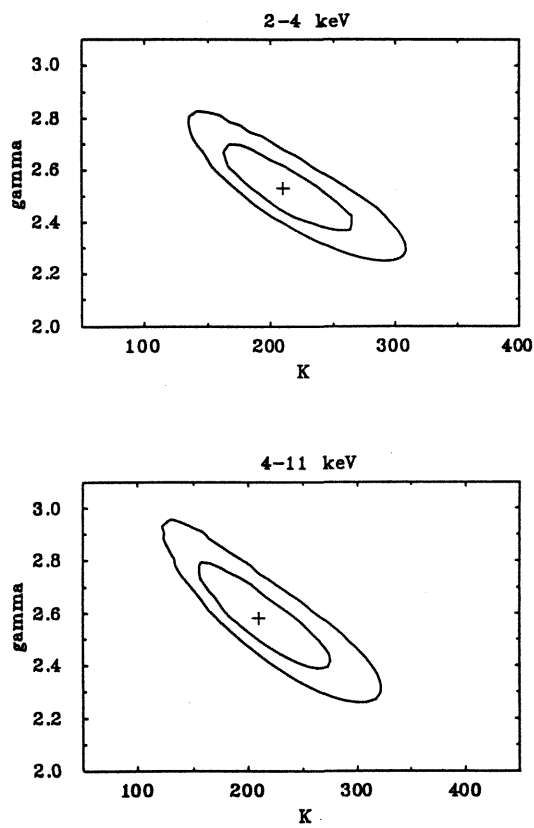
Figure 3.8: 68% and 90% confidence contours for the best fitting slope,' Γ and normalisation, K, of the differential source counts. K is plotted in *Ginga* units of $(LAC\,ct\,s^{-1})^{\gamma-1}\,sr^{-1}$. The confidence regions are calculated for one interesting parameter.

distribution is wider. It is usual to mimic the effect of this source clustering by convolving the fluctuation distribution for unclustered sources with a gaussian of standard deviation σ_{ex} (recall that $\sigma_{ex} \sim 0.1\,\mathrm{ct\,s^{-1}}$ is necessary to account for the effect of counting statistics). This excess variance was treated as a free parameter in the model fitting procedure which was repeated for the best fitting model $\gamma = 2.59$ and for the Euclidean case. Figure 3.9 shows a plot of minimum χ^2 against excess variance for the two cases mentioned. Considering σ_{ex} to be the only interesting parameter then the one sigma limit, $\chi^2 + 1$, corresponds to $\sigma_{ex} < 0.26\,\mathrm{ct\,s^{-1}}$ and at two sigma confidence $\sigma_{ex} < 0.35\,\mathrm{ct\,s^{-1}}$. In both cases the best fit corresponds to some clustering, but in neither case can models with no source clustering be excluded. In fact Shafer (1983) shows that the chi-squared statistic produces systematically high limits of σ_{ex}, due to the need to bin the data, and that maximum likelihood methods are actually more appropriate. Using such techniques on this data, Barcons finds that at one sigma confidence $\sigma_{ex} < 0.17\,\mathrm{ct\,s^{-1}}$ and at two sigma $\sigma_{ex} < 0.3\,\mathrm{ct\,s^{-1}}$ (Butcher *et al.* 1994) These limits correspond to fluctuation levels of $\frac{\Delta I}{I} < 2\%$ and $\frac{\Delta I}{I} < 3.8\%$ respectively. The best fit value of K is, of course inversely correlated with σ_{ex} and this two sigma limit for σ_{ex} corresponds to a very low surface density source population, with most of the width of the P(D) curve coming from the excess variance.

3.2.3 Fluctuation Spectrum

The fluctuations spectrum has been presented in Warwick & Butcher (1992). In this section the derivation of the spectrum is discussed in more detail and more complex models are fitted. Figure 3.10 shows count rate in the 2-4 keV band plotted against 4–11 keV count rate for the fluctuations taken from the database pointings (the raster scan pointings were not used for this work because of their lower signal to noise ratio). The dashed lines show the division of the sample into positive (top right) and negative (bottom left) fluctuations used in Warwick & Butcher (1992). The average spectrum of negative fluctuations was subtracted from that of positive fluctuations to give a mean fluctuation spectrum, which

47

a)

b)
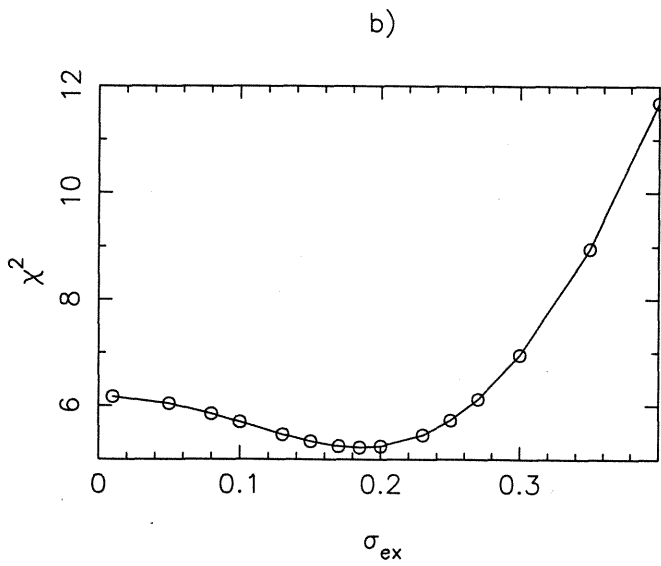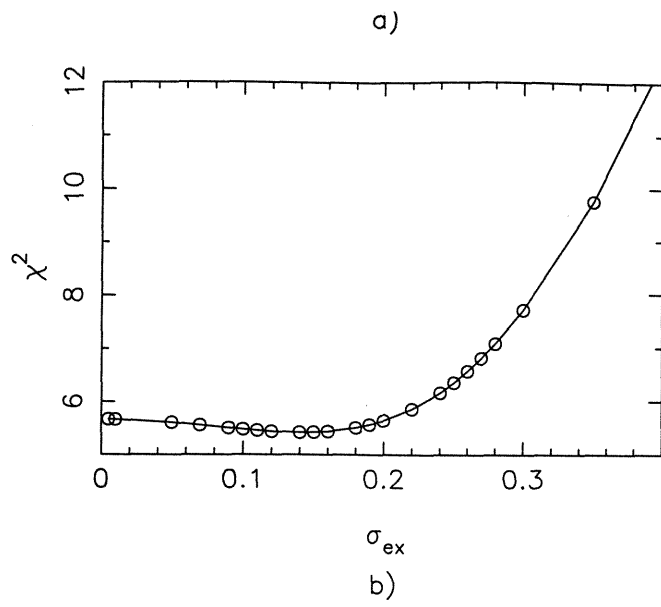
Figure 3.9: Excess variance, minimum χ^2 against σ_{ex} for $\gamma = 2.59$ (a) and $\gamma = 2.5$ (b). The energy band is 4-11 keV

was then analysed using standard spectral fitting routines. Figure 3.11 shows the incident spectrum and residuals for the best fitting power law model. The derived spectral parameters were $\alpha = 0.81^{+0.06}_{-0.05}$ and $N_H < 2 \times 10^{21} \, \text{cm}^{-2}$ (all errors quoted in this section are 68% confidence for 1 parameter of no interest). Note that the uncertainties in the spectral fitting of the diffuse background spectrum mentioned in Section 3.1.2 are not a problem here because the *differential* fluctuation spectrum is used. Although the model is formally acceptable at the 90% confidence limit ($\chi^2_\nu = 1.25$ for 24 degrees of freedom), an examination of the residuals to the fit shows an apparent hardening of the spectrum above 10 keV. Similar features are seen in the X–ray spectra of Seyfert galaxies (Nandra 1992) and are generally interpreted as evidence of Compton reflection from cold material near the central engine.

In order to check the fluctuation spectrum for biases due to the imposition of an apparently arbitrary division between negative and positive fluctuations, a spectrum was extracted on the basis of Figure 3.12, *ie.* a simple division between fluctuations less than the mean (zero counts) and those greater than the mean. A simple power law gave a very good fit to the data, $\chi^2_\nu = 1.04$; the incident spectrum and residuals are shown in Figure 3.13. The best fitting model parameters were $\alpha = 0.91^{+0.08}_{-0.05}$ and $N_H < 3 \times 10^{21} \, \text{cm}^{-2}$. The problem with this method of extracting the fluctation spectrum is that the fluctuations clustered close to zero contribute little to the signal, but much to the noise. The most appropriate method of deriving the spectrum would seem to be to exclude these points and to use points from the extremes of the distribution. Figure 3.14 shows the final division of the fluctuations into positive and negative and Figure 3.15 shows the model spectrum and residuals. In this case a simple power law model was not an acceptable fit to the data ($\chi^2_\nu = 1.90$ for 24 degrees of freedom). The derived spectral parameters were $\alpha = 0.81^{+0.03}_{-0.04}$ and $N_H < 0.5 \times 10^{21} \, \text{cm}^{-2}$.

With this motivation an extra, reflection component was added to the model, representing reflection from a slab of material, inclined at angle i to the line of sight, behind an isotropically emitting source (from the Monte Carlo calculations

49
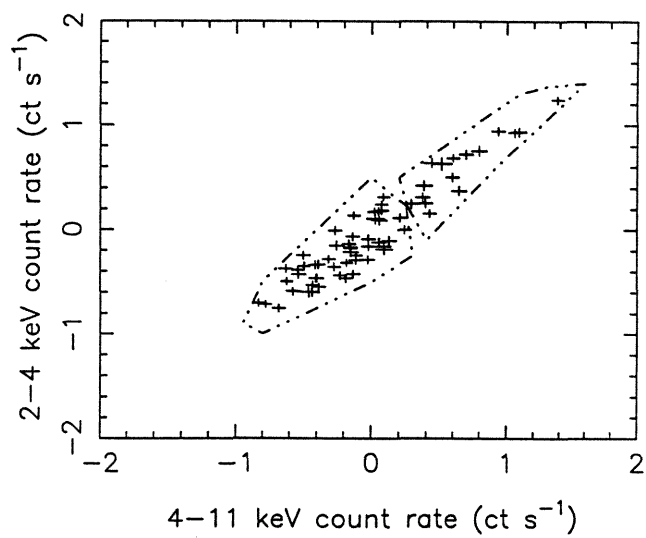
Figure 3.10: Soft (2–4 keV) LAC counts plotted against hard (4–11 keV) counts for the database pointings. The mean spectrum of points in the bottom left area was calculated and subtracted from the mean spectrum of points in the top right region to give the fluctuation spectrum shown in Figure 3.11. This is the method used in Warwick & Butcher (1992).
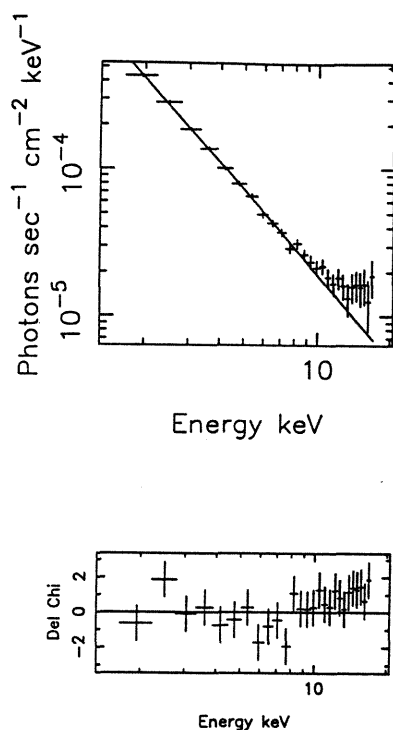
Figure 3.11: Incident spectrum and residuals for the best fitting power law model.

of George & Fabian (1991)). This model was fitted to the spectrum derived by the method shown in Figure 3.14. The inclination was fixed at 60°, the expected mean value. The inclusion of the reflection component as an additional free parameter gave a significantly (at greater than 99% confidence) improved fit and the fit was statistically acceptable at 90% confidence ($\chi^2_\nu = 1.33$ for 23 degrees of freedom). The unfolded spectrum and residuals are shown in Figure 3.16.

Analysis of the autocorrelation function

The set of 132 fluctuation pointings were used to study the autocorrelation function on scales > 2 degrees (Carrera *et al.* 1991). No significant signal was found on any scale and the upper limit at 2° was $\sim 10^{-4}$ (95% confidence). The results
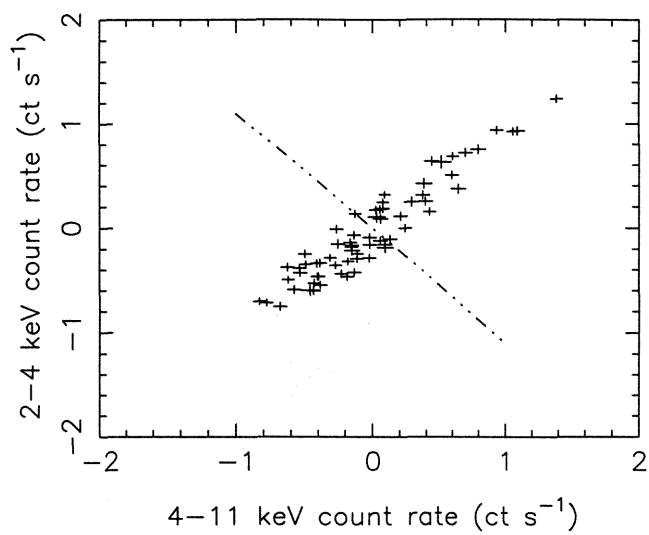
Figure 3.12: Soft (2–4 keV) LAC counts plotted against hard (4–11 keV) counts for the database pointings. The mean spectrum of points below the dashed line (*ie.* below the mean) was calculated and subtracted from the mean spectrum of points above the line to give the fluctuation spectrum shown in Figure 3.13.
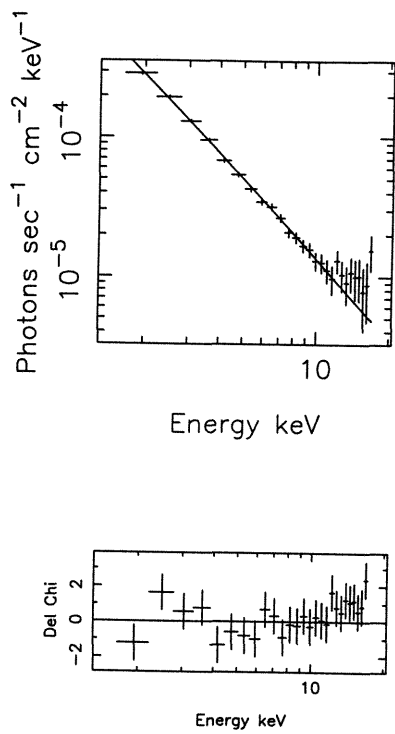
Figure 3.13: Incident spectrum and residuals for the best fitting power law model from the spectrum extracted using the method illustrated in Figure 3.12.
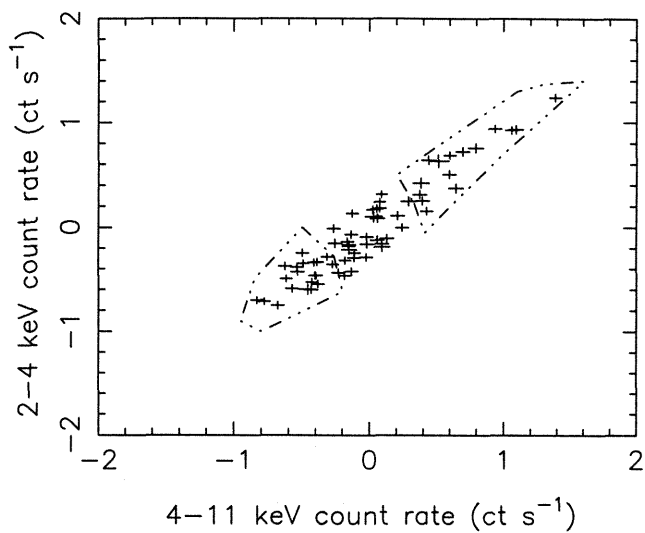
Figure 3.14: Soft (2–4 keV) LAC counts plotted against hard (4–11 keV) counts for the database pointings. The mean spectrum of points in the bottom left region was calculated and subtracted from the mean spectrum of points in the top right region to give the fluctuation spectrum shown in Figure 3.15.
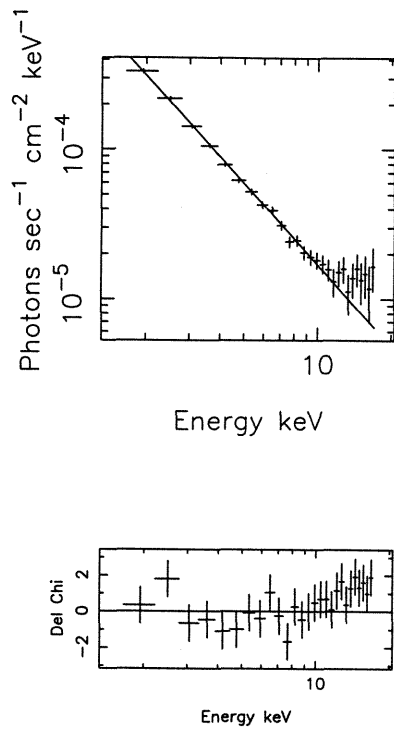
Figure 3.15: Incident spectrum and residuals for the best fitting power law model from the spectrum extracted using the method illustrated in Figure 3.14.
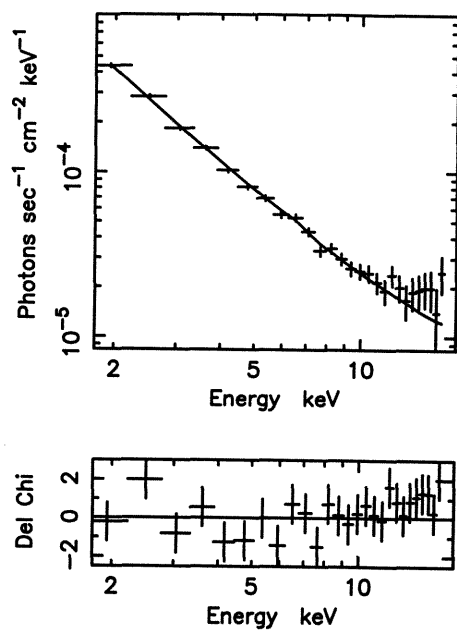
Figure 3.16: Incident spectrum and residuals for the mean fluctuation spectrum fitted to a model including a reflection component.
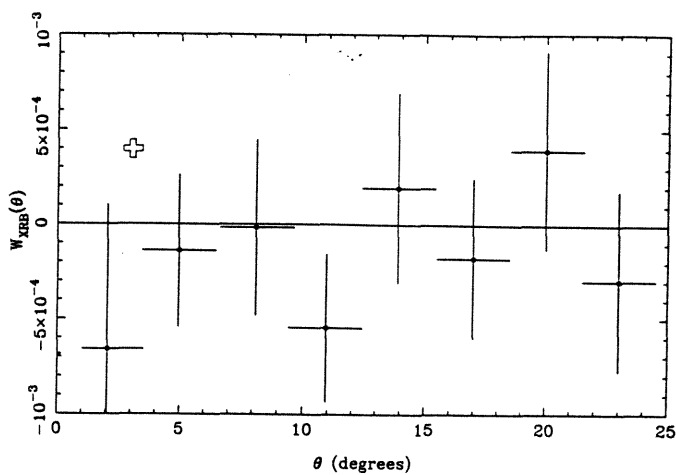
Figure 3.17: The autocorrelation function of the 4–12 keV X–ray background, taken from Carrera *et al.* 1991. The vertical bars represent the 95% confidence region. The cross is the 95% upper limit of Persic *et al.* 1989.

are shown in Figure 3.17. It was found that QSOs with correlation lengths of $\sim 8h^{-1}$ Mpc can contribute no more than 50% of the 4–12 keV XRB.

In 1990 *Ginga* performed a set of scanning observations of the North Galactic Pole (NGP) and North Ecliptic Pole (NEP) regions. The data were binned into 0.2 degree bins along the scan path and the autocorelation function was calculated. After subtracting the ACF expected due to the LAC collimator response, the cosmic ACF on scales 0.2 to 12 degrees was deduced. The two sigma upper limit to the signal on scales smaller than the collimator size ranges from $W(0.2\,\mathrm{deg}) < 1.5 \times 10^{-3}$ to $W(2\,\mathrm{deg}) < 5 \times 10^{-4}$. Above 2 degrees the pointed data provide a better upper limit. A full description of the analysis and results can be found in Carrera *et al.* (1992).

Results of cross-correlating with the Abell catalogue

The list of fluctuation positions was correlated with the Abell catalogues (Abell 1958, Abell Corwin & Olowin 1989) to look for serendipitous clusters of galaxies in the field of view. A total of 41 clusters were found in 23 of the fields. These clusters are typically in Abell distance classes 5-6. Figure 3.18 shows the P(D) distributions for fields containing clusters on the same axes as the distribution for fields without clusters. The mean and median levels for the fields containing clusters are higher in both the 2-4 and 4-11 keV bands, but a K-S test shows no statistically significant difference between the two sub-samples. The spectra for fields with and without Abell clusters were extracted. It is not correct to derive the AGN contribution to the cluster spectrum by considering only fields without Abell clusters (as done by Hayashida *et al.* 1992) since, even in fields containing an Abell cluster, the fluctuations may be dominated by the presence or absence of a bright AGN, while the Abell catalogue is known to be incomplete at the distances considered here. However, the difference between the spectra may, in principle, yield some information on the mean spectra of clusters at redshifts ~ 0.2. The separate spectra were fitted to simple power law models; the results were entirely consistent with those obtained earlier, although the confidence limits on parameters were generally worse, due to the poorer statistics of the sub-samples. Thus this study provides no evidence that the properties of fluctuation fields with an Abell cluster in the field of view are in anyway different from those which contain no cluster.
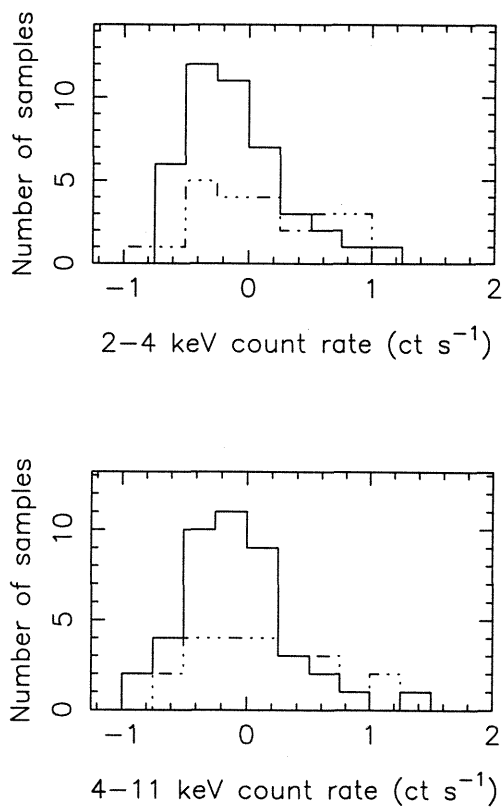
Figure 3.18: 4–11 keV P(D) distributions for database fluctuation pointings with (dotted line) and without (dashed line) serendipitous Abell clusters in the field of view. Although the mean of the distribution of fields containing clusters is shifted to the right relative to the mean of the non-cluster sample, the two sub-samples cannot be distinguished using a KS test.

3.3 Summary

- The fluctuations data show no trends with galactic latitude.

- The slopes of the source counts inferred from both energy bands are consistent with each other and with an Euclidean slope, $\Gamma = 2.5$.

- Examining the excess variance reveals no evidence for source clustering,

- The spectrum of the fluctuations is best fit by a model including a reflection component.

- There are no significant differences between the sample of fluctuation fields which contain Abell clusters and those which do not.

Chapter 4

Implications for the Origin of the X–ray Background

Overview

The results presented in the previous chapter are interpreted. Predicted source counts from clusters of galaxies and AGN are calculated and compared with the source counts inferred from the fluctuations and with those inferred from the EMSS. Absorbed, low luminosity Seyferts are put forward as the most likely candidates for producing the 2-10 keV X-ray background.

4.1   From K, γ to $N(S)$

In order to compare the two colour confidence regions for K and γ described in the previous chapter the two sets of models must be converted to the same energy band (chosen to be 2–10 keV as the source counts will later be compared with those obtained by the *HEAO-1* A-2 experiment (Shafer 1983)).

Formally, the comparison of the resulting $K - \gamma$ confidence regions in the two bands requires detailed knowledge of the spectra of the sources causing the fluc-

tuations over the entire energy range 2–11 keV. In the absence of such detailed spectral information the counts are converted to the hard band by use of an average spectral conversion factor f defined by, eg.

$$f = \frac{S(2 - 10\,\text{keV})}{S(4 - 11\,\text{keV})} \qquad (4.1)$$

Figure 4.1 shows curves of constant f in the Γ, N_H plane for spectral parameters typical of extragalactic X–ray sources. If f is constant for the whole source population then the source count normalisations in the two bands are related by:

$$K(2 - 10\,\text{keV}) = f^{\gamma-1} \times K(4 - 11\,\text{keV}) \qquad (4.2)$$

The models derived in the 2-4 keV band may be similarly transformed. The spectral conversion factors used were those appropriate to a power-law spectrum with $\alpha = 0.8$ and a nominal galactic column of $3 \times 10^{20}\,\text{cm}^{-2}$ (consistent with the fluctuation spectrum presented in the previous chapter). These conversion factors are calculated from

1 LAC ct s^{-1} (4–11 keV) = 4.2×10^{-12} ergs cm^{-1} s^{-1} (2–10 keV)

1 LAC ct s^{-1} (2–4 keV) = 4.4×10^{-12} ergs cm^{-1} s^{-1} (2–10 keV)

Table 4.1 summarises the best fitting models in the 2–10 keV band inferrred from the 2–4 keV and 4-11 keV bands. The parameters for the best fitting Euclidean models are also shown. The inferred Euclidean 2–10 keV source count normalisations deduced from the two colours are in excellent agreement with each other and with the normalisation of the resolved source counts in Piccinotti *et al.* (1982). The normalisation deduced from the soft *Ginga* fluctuations is much more sensitive to the assumed spectral shape of the fluctuations and, for this reason, most of the rest of this chapter considers only results derived from the 4-11 keV band.
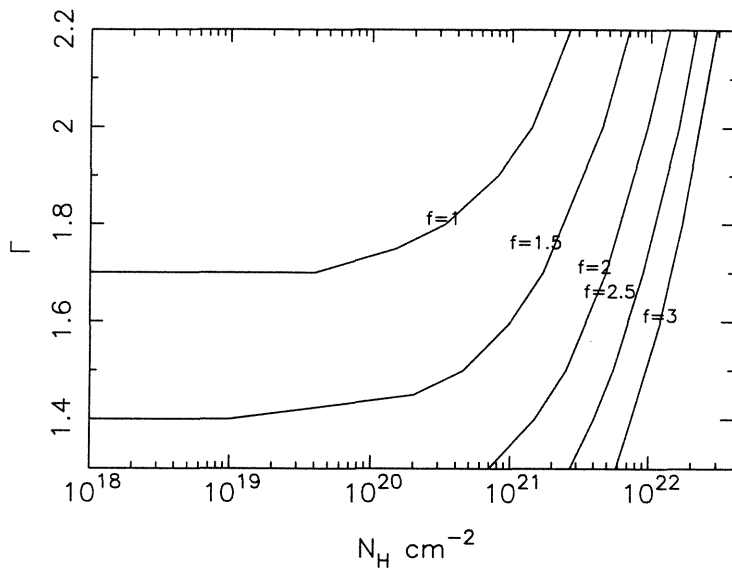
Figure 4.1: Spectral conversion factor f (see text) plotted for various values of power-law slope and absorbing column.

	2–4 keV		4-11 keV	
	γ	K	γ	K
Best fitting model	$\gamma = 2.53^{+0.15}_{-0.13}$	$K = 8.8^{+2}_{-1.5} \times 10^{-16}$	$\gamma = 2.58^{+0.18}_{-0.14}$	$K = 2.2^{+0.7}_{-0.4} \times 10^{-16}$
Best Euclidean model	$\gamma = 2.5$	$K = 2.0^{+0.5}_{-0.3} \times 10^{-15}$	$\gamma = 2.5$	$K = 2.0^{+0.5}_{-0.3} \times 10^{-15}$

Table 4.1: The normalisations and slopes of the 2–10 keV source counts deduced form the *Ginga* fluctuations in the colours 2–4 keV and 4–11 keV using the spectral conversions discussed in the text. Both of the best fitting models are slightly steeper than the Euclidean, however this latter is not excluded by the data and the normalisations for the best fitting Euclidean models are also shown. The normalisation, K, is in units of $(\mathrm{erg\,cm^{-2}\,s^{-1}})^{\gamma-1}\,\mathrm{sr^{-1}}$.

4.2 The 2–10 keV $N(S)$ relation

The confidence contours for K and γ presented in the previous chapter must be converted into detector independent models for $N(S)$. The source counts will be plotted in the form first devised by radio astronomers and immortalised in the X–ray band by Shafer (1983). The y axis represents $N(S)$ for each model divided by $N(S)$ from the best fitting Euclidean model to the resolved source counts and the fluctuations, $N_0(S)dS = 2 \times 10^{-15}\,\mathrm{erg\,cm^{-2}\,s^{-1}\,sr^{-1}}$. The differential source counts are plotted in Figure 4.2. The interpretation of this diagram may not be intuitively obvious and it is important to understand what information the figure does and does not contain. A line $y = 1$ would correspond to the best fitting Euclidean model; other Euclidean models appear as horizontal lines. In general, power-law models appear as straight lines and the solid line in Figure 4.2 defines the region within which power-law models acceptable at the 90% level must lie. The right hand edge of the fish corresponds to the value of S_{max}. The dash-dotted line to the left shows where the integrated emission from power-law models produces the entire X–ray background. The left-hand edge of the fish must be treated with caution. It is *not* a lower flux limit to the validity of power-law models, as might be assumed from a brief glance. This line was determined by treating K and γ for the steepest, Euclidean and shallowest slopes as fixed parameters and varying the value of S_{min} used in the fitting procedure until χ^2 was exceeded at 90% confidence. Thus the dotted line represents the minimum flux to which a single index power-law model must extend, *i.e.* an Euclidean model of the form illustrated by the dashed line labelled a) in Figure 4.2 is acceptable, while a model corresponding to the line labelled b) is not. Models which truncate between the dotted line and dash-dotted line are statistically indistinguishable from models which continue all the way to the dash-dotted line.
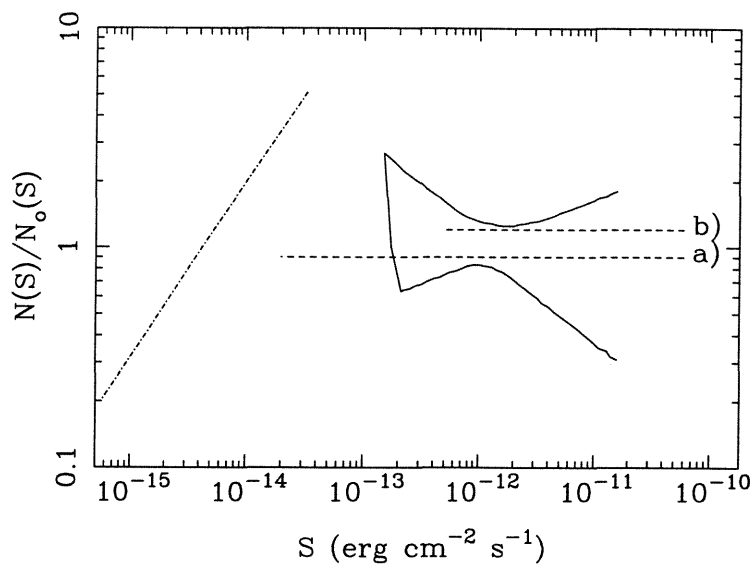
Figure 4.2: The 90% confidence region for the 2–10 keV source counts; $N(S)dS$ is plotted normalised to the Euclidean form. A more detailed explanation is given in the text.

4.3 Comparison with *HEAO-1* results

Figure 4.3 shows 2–10 keV source counts determined by *Ginga* (solid line) and *HEAO-1* fluctuations (Shafer 1983) (dashed line). The individual data points are calculated from Shafer's (1983) treatment of the *HEAO-1* resolved sources (Piccinotti *et al.* 1982). This includes more source identifications than the original paper. A counts to flux conversion of $1R15ct\,s^{-1} = 2.17 \times 10^{-11}\,erg\,s^{-1}$ has been assumed and Shafer's corrections for Malmquist bias are included. Following Shafer, the galactic sources of Piccinotti *et al.* are included, as these contribute to the fluctuations at a similar level.

The normalisations are in excellent agreement and the figure shows that the 2–10 keV source counts are consistent with the Euclidean form over nearly three decades in flux.

The *HEAO-1* fluctuation source counts are most tightly constrained at fluxes about six times fainter than the lower limit of the Piccinotti sample, while the *Ginga* source counts are best constrained at fluxes about thirty times lower than the Piccinotti limit, $S \sim 1 \times 10^{-12}\,erg\,cm^{-2}\,s^{-1}$. It is often stated (*e.g.* Scheuer 1974) that the fluctuations are dominated by sources at the flux levels where there is one source per beam. For *Ginga* this corresponds to a flux level of $S \sim 2.2 \times 10^{-12}\,erg\,cm^{-2}\,s^{-1}$ so, in common with Shafer (1983) and Hayashida (1989), it is found that the fluctuations constrain the source counts most strongly just below the one source per beam level.

4.4 Comparison with the EMSS

The *Ginga* fluctuation studies are the most sensitive results obtained to date in the 2–10 keV band. However, the EMSS (Gioia *et al.* 1990a) reached similar fluxes in the energy band 0.3–3.5 keV and it is natural to compare the $N(S)$ relations obtained in the two energy bands. The EMSS source counts were con-
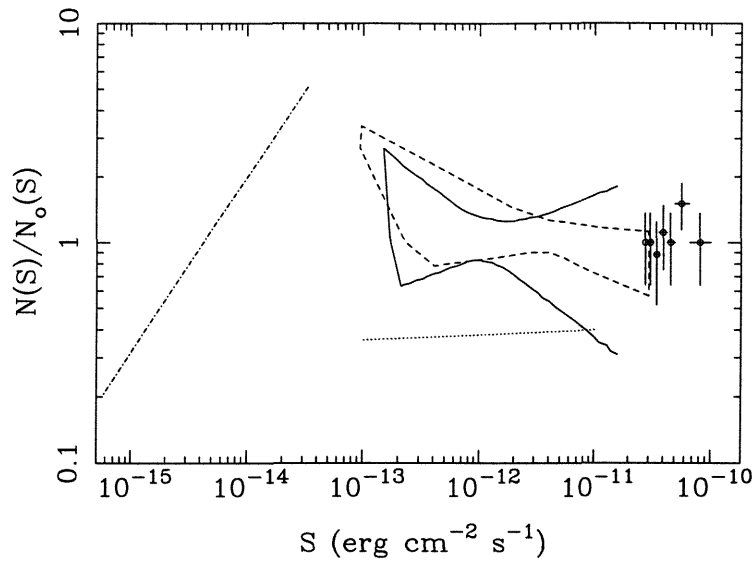
Figure 4.3: The 2–10 keV source counts normalised to $N_0(S)dS = 2 \times 10^{-15}$ erg cm^{-2} s^{-1}. The solid line is from the results presented in this thesis, the dashed line is from the *HEAO-1* fluctuation analysis of Shafer (1983) and the solid points are from the resolved source counts of Piccinotti *et al.* (1982). The dotted line shows the EMSS prediction assuming $f = 1$ (see text).

verted to the 2–10 keV band using the technique described in section 4.1. For a power-law spectrum of index $\alpha = 0.7$, and a typical galactic absorption value of $n_H = 3 \times 10^{20}\text{cm}^{-2}$ then $f \sim 1$. The EMSS source counts then correspond to the dotted line in Figure 4.3; it is very clear that this underestimates the 2–10 keV source counts by a factor $\sim 2 - 3$.

In view of this discrepancy it is perhaps surprising that the source counts inferred from the two *Ginga* colours are in such good agreement, as the lower *Ginga* band overlaps the *EINSTEIN* IPC band (0.3–3.5 keV). It is possible that any real defficiency in soft X–ray source counts in the *EINSTEIN* band is exactly compensated by the effects of collimator reflection in the *Ginga* LAC. It seems more likely that the sources detected by *EINSTEIN* are dominated by sources with characteristic temperature < 2 keV, towards the lower end of the IPC band, while the sources in the *Ginga* 2–4 keV band are somewhat harder.

The mismatch between the *Ginga* source counts and those inferred from the EMSS has been a point of some controversy and it is important to verify that the effect is real. It is stressed that the discrepancy is *not* the result of assuming that the source counts are Euclidean, as the confidence region in 4.2 was obtained from *all* models acceptable at 90%, confidence. In the previous chapter it was mentioned that the normalisation of the source counts, K, was inversely proportional to the excess variance σ_{ex}. If source clustering is important, so that σ_{ex} is greater than the value used in the fitting procedure, then the source count normalisation deduced from the *Ginga* fluctuations may be significantly too high. Figure 4.4 shows the normalisation K plotted against σ_{ex} for the best fitting Euclidean models. In order to make the 2–10 keV source counts agree with the EMSS counts for an assumed $f \sim 1$, it would be necessary to reduce the normalisation of the hard source counts by a factor ~ 2. Inspection of Figure 4.4 shows that this would require $\sigma_{ex} \sim 0.35$ ct s^{-1}, which is excluded at two sigma confidence. Although this restriction on its own may not seem particularly stringent, it becomes stronger when the implications for source clustering are further considered. In Carrera *et al.* (1992) two sets of *Ginga* scan data were used to determine the ACF at
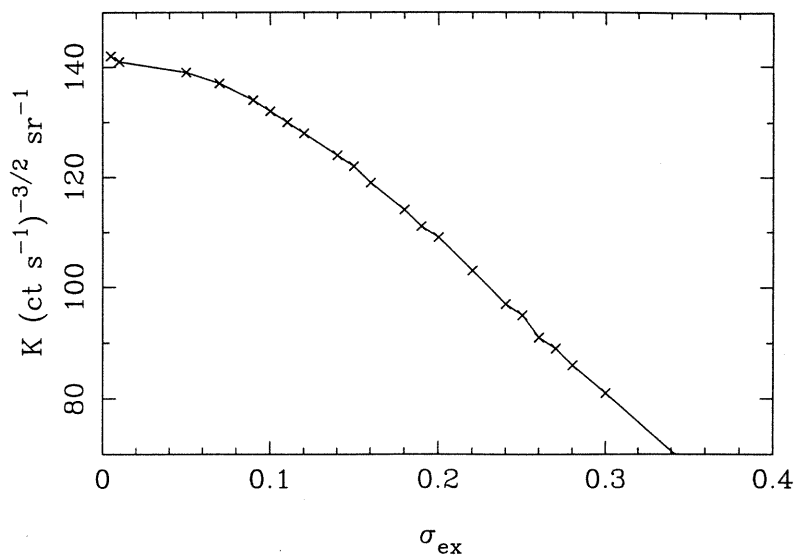
Figure 4.4: Differential source count normalisation, K, plotted against excess variance, σ_{ex}, for the best fitting Euclidean model.

scales down to 0.2°. No signal was found below 2°. The maximum amplitudes of the ACF at separations 0.1, 0.2 and 0.3 degrees are 0.05, 0.015 and 0.005 respectively (at 3 sigma confidence). The same paper also considered the clustering necessary to make the *Ginga* fluctuations consistent with the EMSS, given a canonical AGN spectrum. Figure 4.5 shows the results of fitting the source counts normalisation K and the clustering angle θ_0 for a clustering amplitude of unity (calculated for $\Gamma = 2.5$). The EMSS counts for a power-law spectrum with $\alpha = 0.7$ are also shown. It can be seen a clustering amplitude of unity on scales $\theta_0 \sim 0.3°$ is necessary to reconcile the soft and hard source counts. Even if some of the assumptions in the calculation are relaxed the necessary amplitude at 0.3° is not less than 0.1, still well above the measured limit.

Thus the *Ginga* fluctuations cannot be explained by source clustering and the mismatch with the EMSS source counts is real.

Having shown that the discrepancy between the source count normalisations cannot be explained by source clustering and the associated excess variance, it is
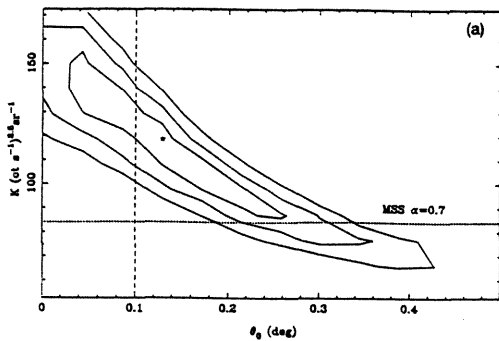
Figure 4.5: Best fit and 1σ, 2σ and 3σ contours showing the source counts normalisation and clustering angle for $\Gamma = 2.5$ and a clustering amplitude of 1.The dotted line shows the normalisation of the EMSS source counts for $\alpha = 0.7$. The dased line shows the maximum correlation length allowed by the ACF of the *Ginga* scan data. the figure is taken from Carrera *et al.* 1993.

necessary to consider the average spectral conversion factor used to transform the EMSS source counts. $f \sim 2$ is required to reconcile the EMSS and 2–10 keV source counts. This would imply either that the sources have relatively flat spectra, $\alpha \sim 0.4$, or that extra photoelectric absorption is present, cutting off the spectrum at low energies. While $\alpha \sim 0.4$ is, indeed, the spectrum of the background, the first of these possibilities seems unlikely given that the 2–10 keV spectra of both high and low luminosity AGN which dominate the resolved source counts have $\alpha \geq 0.7$ (Turner & Pounds 1989, Nandra 1992, Williams *et al.* 1992) and that the spectra of QSOs observed with *ROSAT* seem to be even steeper, $\alpha \sim 1.0$ (Shanks *et al.* 1991). Since low luminosity AGN are known to be preferentially intrinsically absorbed (Reichert *et al.* 1985, Turner & Pounds 1989), it seems feasible that the EMSS misses some of these sources. Indeed this may be the cause of the flattening of the EMSS AGN luminosity function below $L_x \sim 10^{43} \mathrm{erg\,s^{-1}}$. For a spectral index $\alpha = 0.8$ as used previously, then $f \sim 2$ requires $N_H \sim 5 \times 10^{21}\,\mathrm{cm^{-2}}$. This is barely consistent with the upper limit to the absorption obtained in the previous chapter.

4.5 Contamination from galactic sources

The $N(S)$ relation derived from the resolved sources of Piccinotti *et al.* and from the EMSS explicitly excludes the contribution from galactic sources. This contribution cannot be removed from the fluctuation measurements and its importance must be estimated. Piccinotti *et al.* identified 14 galactic sources in the 76 objects in their complete sample, a fraction of $\sim 20\%$. Four of these objects are high luminosity X–ray binaries; the luminosity function of these objects seems to truncate at $L_x \sim 10^{36} \, \text{erg s}^{-1}$ and it can reasonably be assumed that all such objects at $|b| > 20°$ have been detected by one of the all sky surveys. They may therefore be considered irrelevant to the fluctuation measurements.

Several authors have discussed the existence of a class of medium ($L_x \sim 10^{34} \, \text{erg s}^{-1}$) luminosity X–ray sources (see Worrall & Marshall (1983) and references therein for further details) which may be associated with Be star transient X–ray binary systems. The scale height (see below) of these sources is believed to be $\sim 50 \, \text{pc}$ and their space density (and hence volume emissivity) is also believed to be low, so they will not contribute strongly to the source counts derived from the fluctuations.

Most of the galactic sources in the EMSS are normal stars, but these have very soft (T $\sim 10^6$ K) spectra and are unlikely to contribute to the fluctuations at the energies considered here. The most important sources from the point of view of their impact on the fluctuations are the cataclysmic variables (CVs) and active cool star binaries. CVs typically have a hard spectral component with $kT = 10 - 20$ keV and luminosities $10^{32} \, \text{erg s}^{-1}$. The active cool star binaries include RS CVn systems and contact binaries; they have $kT \sim$ a few keV and luminosities up to a few $\times 10^{31} \, \text{erg s}^{-1}$. These sources are expected to belong to the disk population and have a characteristic scale height, h. The luminosity function may then be expressed thus

$$\phi(L, \mathbf{r}) = \phi(L) \exp(-(r/h) \sin |b|) \qquad (4.3)$$

where $\phi(L)$ is the luminosity function in the galactic plane. The scale height for CVs is probably ~ 300 pc [1], for RS CVn systems ~ 110 pc (Montle 1973) and the scale height for contact binaries is not known because their evolutionary path is not understood. Hard X–ray luminosity functions for the three classes of sources are not well determined and their space densities are poorly known. The sample of Piccinotti *et al.* contains 7 CV stars and 3 RS CVns, but no contact binaries. *Ginga* observed (and detected) 28 CV systems, 5 RS CVns and 1 contact binary system (over all galactic latitudes).

It can be shown (*e.g.* Shafer 1983) that for fluxes

$$S >> S_{\mathrm{Euc}} = \frac{L \sin^2 |b|}{4\pi h^2} \qquad (4.4)$$

the galactic source counts obey the Euclidean form, while for $S << S_{\mathrm{Euc}}$ the source counts roll over as $\exp(-S^{-1/2})$. Thus the contribution from galactic sources at the fluxes constrained by the fluctuations must be smaller than at the flux levels of Piccinotti *et al.* The source counts from the population of medium luminosity X–ray binaries discussed above roll over at $S \sim 6 \times 10^{-9}\,\mathrm{erg\,cm^{-2}\,s^{-1}}$ for $|b| = 25°$ and at even higher fluxes for higher galactic latitudes. For a CV of luminosity $10^{32}\,\mathrm{erg\,cm^{-1}\,s^{-1}}$ the critical flux is 1.6×10^{-12} $\mathrm{erg\,cm^{-2}\,s^{-1}}$ for a source at $|b| = 25°$ and for an RS CVn system at the same galactic latitude the value is slightly higher.

Shafer (1983) estimated the contribution of CVs and RS CVns as follows: the luminosity function for each class of source was assumed to be a power law with index $\beta = 2$ or 3; an L_{min} and an L_{max} were assumed for each class of source and the luminosity functions were normalised to predict the correct number of sources in the Piccinotti *et al.* sample. In this way he calculates maximum total contributions to $N(S)$ of 10%, 8% and 3% at $S = 10^{-11}, 10^{-12}, 10^{-13}$ $\mathrm{erg\,cm^{-2}\,s^{-1}}$ respectively. These luminosity functions are consistent with the numbers of these sources actually observed by *Ginga*, thus the limits on $N(S)$ quoted above can be applied to the *Ginga* fluctuations. A more detailed estimate

---

[1]Osborne *et al.* (1994) report the discovery of an AM Her system at an height $z > 630$ pc.

of the contamination would require the existence of a hard X–ray luminosity function. Since *Ginga* did not observe a complete sample of CV systems, such a luminosity function can not be derived from the *Ginga* data.

The possible contribution from contact binaries is very hard to quantify given the paucity of information on these systems. The fact that no contact binaries were detected in Piccinotti *et al.* implies that their contribution at any flux level cannot be more than $\sim 5\%$.

Thus the total contamination from galactic sources must be less than $\sim 10\%$. This is certainly not enough to bring the *Ginga* results into agreement with the EMSS results and implies that most of the fluctuations must be explained by extragalactic sources. This is, of course, the expected result given that the fluctuations do not show any trends with galactic latitude or longitude.

4.6   The contribution of clusters

The evidence so far seems to indicate that low luminosity AGN make a significant contribution to the background at the fluxes typical of the *Ginga* fluctuations. Clusters of galaxies will also be contributing, especially at low energies and high fluxes.

Piccinotti *et al.* find the following luminosity function for clusters

$$\frac{dN}{dL_{44}} \approx 3.5 \times 10^{-7} L_{44}^{-2.15} (10^{44} \, \mathrm{erg \, s^{-1}})^{-1} \mathrm{Mpc}^{-3} \qquad (4.5)$$

where L_{44} is the 2–10 keV X–ray luminosity in units of $10^{44} \, \mathrm{erg \, s^{-1}}$. The flatness of this luminosity function means that the cluster source counts are dominated by the high luminosity objects. This luminosity function has been used to predict the 2–10 keV cluster source counts following the method of Fabian & Rees (1978) which is summarised briefly below.

The number of sources per steradian out to a redshift z_{max} was calculated from

$$N(> S) = \int_{L_{min}}^{L_{max}} n(L, z = 0)dL \int_0^{z_{max}} \frac{[zq_0 + (q_0 - 1)(\sqrt{(2q_0 z + 1)} - 1)]^2}{q_0^4(1 + z)^3(1 + 2q_0 z)^{1/2}}dz \qquad (4.6)$$

(Weinberg 1972).

The second integral was integrated numerically for small increments ($z2 - z1$). The flux from sources at that redshift was then calculated from

$$S(z_2) = \frac{LH_0^2 q_0^4(\exp[-2(1 + z_2)/T] - \exp[-10(1 + z_2)/T])}{4\pi c^2(zq_0 - 1)(\sqrt{(2q_0 + 1)} - 1))^2} \qquad (4.7)$$

where T is the cluster temperature in keV.

Five luminosity bins were used with the minimum luminosity set to $0.1L_{44}$ erg s^{-1} and the maximum luminosity equal to $32L_{44}$ erg s^{-1}. For each bin a weighted luminosity was calculated and a bin temperature was calculated using:

$$T(\text{keV}) = 10^{-11.73} \times L_x^{0.28} \qquad (4.8)$$

(Edge & Stewart (1991a)). The dashed line in Figure 4.6 shows the expected behaviour of the cluster source counts calculated in this way. It can be seen that the cluster source counts fall below the Euclidean value very rapidly. This is due to the thermal spectra being redshifted out of the *Ginga* energy band. The volume emissivity of the cluster emission is $\sim 10^{38}$ erg s^{-1} Mpc^{-3} indicating that clusters contribute ~ 4 % of the 2-10 keV X-ray background (entirely consistent with the value found by Piccinotti *et al.* and Shafer).

In fact the luminosity function from clusters is known to exhibit strong, negative evolution (Edge *et al.* 1990, Gioia *et al.* 1990b). These first authors found that the differential luminosity function could be fit by

$$\log N = A - 2\log B + (L_x^{0.4} - 1)\log(1 - 1/B) - 0.6\log L_x \qquad (4.9)$$

representing a simple model of the stochastic merging of clusters, where B measures the number of elapsed collision times (hence B changes as $(1 + z)^{-3/2}$ in an Einstein–de Sitter universe). The mean collision time is found to be $\sim 1.6 \times 10^{10}$
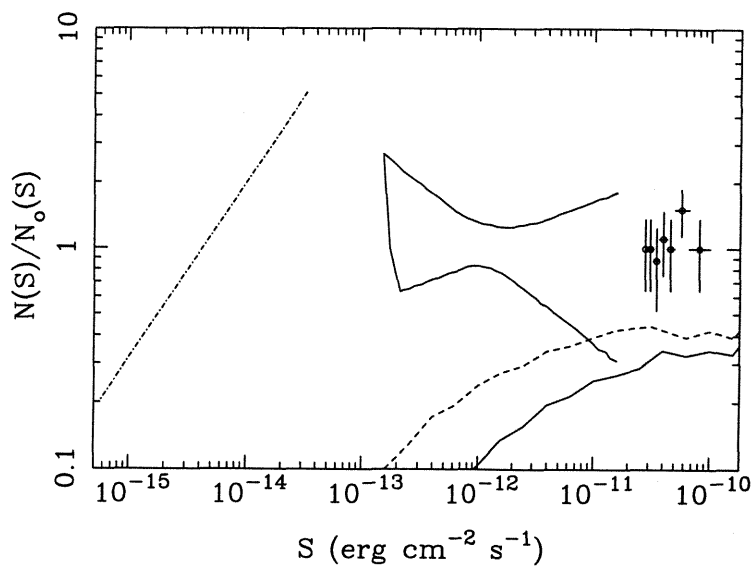
Figure 4.6: The expected form of the cluster source counts with (solid line) and without (dashed line) negative luminosity evolution.

years. The solid line in Figure 4.6 illustrates the expected form of the cluster source counts when negative evolution of this form is taken into account; a simple parameterisation $B = 0.92 + 0.83/(1 + z)^{3/2}$ is assumed. At fluxes corresponding to the level of the Piccinotti sample the source counts are at the correct level of $\sim 40\%$, but at lower fluxes the counts fall off even more rapidly than the counts with no evolution. Thus the total contribution of clusters to the 2–10 keV background is even less than that calculated from the HEAO-1 data by Shafer and Piccinotti *et al.*.

4.7 AGN source counts

Piccinotti *et al.* determined the following luminosity function for AGN (excluding BL Lacs)

$$\frac{dN}{dL_{44}} \approx 2.7 \times 10^{-7} L_{44}^{-2.75} (10^{44}\,\mathrm{erg\,s^{-1}})^{-1}\,\mathrm{Mpc^{-3}} \qquad (4.10)$$

The steepness of the luminosity function indicates that the source counts will be dominated by low luminosity objects and will depend only weakly on L_{max}. Piccinotti it et al. estimate L_{min} by requiring that the number of sources above their flux limit predicted by the luminosity function should not exceed the number observed in their sample. In this way they calculate that the luminosity function cannot continue as an unbroken power law below some $L_{\mathrm{min}} \sim 0.005 - 0.05 L_{44}$. Elvis *et al.* (1984) show that the luminosity function does indeed flatten to $\beta \sim -1.75$ below $L \sim 10^{-1.5} L_{44}$.

The AGN source counts were predicted in the same way as the cluster counts, for various values of the luminosity function parameters. Each decade of luminosity was divided into four bins. For each model various integral properties (the number of sources that would be expected above $3.16 \times 10^{-11}\,\mathrm{erg\,s^{-1}\,cm^{-2}}$, the integrated flux from the sources) were calculated and are summarised in Table 4.2. This table will be used to refer to the models by number. For comparison, the 2–10 keV XRB flux, calculated from

$$f(E) = 7.877 E^{-0.29} \times \exp(-E/41.13\,\mathrm{keV}) \qquad (4.11)$$

(Gruber, 1992) is $5.41 \times 10^{-8}\,\mathrm{erg\,cm^2\,s^{-1}\,sr^{-1}}$.

The sensitivity to L_{min} and the relative lack of sensitivity to L_{max} is clearly illustrated by comparing models 1, 2 and 3. The broken power-law luminosity function described above is then considered. The slope of the luminosity function was assumed to be -1.75 below L_{bk}, the break luminosity; the normalisation of the flatter part was adjusted to agree with the Piccinotti *et al.* luminosity function at L_{bk}.

Model	L_{min}	L_{max}	L_{bk}	L_{abs}	Column	Predicted number	Integrated flux
1	10^{42}	10^{45}				32.3	0.156
2	10^{42}	$10^{45.5}$				33.7	0.157
3	$10^{41.5}$	$10^{45.5}$				47.3	0.297
4	10^{42}	$10^{45.5}$	$10^{42.5}$			29.6	0.123
5	10^{41}	$10^{45.5}$	$10^{42.5}$			33.1	0.162
6	10^{41}	$10^{45.5}$	10^{43}			23.6	0.086
7	10^{42}	$10^{45.5}$	$10^{42.5}$	10^{43}	10	28.0	0.118
8	10^{41}	$10^{45.5}$	$10^{42.5}$	10^{43}	10	31.0	0.154
9	10^{41}	$10^{45.5}$	$10^{42.5}$	$10^{43.3}$	10	30.7	0.154
10	10^{41}	$10^{45.5}$	$10^{42.5}$	10^{43}	5	31.6	0.158

Table 4.2: Model parameters and integral properties of models of the AGN source counts without evolution. All luminosities are in $erg\,s^{-1}$, the column density is in units of $10^{21}\,cm^{-2}$, the predicted number is the number of sources in 8.23 steradians above $3.1 \times 10^{-11}\,erg\,s^{-1}\,cm^{-2}$, and the integrated flux is in units of $10^{-7}\,erg\,s^{-1}\,cm^{-2}\,ster^{-1}$.

It has already been mentioned that low luminosity AGN are commonly absorbed, so the counts were recalculated assuming that all AGN below some L_{abs} are absorbed by some column, N_H. (It is assumed that the luminosity function parameterises the unabsorbed luminosity). As expected, the absorption does not greatly affect the expected number of sources in the 2-10 keV band.

Figure 4.7 shows the predicted AGN source counts from some of the models described in Table 4.2, The source counts follow the Euclidean form down to much lower flux levels than clusters since the effects of redshifting the AGN spectra are much less dramatic.
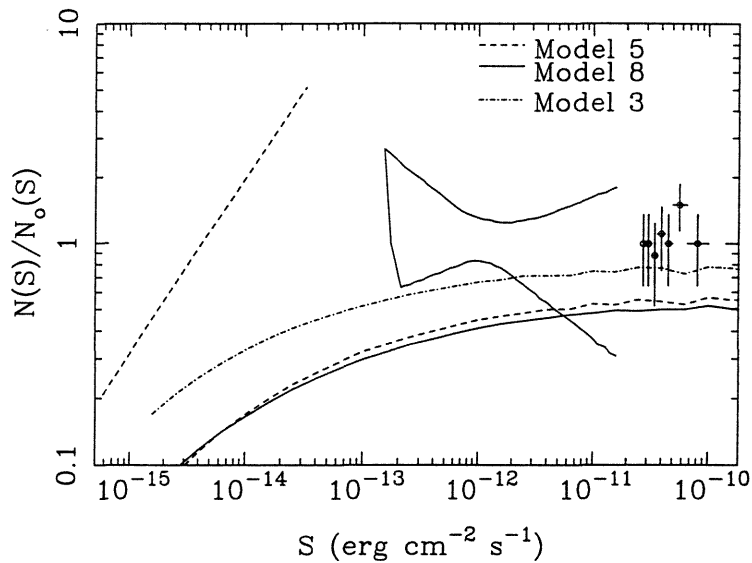
Figure 4.7: The 2–10 keV AGN source counts, ignoring evolutionary effects for the models described in Table 4.2 and in the text. The curve depicting the source counts for model 2 (not shown) is virtually coincident with the curve shown for model 5.

4.7.1 BL Lacertae objects

Only four BL Lac objects were detected in the Piccinotti sample (a total contribution of $\sim 5\%$); consequently no luminosity function could be derived. BL Lacs have significantly steeper spectra then most other AGN – typically $\alpha = 1.5$ (Fink *et al.* 1992). In the absence of evolutionary effects this means that the BL Lac source counts will behave like those of clusters as the effects of redshift will rapidly become important.

The BL Lac source counts deduced from the EMSS are significantly flatter than the Euclidean prediction (Maccacaro *et al.* 1984). Morris *et al.* (1991) define a flux limited sample of X–ray selected BL Lacs from the EMSS for which redshifts have been measured and show that there is strong negative evolution of the BL
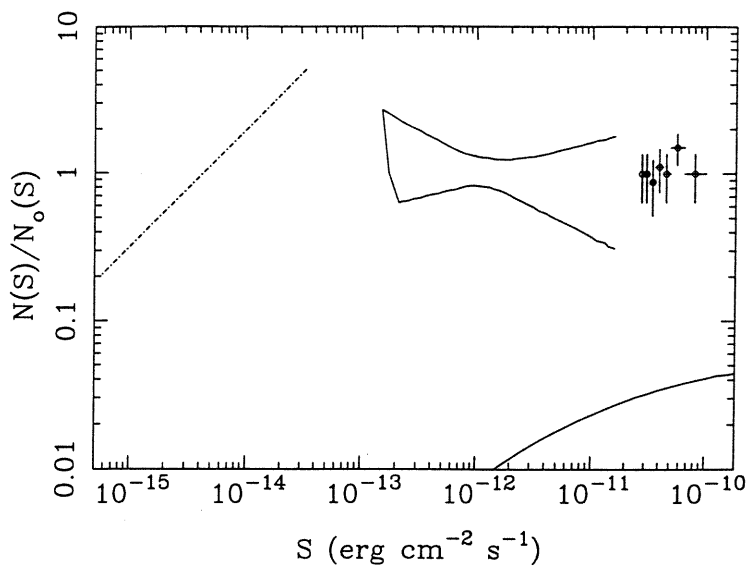
Figure 4.8: The 2–10 keV BL Lac source counts, including negative luminosity evolution for the model described in the text.

Lac population. They conclude that the contribution of BL Lac objects to the soft X–ray background is only $\sim 3 - 4\%$. Figure 4.8 shows the BL Lac source counts predicted from the luminosity function of Morris *et al.* (1991) with $\gamma = -7.0$ luminosity evolution. The number predicted in the Piccinotti sample is 2.2 and the contribution to the XRB flux, integrated to a redshift of 2.5, is $\sim 1\%$.

Figure 4.9 shows the summed (cluster+evolution), (agn, no evolution - model 8) and (BL Lac+evolution) counts. At fluxes greater than $\sim 5 \times 10^{-12}$ the model counts are consistent with resolved source counts and the fluctuations constraints, but at lower fluxes the predicted counts fall off below the fluctuation region (this is the 'negative invariant excess' of Shafer (1983)). AGN are known to evolve in the opposite sense to clusters - ie they are more luminous at higher redshifts - so this effect is now considered.
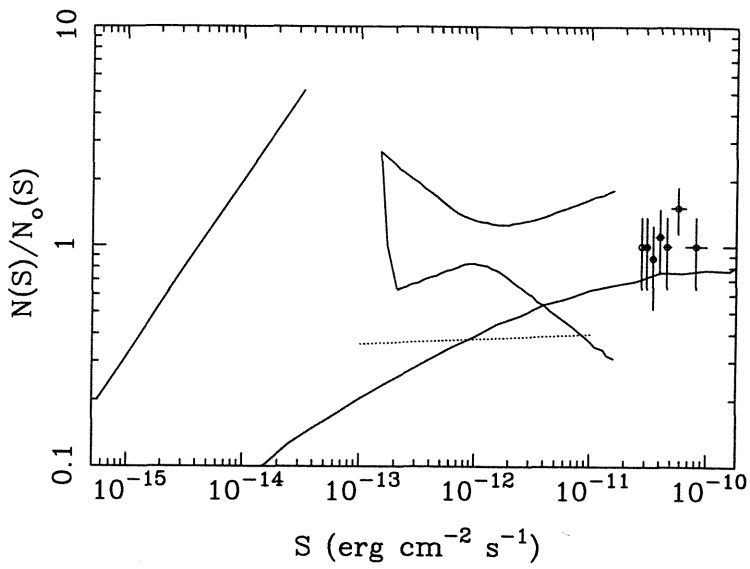
Figure 4.9: The 2–10 keV (AGN + cluster + BL Lac) source counts. The contributions of clusters and BL Lacs include the effects of evolution, the contribution of AGN does not.

4.8 Including AGN evolution

The AGN are assumed to undergo pure luminosity evolution. Models of luminosity evolution have traditionally been of two types:

exponential evolution;

$$L_x(z) = L_x(0)e^{C\tau(z)} \qquad (4.12)$$

where $\tau(z)$ measures the elapsed time from emision.

and power law evolution;

$$L_x(z) = (1+z)^A L_x(0) \qquad (4.13)$$

The first form of evolution seemed to be favoured by the EMSS data (Maccacaro *et al.* 1991). The latter form of evolution is favoured by both optical (Boyle *et al.* 1991) and ROSAT (Boyle *et al.* 1993) data and will be considered here. These authors find that, in a $q_0 = 0.5$ universe, then the best fit value of A is $A = 2.5$; this requires a redshift cutoff at $z = 2.0$.

The maximum redshift is taken to be either 2.0 or 2.5. It is assumed that source with emitter frame luminosities greater than L_{abs} are unabsorbed. Table 4.3 shows model parameters and integral properties of models of source counts including luminosity evolution. Models indicated with a * have been computed by integrating to a maximum redshift $z = 2$.

Models which extend to low luminosities overproduce the XRB if the evolution parameter $A > 2$ or if $z_{max} > 2$.

Figure 4.10 shows the predicted source counts for the some of the models described in Table 4.3. It illustrates the effect of varying either A or z_{max}. It can be seen that these models 'fill in' some of the deficit left by models which do not contain evolution but that care must be taken not to overproduce the X-ray background.

Model	L_{min}	L_{max}	L_{bk}	L_{abs}	Column	A	Predicted number	Integrated flux
1	10^{41}	$10^{45.5}$	$10^{42.5}$	10^{43}	10	2.0	34.3	0.40
2	10^{41}	$10^{45.5}$	$10^{42.5}$	10^{43}	10	2.5	35.0	0.58
3	10^{41}	$10^{45.5}$	$10^{42.5}$	10^{43}	10	3.0	36.2	0.871
4	$10^{42.5}$	$10^{45.5}$	$10^{42.5}$	10^{43}	10	2.5	25.6	0.303
5	$10^{42.5}$	$10^{45.5}$	$10^{42.5}$	10^{43}	10	2.0	25.1	0.22
6*	$10^{42.5}$	$10^{45.5}$	$10^{42.5}$	10^{43}	10	2.5	25.6	0.261
7*	10^{41}	$10^{45.5}$	$10^{42.5}$	10^{43}	10	2.5	35.0	0.519
8*	$10^{42.5}$	$10^{45.5}$	$10^{42.5}$	10^{43}	10	2.0	25.1	0.198

Table 4.3: Model parameters and integral properties of models of the AGN source counts with luminosity evolution. All luminosities are in $erg\,s^{-1}$, the column density is in units of $10^{21}\,cm^{-2}$, the predicted number is the number of sources in 8.23 steradians above $3.1 \times 10^{-11}\,erg\,s^{-1}\,cm^{-2}$, and the integrated flux is in units of $10^{-7}\,erg\,s^{-1}\,cm^{-2}\,ster^{-1}$.
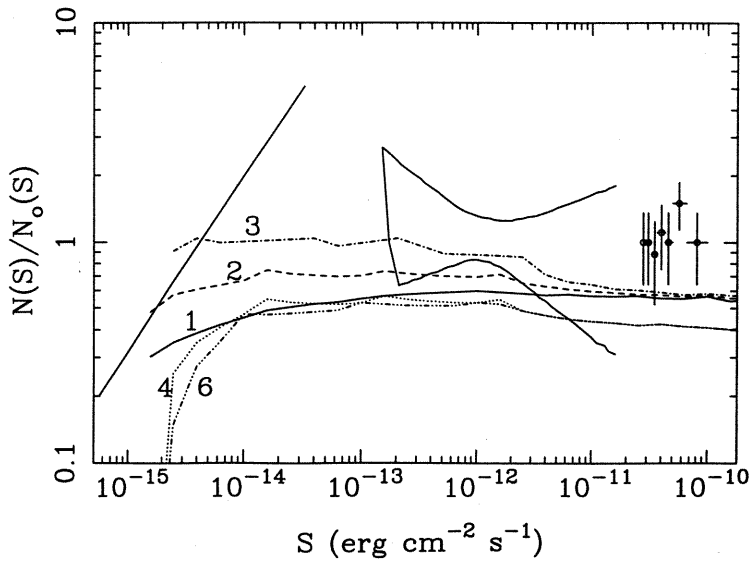
Figure 4.10: The 2–10 keV AGN source counts, assuming pure luminosity evolution for the models described in Table 4.3 and in the text.

4.9 Comparison with the EMSS (revisited)

The luminosity functions and model parameters described above were used to predict the counts in the EMSS band (0.3–3.5 keV).

Models with $L_{min} < 10^{42.5}$ overpredicted the EMSS counts by a factor ~ 2. Thus this section considers models with $L_{min} = 10^{42.5}$ (see also Butcher *et al.* 1994). Low luminosity AGN with $L_x < 10^{42.5}$ are known to exist; the need to truncate the luminosity function at $L_{min} = 10^{42.5}$ indicates either that the slope of the luminosity function below this point is much flatter than assumed, or that the assumptions about evolution are incorrect - possibly low luminosity AGN evolve less rapidly than higher luminosity AGN. Figure 4.11 shows the differential model counts in the 0.3-3.5 keV band, for the some of the models described in Table 4.3, normalised to the best N(S) curve for the EMSS AGN described by

$$N(> S) = 1.62 \times 10^{-17} S^{-1.61} \qquad (4.14)$$

(Della Ceca *et al.* 1992).

The curve for Model 8 gives an acceptable estimate of the EMSS source counts.

4.10 Summary

There appears to be an area of parameter space round $L_{min} = 10^{42.5}$, $A \sim 2$ and $z_{max} = 2.0$ where model AGN source counts can successfully reproduce both the 2–10 keV and the 0.3–3.5 keV source counts. The allowed range of parameter space is, perhaps, rather large but this is only to be expected given the paucity of some of the relevant observational data. In practice, one can expect that the situation is considerably more complex than the simple models considered here; for example, both L_{abs} and the absorbing column are probably drawn from a continuous distribution rather than the sharp cutoffs assumed here.

The value of A required here is below that indicated by the available X–ray and

83
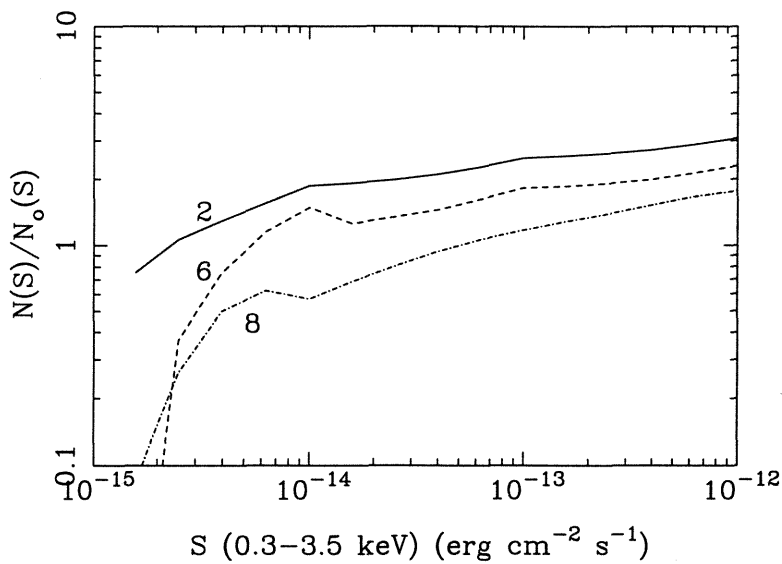
Figure 4.11: Model source counts in the 0.3-3.5 keV range normalised to the best fit N(S) curve for the EMSS.

optical data but, given the other uncertainties in the models, the difference is not alarming. Indeed the model source counts presented in Butcher *et al.* (1994), which assume that the AGN have spectra with $\alpha = 0.7$, yield acceptable results with $A = 2.5$. In Butcher *et al.* it is also shown that the summed spectra of sources (clusters and AGN) brighter than $S = 10^{-12} \, \mathrm{erg \, cm^{-2} \, s^{-1}}$ is fit by a power law of slope $\alpha = 0.76$ between 3–10 keV, consistent with the measured fluctuations spectrum.

Figure 4.12 shows the final model source counts from clusters, BL Lacs and AGN ('best buy' model 8 in Table 4.3).

A more complete consideration of AGN source counts would assume more complex AGN spectra. Madau *et al.* (1994) consider a reflection model for AGN spectra, with a distribution of absorbing columns with mean $N_H = 10^{24} \mathrm{cm^{-2}}$. They find that such a model successfully reproduces both the soft and hard source
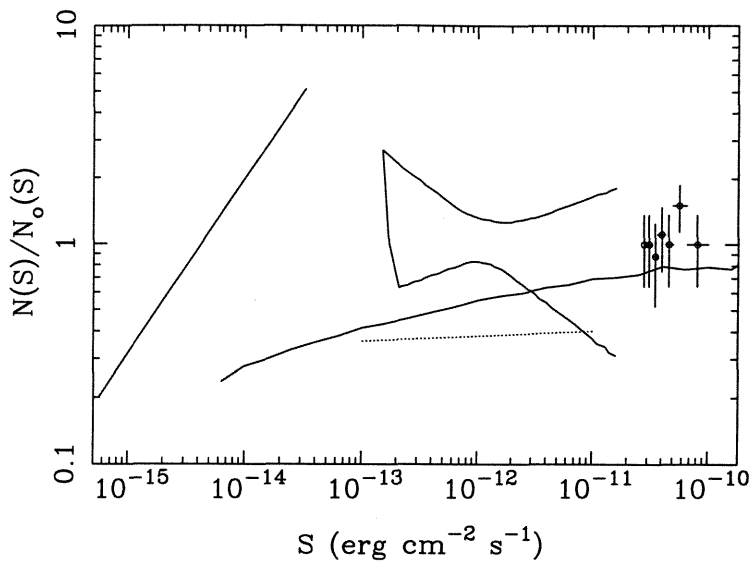
Figure 4.12: Final extragalactic source counts from the summed contributions of clusters, BL Lacs and AGN.

counts and the XRB spectrum. The discovery of more objects comparable to the highly absorbed, strong iron line source NGC 6552 (Fukazawa *et al.* 1994) will be crucial in validating these models.

Chapter 5

Clusters of Galaxies —
an overview

Overview

This chapter reviews previous observations of clusters and summarises some of the relevant theoretical background.

5.1 Introduction

Clusters of galaxies are the most massive gravitationally bound structures in the universe. They contain tens to hundreds of galaxies in a volume of a few Mpc^3, with virial masses of $10^{13} - 10^{15} M_\odot$. The visible mass in clusters is estimated to be typically a factor of 10 less than this and is comprised of approximately equal contributions from galaxies and from hot ($10^7 - 10^8$ Kelvin) gas, held in the gravitational potential well of the cluster. This gas is at densities of $\sim 10^{-3}\text{cm}^{-3}$ and cools via thermal bremsstrahlung, emitting primarily at X–ray wavelengths. The X–ray properties and theoretical models of clusters are reviewed extensively in Sarazin (1988). The reader is referred to this work and references therein for a more complete introduction to this subject.

5.2 Previous observations of clusters

5.2.1 Optical observations

The tendency for galaxies to cluster was noted by many observers in the last century, but was first studied in detail by Wolf (1906). Abell (1958) compiled the first statistically complete catalogue of rich clusters of galaxies in the northern hemisphere; for over 30 years this work has been the most important resource in the study of clusters. A similar study of the southern sky has also been completed (Abell, Corwin & Olowin 1989). These catalogues were compiled by visual inspection of the Palomar and UK Schmidt Sky Survey plates and estimates were made of the cluster richness and distance. Obviously, catalogues compiled in such a manner are vulnerable to contamination from projection effects and more accurate determinations of cluster properties require spectra to be taken (and hence redshifts measured) for many galaxies in the cluster. The development of multi-object spectroscopy using fibre optics has made possible much more detailed studies of cluster redshifts. This has increased the number of clusters with well measured velocity dispersions and shown that velocity substructure is very common (Colless 1987, Dressler & Schectman 1988).

Several optical classification schemes for clusters exist, based on their morphology. These systems are highly correlated and there seems to be a crudely one dimensional sequence running from regular to irregular. Table 5.1 taken from Sarazin (1988) summarises the various optical schemes. The galactic content of a cluster is also highly correlated with its optical classification. The inner regions of regular, compact clusters contain primarily elliptical and SO galaxies (spiral fraction $\sim 10\%$), while poor, irregular clusters have higher spiral fractions $\sim 50\%$. About 20% of rich clusters and other, poorer groups contain cD galaxies, the most luminous non-nuclear galaxies known. In contrast to the galactic content of clusters, the magnitude of cD galaxies has been considered to depend only weakly on optical cluster richness (dispersion $\sim 0^m.3$). For this reason they are

Property	Regular	Intermediate	Irregular
Zwicky Type	Compact	Medium–Compact	Open
Bautz–Morgan Type	I.I-II.II	II.II-III	II-III.III
Rood–Sastry Type	cD.B.L.C	L.C.F	F.I
Galactic Content	Elliptical-rich	Spiral-poor	Spiral-rich
E : S0 : Sp	3 : 4 : 2	1 : 4 : 2	1 : 2 : 3
Morgan Type	ii	i-ii	i
Oemler Type	cD.Spiral-poor	Spiral-poor	Spiral-rich
Symmetry	Spherical	Intermediate	Irregular
Central Concentration	High	Moderate	Low
Subclustering	Absent	Moderate	Significant
Richness	Rich	Rich–Moderate	Rich–Poor
	$n^* \approx 10^2$	$n^* \gtrsim 10^1$	$n^* \gtrsim 10^0$

Table 5.1: Summary of optical classification schemes for clusters taken from Sarazin 1988.

often used as 'standard candles' in cosmological studies. Most, perhaps all, cD galaxies are at the centres of cooling accretion flows and many are radio sources.

Linked to both cooling flows and radio activity is the optical line emission observed in clusters from gas at $\sim 10^4$ Kelvin (see Baum 1992 for an extensive review of this topic). Line emission nebulae are observed in the inner ~ 10 kpc of cooling flow clusters only. However, not all cooling flow clusters contain such nebulae. The line luminosity of a cluster correlates well with the X–ray mass accretion rate (Johnstone *et al.* 1987), but the scatter is very large. These emission line nebulae have traditionally been interpreted as thermal instabilities condensing out of the hot ICM, but more detailed observations have challenged this view (Baum 1992).

An important new development in optical studies of clusters has been the discovery (Lynds & Petrosian 1986, Soucail *et al.* 1987) of gravitationally lensed images of background galaxies, known as gravitational arcs and arclets (see Soucail 1992 for a review). Giant luminous arcs are typically $\sim 20''$ long and most of them are unresolved. At lower surface brightnesses there exist a large number of arclets, tangentially extended objects, usually very blue. The arcs are at higher redshifts than the cluster, confirming their origin. Such arcs provide both an important tool for studying distant field galaxies and a way of tracing the gravitational po-

tential (dark matter distribution) in clusters that does not depend on dynamical studies.

5.2.2 Radio Observations

Many clusters contain radio sources, usually associated with galaxies in the clusters. About 20% of local, strong radio galaxies are located in rich clusters, with more powerful sources usually found near the cluster centre and often associated with optically dominant galaxies (*e.g.* McHardy 1979). Radio sources in clusters usually have steeper spectra ($\alpha > 1$) than field radio sources and the steepness of the radio spectrum increases with cluster richness (McHardy 1979).

Radio maps of clusters show complex structure; Figure 5.1 shows a 1400 MHz continuum map of the Perseus cluster made with the Westerbork telescope as an example (the figure is taken from Jaffe 1992). Radio galaxies in clusters generally don't have the symmetrical double structure of isolated objects. Cluster radio galaxies have morphologies ranging from Wide Angle Tails (two lobes, not aligned with the galaxy nucleus) through to Narrow Angle Tails (radio emission all on one side of the galaxy). The equipartition pressures in the tails are generally in good agreement with the thermal pressures derived from X–ray data (see however Feretti, Perola & Fanti 1992). Some clusters also have clumpy, extended, radio halos; well known examples are Coma, A2256 and A2319. In Perseus the radio haloes seem to be associated with the two radio galaxies NGC 1275 and NGC 1272, but in no other case is the halo associated with a radio galaxy. Radio haloes also have steep spectra ($\alpha \sim 1.2$). Faraday rotation measurements towards background or cluster radio sources can be used to estimate intra-cluster magnetic fields but interpretation of the data is made complicated by the fact that radio galaxies have intrinsic rotation measure of their own. Turbulent dynamo models predict a field of $B_T \sim 50\mu G$ near cooling flow radio sources (Jaffe 1992).

Clusters have also been studied at 21cm, to try and trace the cooled gas below 1000 Kelvin. 21cm absorption has so far been detected in four clusters: Perseus,

89

Peak flux = 6.2933E-01 JY/PIX
Levs = 1.5733E-04 * (-3.00, -2.00, -1.00,
1.000, 2.000, 3.000, 4.000, 5.000, 6.000,
7.000, 8.000, 9.000, 10.00, 20.00, 30.00,
40.00, 50.00, 100.0, 200.0, 400.0, 1000.,
2000., 3000., 4000.)
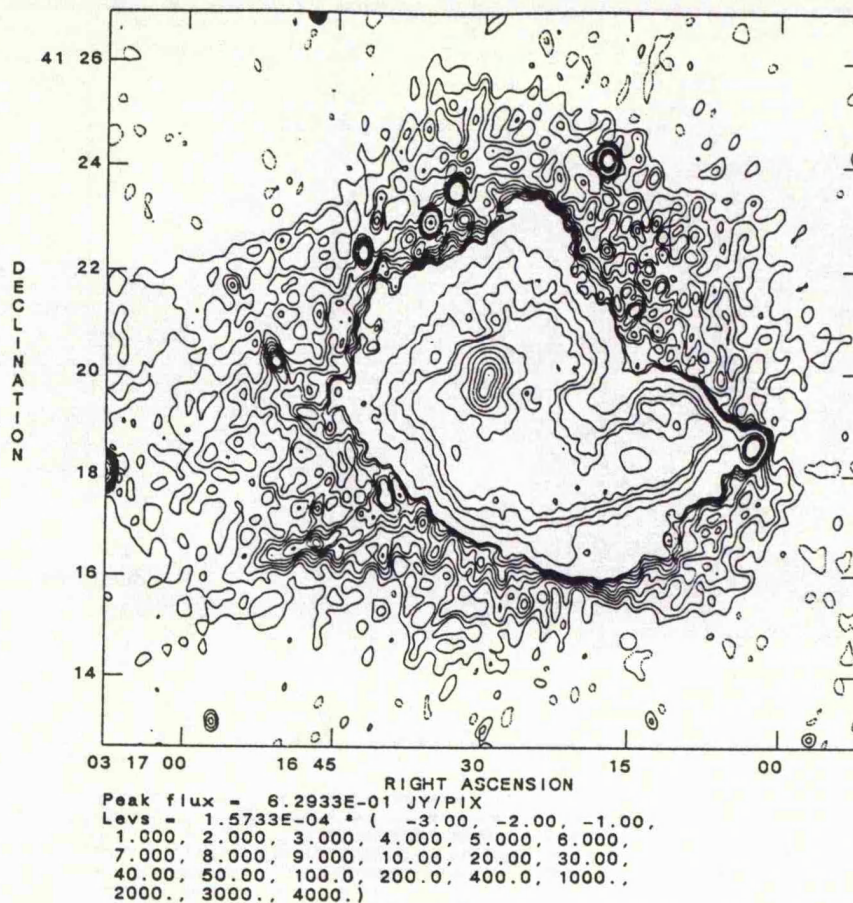
Figure 5.1: A 1400 Mhz map of the Perseus cluster, made with the Westerbork telescope by Sijbreng & de Bruyn. Taken from Jaffe (1992).

A0335+096, MKW3s and Virgo (Jaffe 1992 and references therein). 21cm emission has only been observed in Virgo. The masses of gas inferred in emission and absorption ($10^9 - 10^{10} M_\odot$) are only a small fraction of the $10^{12} M_\odot$ required to produce the X–ray absorption seen in cooling flow clusters (White *et al.* 1991) and the limits on HI emission require that the remaining neutral gas must be optically thick. Searches for small clouds of cold gas are ongoing (Jaffe 1992). 21cm observations also show that ellipticals and SOs in clusters have little neutral hydrogen, while spirals in clusters tend to be HI deficient compared to field galaxies.

SZ effect

Microwave background photons passing through the hot ICM are Thompson scattered, leading to a decrement in the Rayleigh Jeans (microwave) region of the spectrum and in increment in the millimetre (Wien) region. This is known as the Sunyaev Zel'dovich effect (Sunyaev & Zel'dovich 1972, see Birkinshaw 1991 and Lasenby 1992 for a summary of recent results). This effect is independent of redshift, leading to a method of determining H_0 independent of the distance ladder. Results from recent attempts to employ this technique are summarised below:

Cluster	H_0 (km s^{-1} Mpc^{-1})	Reference
A2218	24 ± 10	McHardy *et al.* 1990
A665	$(40 - 50) \pm 12$	Birkinshaw, Hughes & Arnaud 1991
A2218	57 ± 12	Hughes & Birkinshaw 1994

The largest experimental uncertainties are the zero offset of the SZ effect measurement and the lack of detailed knowledge of the cluster spatial temperature profile. This latter point will be addressed by Asca and by other future hard X-ray imaging satellites. The former problem is expected to be ameliorated by the refurbished and renamed Ryle Telescope at Cambridge which is bringing the benefits of interferometry to the field (Lasenby 1992).

5.2.3 Infra-red observations

Thermal dust emission of cD galaxies from IRAS observations was reported by three groups in 1990 (see Bregman (1992) for a review of the results). Bregman also describes the results of the study of a complete sample of Abell clusters; far infrared emission was detected in about 12% of clusters. The average properties of detections were: $< z >= 0.06$, $< L_{FIR} >= 3 \times 10^{44}$ erg s^{-1} and $< T >=25$-30 K. The infrared luminosity within the cooling radius is ~ 10 times the X-ray luminosity.

Wise *et al.* (1993) report the discovery of extended, diffuse, far-infrared emission from the clusters A262 and A2670. There is evidence that poorer clusters emit more strongly in the far-infrared but the sample sizes are small and the authors advise caution.

5.2.4 X–ray observations

M87 in the Virgo cluster was the first extragalactic object to be identified as an X–ray source (Byram, Chubb & Friedman 1966, Bradt *et al.* 1967). The *UHURU* satellite, launched in 1970, performed the first all sky survey in the X–ray band (Giacconi *et al.* 1972, 1974, Forman *et al.* 1978). Many more clusters were confirmed as X–ray sources (Gursky 1971a & b) and it was shown that the emission was extended (Kellogg *et al.* 1972). The discovery of an iron line in the ICM of Perseus (Mitchell *et al.* 1976, Sermelitsos *et al.* 1977) confirmed the thermal nature of the emission and showed that a significant fraction of the ICM had been processed through an early generation of stars.

Mushotzky (1984) reviews the spectral results on clusters from pre-*EXOSAT* satellites; X–ray temperature is highly correlated with luminosity. Rothenflug & Arnaud (1985) used HEAO-1 spectra to determine iron abundances for 22 clusters. The results are consistent with an uniform abundance of 0.4 solar for all clusters. HEAO-1 results showed evidence for non-isothermal spectra in some clusters (Mitchell & Mushotzky 1980, Henriksen & Mushotzky 1985).

The *EINSTEIN* observatory (Giacconi *et al.* 1979) was the second (after Copernicus which had very limited sensitivity) satellite with focussing X–ray optics. Over 200 clusters were observed with the IPC or HRI. The two major surveys of *EINSTEIN* observations are in Abramopolous & Ku (1983) and Jones & Forman (1984). The X–ray surface brightness profiles were generally well described by King profiles (see below) in their outer regions, but many clusters showed strongly peaked excess emission in their cores, indicating much denser gas. This was the first evidence for the existence of cooling flows in clusters (Stewart *et al.* 1984).

A more sophisticated method for analysing cluster images is the deprojection technique developed by Fabian and co-workers in Cambridge (see for example Fabian *et al.* 1981, Stewart *at al.* 1984, Arnaud 1988). This calculates the contribution from a radial shell of cluster emission to a circular ring in the surface brightness profile. If S_i is the surface brightness in the ith bin ($i = 1$ is the outer bin) and C_i is the emissivity in the ith shell then:

$$S_i = \sum_{j=1}^{i} A_{ij} C_j \qquad (5.1)$$

where A_{ij} is a matrix of geometrical factors. Only shells with $j \leq i$ contribute to the surface brightness of bin i so A_{ij} is triangular and equation 5.1 may be iteratively solved for C_j by starting at the first bin and working in. These values of C_j may be used to determine the density and temperature of the gas if a form for the gravitational potential is assumed. The cooling time of the gas can be calculated from these profiles; if the central cooling time is less than the age of the cluster $\sim H_0^{-1}$ then the cluster contains a cooling flow. Arnaud (1988) analysed 106 IPC and HRI images of clusters and found that 43 had cooling flows.

Gioia *et al.* (1990b) have analysed a sample of 67 clusters from the EMSS. They find that the X–ray luminosity functions for their highest and lowest redshift bins are different at the 3σ level, in the sense that there are fewer high luminosity clusters at high redshifts.

EINSTEIN also carried three spectroscopic instruments; two in the focal plane of the telescope and one co-aligned.

The Solid State Spectrometer (SSS) had a field of view of 3 arcmin diameter and a constant energy resolution of 160 eV over the energy range 0.5–4.5 keV (Holt *et al.* 1979). The SSS detected K-lines from Mg, Si and S and L-lines from Fe, in the spectra of Virgo/M87, Perseus, A496 and A576 (Mushotzky *et al.* 1981, Lea *et al.* 1982, Nulsen *et al.* 1982). The observations of Virgo require nearly solar abundances of S and Si, while the iron abundance in Perseus was found to be about half the solar value (Mushotzky *et al.* 1981). No evidence for strong abundance gradients was found (Mushotzky *et al.* 1981, Lea *et al.* 1982). The

93

SSS also showed evidence of cooler gas at the centre of the cluster; mass accretion rates calculated from the distribution of this cool gas were in good agreement with those determined from X–ray images (Mushotzky & Szymkowiak 1988). White *et al.* (1991) recently analysed the SSS spectra of 21 clusters. They found that 12 of these clusters showed evidence for excess absorption above that predicted from galactic column densities. These 12 clusters also required an extra emission component which was modelled as a simple cooling flow spectrum. The inferred mass of cold gas was $\sim 10^{12} M_\odot$ within a typical cooling radius of ~ 20 kpc.

The Focal Plane Crystal Spectrometer (FPCS) had a 30×3 arcmin field of view with high energy resolution in a few selected energy bands. It detected O K-lines and Fe L-lines in cooling flow clusters (Canizares *et al.* 1979, 1982, Canizares, Markert & Donahue 1988). These lines are characteristic of gas at $\sim 10^6$ Kelvin and the Fe L-lines cannot be explained by gas at any single temperature. Mass accretion rates derived from line strengths were also in good agreement with results from imaging data (Canizares, Markert & Donahue 1988). An interesting result from the FPCS observations was that oxygen appeared to be a overabundant by a factor of 3 relative to iron. This has important implications for the origin of the intracluster medium.

The Monitor Proportional Counter (MPC) was co-aligned with the *EINSTEIN* telescope. The FWHM field of view was 45×45 arcmin and the energy resolution was mediocre, with 8 energy bins for the range 2–20 keV.

EXOSAT was launched in 1983 (the mission is reviewed in White & Peacock 1988). The two experiments relevant for cluster work were the low (0.04–2 keV) energy telescopes (LE) with $\sim 18''$ resolution and a medium energy proportional counter (ME) with a 45×45 arcmin field of view and moderate energy resolution, $E/\Delta E \sim 3 - 8$ over 1–20 keV (Turner, Smith & Zimmermann 1981). *EXOSAT* observations of 45 clusters are presented in Edge (1989) and Edge & Stewart (1991a). The LE was insensitive to low surface brightness objects and analysis of the images did not generally yield estimates of core radius or β which were

an improvement over those derived from *EINSTEIN*. Deprojection of the surface brightness profiles showed that ~ 90 % of the sample had cooling flows. Analysis of the ME spectra showed that isothermal models were good fits to the data. The results were consistent with an uniform iron abundance of 0.32 solar for all clusters, with Coma the only cluster to deviate significantly from this mean. The three nearby, bright clusters, Virgo, Perseus and Coma were extensively observed by *EXOSAT* and a series of offset pointings were performed. A radial temperature gradient was discovered in Coma, (this is discussed more extensively in the next chapter), but no strong iron abundance gradients were detected. Edge & Stewart (1991b) describe correlations between the X–ray properties of clusters in the sample and various optical, infra-red and radio properties taken from the literature.

A flux limited sample of 46 clusters has been compiled from the all-sky surveys of HEAO-1 and Ariel V. Confusion problems were alleviated by observations with *EINSTEIN* and the *EXOSAT* LE. The temperatures of most of the clusters were measured by either the HEAO-1 A2, *EXOSAT* ME or the *EINSTEIN* MPC. Edge *et al.* (1990) find a significant deficiency of high luminosity clusters in the redshift range 0.1–0.2. This indicates rapid X–ray luminosity evolution in the same sense as the EMSS results of Gioia *et al.* 1990b.

The X–ray study of clusters suffers from the same problem as the study of the XRB, mentioned in Chapter 2. Images of clusters are only available in the soft band, while high quality spectra are available in the 2–10 keV band. The questions about clusters which we wish to answer involve their radial temperature profiles and the spatial distribution of heavy elements. The next generation of X–ray satellites (Jet-X, Asuka) will begin to provide the 0.5–10 keV spatially resolved spectra necessary to address these questions, but there have been several attempts to circumvent the problems which are described below.

Spartan I was a narrow slit collimator experiment flown on the space shuttle in 1985 (Ulmer *et al.* 1987). Strip scans of the Perseus cluster enabled an 'almost im-

age' of the cluster to be built up. The results have been very controversial; Kowalski *et al.* (1993) claim the existence of a strong central concentration of iron with a central abundance of 0.8 ± 0.3 solar and a linear gradient of $-1.10^{+0.9}_{-2.2}\,\mathrm{Mpc}^{-1}$. The temperature is found to fall in the inner, cooling flow, region of the cluster and is isothermal in the outer regions.

The SL2 XRT was a coded mask telescope flown on the space shuttle in 1985. The coded mask technique is well suited to studying the distribution of point sources but the analysis of extended, low surface brightness objects such as clusters is very complicated. 4 clusters were observed; hard X–ray morphologies of Coma, Perseus and Ophiuchus are presented in Ponman *et al.* 1991. The spectral results for the Perseus cluster (Ponman *et al.* 1990, Eyles *et al.* 1991) have fuelled the controversy over the heavy element distribution in this cluster. The central iron abundance was claimed to be 1.3 ± 0.2 solar, dropping to < 0.2 solar at ~ 25 arcmin radius. The temperature profile was found to be a minimum in the centre of the cluster, rise to a maximum and then fall off in the outer regions of the cluster. Observations of other clusters (Watt *et al.* 1992) show no evidence for any abundance gradients.

The Broad Band X–Ray Telescope (BBXRT) was part of the Astro package flown on a seven day shuttle mission in December 1990 (Serlemitsos *et al.* 1991). It had good spectral resolution ($E/\Delta E \sim 5$ at 6 keV), a wide bandpass (0.3–12 keV) and crude spatial resolution (one central pixel of 2 arcmin radius and four outer pixels of 8 arcmin radius). The mission suffered from severe pointing problems and only seven clusters were observed with exposures greater than 1000 seconds. Preliminary results are described in Mushotzky (1992) and references therein. Cool gas is detected in the cooling regions of many clusters and the excess absorption discovered by White *et al.* 1991 is confirmed. An oxygen absorption feature is detected in the extension to the cluster emission in A2256 seen with *ROSAT* (Briel *et al.* 1991. The results for Perseus (Arnaud *et al.* 1991) appear to be inconsistent with the Spartan and Spacelab results described above. There is evidence for only a weak abundance gradient (from comparing the BBXRT

abundance measurement to that determined by broad beam instruments). In fact this is the case for all the clusters observed.

5.3 Some relevant theoretical concepts

5.3.1 Mass determinations

Optical

The traditional optical method of determining cluster masses involves treating the galaxies as test particles and studying their dynamics. As shall be seen, this requires assumptions about the galaxy orbits which may not be justified. This method was first applied by Zwicky (1933). The clusters are assumed to be bound, hence

$$E = T + W < 0 \qquad (5.2)$$

where E is the total energy, T is the galaxies' kinetic energy and W is the gravitational potential energy:

$$T = \frac{1}{2} \sum_i m_i v_i^2 \qquad (5.3)$$

$$W = -\frac{1}{2} \sum_{i \neq j} \frac{G M_i m_j}{r_{ij}} \qquad (5.4)$$

The sums are over all the galaxies, m_i and v_i are the ith galaxy mass and velocity and r_{ij} is the separation of galaxies i and j.

The equations of motion of the galaxies may be integrated to give;

$$\frac{1}{2} \frac{d^2 I}{dt^2} = 2T + W \qquad (5.5)$$

where $I = \sum_i m_i r_i^2$ = the total moment of inertia. Assuming a stationary cluster distribution then the left hand side of equation 5.5 is zero and:

$$W = -2T, \quad E = -T \qquad (5.6)$$

ie the virial theorem. The total mass $M_{tot} = \sum m_i$ and a mass weighted velocity dispersion and gravitational radius may be defined

$$< v^2 > = \frac{\sum m_i v_i^2}{M_{tot}} \qquad (5.7)$$

$$R_G = 2M_{tot}^2 \left(\sum_{i \neq j} \frac{m_i m_j}{r_{ij}} \right)^{-1} \qquad (5.8)$$

Substituting these into 5.6

$$M_{tot} = \frac{R_G < v^2 >}{G}. \qquad (5.9)$$

For isotropic orbits

$$< v^2 > = 3\sigma_r^2 \qquad (5.10)$$

where σ_r is the mass weighted radial velocity dispersion, so

$$M_{tot} = \frac{3R_G \sigma_r^2}{G} = 7 \times 10^{14} M_\odot \left(\frac{\sigma_r}{1000 \text{km s}^{-1}}^2 \right) \left(\frac{R_G}{\text{Mpc}} \right) \qquad (5.11)$$

R_G may be estimated from fits to the galaxy distribution, from strip counts of galaxies or from $R_G = (\pi/2)b_G$ where

$$b_G = 2M_{tot}^2 \left(\sum \frac{m_i m_j}{b_{ij}} \right)^{-1} \qquad (5.12)$$

and b_{ij} is the projected separation of galaxies i and j. These methods of determining R_G all assume that the mass distribution in the cluster is traced by the light.

A promising new optical method of determining cluster masses is through the study of the gravitationally lensed arcs and arclets mentioned above. The full mathematical treatment of the subject is complex and the equation given below is for the simple (and ideal) case of a giant arc caused by a small perturbation to the perfect Einstein ring geometry. Then the critical surface density for lensing is given by

$$\Sigma_{cr} = \frac{M(< r)}{\pi r^2} = \frac{c^2}{4\pi G} \frac{D_{OS}}{D_{OL} D_{LS}} \qquad (5.13)$$

$D_{OS,OL,LS}$ are the angular diameter distances between observer, source and lens. The situation is complicated by non-spherical lenses and by the intrinsic shape of the lensed objects.

Soucail (1992) summarises attempts to derive the masses of A370 and A2390 by the study of giant luminous arcs. A multiplicity of models exist for A370; assuming that the arc is seen at the Einstein radius then the models are in general agreement that the mass inside the arc $\sim 1-2 \times 10^{14} M\odot$. A smoothly distributed dark matter component is required. The arc in A2390 appears to show evidence for a dark matter distribution which does not follow the light distribution. Hammer (1991) concludes that most of the lensing clusters he has studied should be more compact than inferred from their optical and X–ray profiles.

Tyson *et al.* (1990) have studied the statistical properties of smaller arclets; gravitationally lensed background galaxies. At a limiting surface brightness of 29 B magnitudes per square arcsecond there are $\sim 20 - 30$ such galaxies within the central square arcminute of the foreground cluster. Each background galaxy above some redshift, $z \sim 0.8$, will produce an arclet. The statistical study of the properties of the arclets can be used to determine the mass distribution.

X–ray mass determination

Assuming that the cluster is spherical and that the gas is in hydrostatic equilibrium, then

$$\frac{dP_{gas}}{dr} = -\rho_{gas}\frac{d\phi}{dr} = \rho_{gas}\frac{GM(< r)}{r^2} \tag{5.14}$$

Substituting $\mu m P_{gas} = \rho_{gas} kT$

$$kT\frac{d\rho_{gas}}{dr} + k\rho_{gas}\frac{dT}{dr} = -\rho_{gas}\mu m\frac{GM(< r)}{r^2} \tag{5.15}$$

from which

$$M(< r) = \frac{-kT}{\mu mG}\left(\frac{d\log\rho_{gas}}{d\log r} + \frac{d\log T}{d\log r}\right) \tag{5.16}$$

If the radial density and temperature profiles are both known then M can be calculated. The biggest uncertainty is caused by a lack of knowledge of $T(r)$. The next generation of X–ray satellites will provide the spatially resolved spectra required to improve estimates of the total mass.

5.3.2 Mass distribution and the mass content of clusters

Optical

The galaxy distribution in clusters has been studied by, among others, Beers & Tonry (1986) and Colless (1987). A number of models have been fit to the data. None of the bounded or unbounded isothermal models can be expressed in terms of simple analytic functions. The most popular model in use is that of King (1962) who showed that a reasonable approximation to the inner parts of an isothermal distribution was given by

$$\sigma(b) = \left(1 + \left(\frac{b}{a}\right)^2\right)^{-1} \tag{5.17}$$

where $\sigma(b)$ is the projected number density of galaxies. The space density of galaxies is

$$n(r) = n_0 \left(1 + \left(\frac{r}{a}\right)^2\right)^{-3/2} \tag{5.18}$$

and $\sigma_0 = 2n_0 a$. At $r \gg a$ the cluster mass and galaxy numbers diverge as $\ln(r/a)$ so the analytic King model must be truncated at some finite radius.

Another analytic model is that of de Vaucouleurs (1948) which was originally formulated to fit the surface brightness profiles of elliptical galaxies. The projected galaxy density is

$$\sigma(b) = \sigma_0 \exp\left[-7.67\left(\frac{b}{r_e}\right)^{1/4}\right] \tag{5.19}$$

r_e is an 'effective radius' which contains half the projected galaxies. The de Vaucouleurs form converges to a finite cluster mass and number density of galaxies; however, it has not been widely used for cluster work.

Gas

The gas distribution may also be parameterised using the King and de Vaucouleurs models although, again, the former has been more frequently used. The

King model in the formalism of Cavaliere & Fusco-Fermiano (1976) is given by

$$S(r) = S_0 \left(1 + \left(\frac{r}{a}\right)^2\right)^{1/2-3\beta}$$
(5.20)

If the gas is isothermal then the gas density profile is

$$\rho_{gas} = \rho_0 \left(1 + \left(\frac{r}{a}\right)^2\right)^{-3\beta/2}$$
(5.21)

ρ_{gas} and n_{gal} are then linked by

$$\rho_{gas} = n_{gal}^{\beta}$$
(5.22)

β is the ratio of the gas temperature to the galaxy "temperature". For isotropic orbits

$$\beta = \frac{\mu m_p \sigma_r^2}{kT}$$
(5.23)

The gas masses inferred by integrating Equation 5.21 are typically a few times $10^{14} M_\odot$ within a few Mpc of the cluster centre, comprising 10–30 % of the virial mass of the cluster. David *et al.* (1990a) find that the ratio of gas mass to stellar mass in clusters increases with the cluster temperature (or equivalently cluster mass). Figure 5.2 shows their results. Edge (1989) (see also Edge & Stewart 1991a) violently disagrees with this result and claims that it is not seen in the *EXOSAT* data. David *et al.* evaluate gas masses within 5 core radii while Edge calculates the gas mass within a fixed metric radius of 0.5 Mpc for all clusters. Edge claims that the discrepancy is inevitable since more massive clusters have larger core radii so that David *et al.* integrate to a larger metric radius for rich clusters.

David *et al.* interpret their results as a decreased efficiency of galaxy formation in rich clusters and postulate that the galaxy formation process is disrupted by the sub-cluster mergers which form rich clusters. The possibility that much of the gas from poor clusters has evaporated away cannot be ruled out by the data. An alternative explanation would be that some of the galactic content in rich clusters has been missed. Early results from the study of very low surface brightness galaxies (J. Davies, priv. comm.) suggest that these galaxies *may* be preferentially found in rich cluster environments.
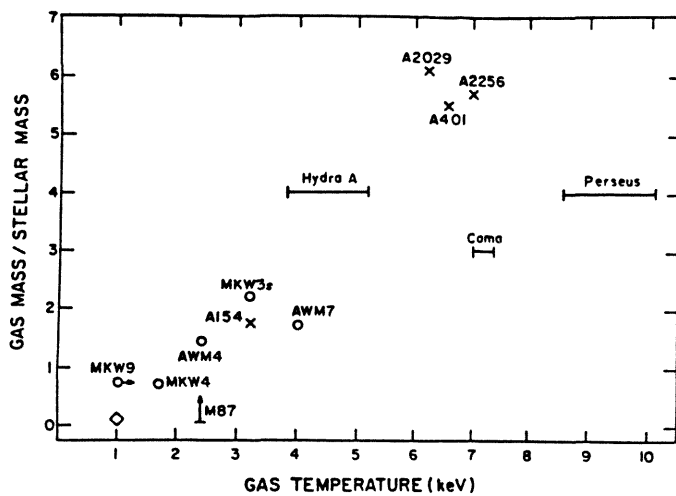
Figure 5.2: Gas mass of clusters (calculated within 5 core radii) plotted against cluster temperature. Taken from David *et al.* 1990a.

Dark Matter

Mass estimates using the virial theorem may be significantly in error if the assumption that mass follows light is wrong (see Fitchett (1990) for a review). Merritt (1987) showed that the maximum cluster mass (for an uniform distribution of dark matter) is $\sim$ 80 times larger than the mass determined by the standard virial theorem. Knowledge of the dark matter distribution is therefore an important prerequisite to the study of cluster masses and hence of the initial density fluctuations from whence clusters came. Merritt (1987) attempted to derive the dark matter distribution of the Coma cluster by analysing the velocity dispersion profile of the cluster. He found that the data were consistent with a wide range of models for the dark matter distribution, with almost an order of magnitude range in the total cluster mass.

Hughes (1989) utilises the accurately determined profile $\rho_{gas}(r)$ together with temperature measurements at various effective radii to constrain the dark matter

distribution in Coma. Models of the form

$$\rho_{dm}(r) = \rho_0 \left(1 + \left(\frac{r}{r_c}\right)^2\right)$$ (5.24)

with $r_c > 25.5'$ are excluded by the X-ray data. Fitchett (1990) comments that X-ray images show the gravitational potential of the cluster to be generally much smoother than the galaxy distribution.

5.3.3 The ICM

Radiative processes

X-ray continuum emission from an hot, diffuse plasma is due to three main processes:

- thermal bremsstrahlung (free-free) emission

- recombination

- two photon decay

At the temperatures of the isothermal regions of most clusters, for roughly solar abundance material, thermal bremsstrahlung from hydrogen and helium dominates the continuum. Processes contributing to line emission include: collisional excitation, radiative recombination and inner shell collisional excitation. X-ray emissivities for both lines and continua have been compiled by Raymond & Smith (1977, 1979 & priv. comm.), Mewe *et al.* (1985, 1986)) and Masai (1984). The strongest line observed in clusters is a blend of iron $K\alpha$ lines, predominantly from Fe^{24+} and Fe^{25+} at ~ 6.7 keV. The shape of the X-ray spectrum thus depends on the elemental abundances and on the temperature while the normalisation depends on the emission integral

$$EI = \int n_p n_e dV$$ (5.25)

103

Cooling flows

If the ICM is in hydrostatic equilibrium (this assumption is valid out to radii of a few Mpc) and there is no source of heating then the X-ray emission causes the gas to gradually cool and lose energy. Following Sarazin (1988) a cooling time may be defined

$$t_{cool} \equiv \left(\frac{d \ln T_g}{dt} \right)^{-1} \tag{5.26}$$

This is then given by

$$t_{cool} = 8.5 \times 10^{10} \text{yr} \left(\frac{\rho_g}{10^{-3} \text{cm}^{-3}} \right)^{-1} \left(\frac{T_g}{10^8 \text{K}} \right)^{1/2} \tag{5.27}$$

For the outer regions of most clusters this is longer than the Hubble time and cooling is not important. Towards the centre of clusters where the gas density is higher the cooling time is less than the age of the cluster. Cooling gas at the centre causes an excess pressure gradient, leading to inward flow of gas. The cooling flow phenomenon is extensively reviewed in Fabian, Nulsen & Canizares (1991).

The fate of the cooled gas has long been a mystery. X-ray data show that the cooled gas is deposited in a spatially distributed manner rather than all at the centre of the cluster. Optical measurements preclude the gas forming stars with a normal Salpetre IMF - any star formation must consist almost solely of low mass stars. Many authors find the disposal of such a large quantity of material (a fairly moderate mass flow rate of $100 M_\odot \text{yr}^{-1}$ will deposit $2 \times 10^{12} M_\odot$ over an Hubble time) to be an untenable proposition. Cooling flows have thus provoked much controversy and a number of authors have suggested that mass flow rates have been overestimated, usually invoking some heat source to balance the cooling (see *e.g* Fabian, Nulsen and Canizares (1991) and references therein). The spectroscopic data of Canizares *et al.* (1979) can be used to refute most of these models although Bregman (1992) claims that it cannot completely rule out his 'warming flow model'. The discovery of a large amount of cold, absorbing material in cooling flow clusters (White *et al.* 1991) may provide an answer to this ongoing problem.

The origin of the ICM

Much of the gas in clusters must have been processed in stars. Possible origins of this enriched material are:

o Population III stars (Carr *et al.* 1984)

This theory is usually mentioned for historical reasons. Here it is simply noted that no stars are known which do not exist in galaxies and this theory is not discussed further.

o Supernovae driven winds

De Young (1978) first proposed that the supernovae resulting from massive, short lived stars could expel gas from elliptical galaxies in a wind.

o Ram pressure stripping

Gunn & Gott (1972) suggested that some of the ICM could come from pressure stripping of the ISM of galaxies. This requires that much of the ICM be primordial to initiate the stripping process.

These latter two models are discussed in much greater detail in Chapter 7 in the context of their specific predictions for iron abundances in the ICM.

5.3.4 Cosmology and cluster evolution

Clusters of galaxies are largest gravitationally bound structures in the universe. Larger systems, such as superclusters, have not yet virialised and may still be expanding with the universe, although at a reduced rate (Rees 1992). Rich clusters are therefore very special regions of space, probably arising from 3σ density fluctuations.

As previously mentioned, substantial negative luminosity evolution is seen in the X–ray band. This evolution may be explained in terms of simple hierarchical

merging of subclusters to form rich clusters, as predicted by CDM models. *EIN-STEIN* and *ROSAT* images provide evidence to support this view; nearly all of the clusters appear to be elliptical and many reveal clear sub-clumps of X–ray emission. Between mergers clusters evolve towards a more symmetrical state through violent relaxation (Lynden-Bell 1967).

No such luminosity evolution has been found in the optical band. Indeed there have been suggestions that gravitational lensing has shown that too many massive clusters exist at large redshifts for standard CDM.

Another confrontation between clusters and cosmology is in the baryon content of clusters. Standard nucleosynthesis arguments (Olive *et al.* 1990) predict

$$\Omega_b \sim 0.016h^{-2} \qquad (5.28)$$

The gas content of some clusters appears to be as large as 30–40% of the virial mass, implying either some process of baryon segregation on the scale of clusters or $\Omega \neq 1$, in which case the baryonic fraction in clusters equals Ω_b/Ω_0. White (1992) cites this as a strong piece of evidence for an open universe. Cosmological models do exist which retain all the benefits of inflation but allow $\Omega < 1$ (Madsen & Ellis 1988, Ellis *et al.* 1991, Madsen *et al.* 1992).

The use of the Sunyaev Zel'dovich effect to determine H_0 has already been discussed in this chapter. The brightest galaxy in a cluster is often used as a standard candle in attempts to determine H_0 and q_o. Edge (1991) has shown that the properties of brightest cluster galaxies are a strong function of their X–ray environment and so should be used with care.

Chapter 6

Ginga Observations of Clusters

Overview

This chapter describes the analysis of 38 pointed observations of clusters made by *Ginga*. The results of simple, isothermal fits to the spectra of the *Ginga* cluster sample are presented. Cluster spectra are found to be, in general, non-isothermal. Individual clusters are then discussed in more detail and more complex spectral models are considered.

6.1 The *Ginga* cluster sample

Ginga observed 46 clusters in pointing mode during its lifetime (scanning observations are not considered here). These clusters do not form a statistically complete sample but nor have they been selected with a single bias. Instead they have been selected to cover a wide range of cluster properties: richness, optical morphology, mass flow rate *etc.*. Thus it is hoped that they may be, in some sense, a 'representative' sample. This sample is an extension of the sample of rich clusters presented by Hatsukade (1989) and the sample of poor groups included

in Tsuru (1991).

6.1.1 Observations

Table 6.1 gives the observing log of the observations and details the background subtraction method used. 'L' indicates that a Local background model was produced using a contemporaneous blank-sky observation. An entry of the form '89A' indicates that a Universal background model was used.

For a period of 7 months between June 1990 and January 1991 LAC detectors 5 and 6 suffered from spasmodic noise, and in some cases these detectors were switched off. All the cluster observations reported here use all 8 of the LAC detectors and careful inspection of the data revealed no excess noise in the suspect channels. However many of the background observations were taken with only 6 detectors. In order for Universal background models to be applied to data where no satisactory local background observation exists, it was necessary to ignore channels 5 and 6 in the analysis. These clusters are marked with an asterix in Table 6.1 and the quoted count rates are only from detectors 1,2,3,4,7 and 8. To first order the total count rates will be 4/3 times the values quoted in the table.

Pulse height spectra were extracted in the standard way described in Chapter 1 and were fit to trial models using standard χ^2 minimisation techniques. Unless stated otherwise in the text, all the results described below are from fitting models to the pulse height spectra between PHA channels 4-30 (2-18 keV). All iron abundances quoted are relative to a cosmic value, $[Fe]/[H] = 4 \times 10^{-5}$.

6.1.2 Isothermal Spectral Fits

All the cluster spectra were fit to the isothermal, optically thin plasma models of Raymond & Smith (1977, 1979 & priv. comm.). Fits were performed both with the absorbing column fixed at the galactic value (Stark et al. 1988) and with the

Cluster	Redshift	RA (1950)	DEC (1950)	Observation date	Mean Offset (arcmin)	Exposure (s)	Bgd model	2-10 keV LAC count rate ct s^{-1}
Cl 0016+16	0.54	4.0	16.15	2/8/88	24	16600	88B	< 0.5
A33	0.28	6.15	-19.78	9/12/88	14.5	13450	88C	2.01 ± 0.07
A193	0.0482	20.62	8.44	8/9/91	29	13950	L	3.22 ± 0.06
A262*	0.0164	27.44	35.9	17/8/90	6	17660	90B	10.52 ± 0.05
AWM7	0.0179	42.80	41.36	8/2/91	39	580	L	27.25 ± 0.42
Perseus	0.0183	49.12	41.33	17/1/89	7	1600	89A	392.0 ± 0.5
A478	0.090	62.67	10.35	7/2/89	11	18300	89A	29.8 ± 0.07
A483	0.280	63.42	-11.65	8/2/89	2.4	20000	89A	1.92 ± 0.003
A496	0.0320	67.83	-13.36	15/10/88	18	17850	88C	28.95 ± 0.005
A520	0.203	72.89	2.84	26/2/91	6	19300	91B	2.95 ± 0.05
A644	0.0781	123.75	-7.36	21/4/88	6.6	24450	88B	20.45 ± 0.003
A665	0.182	126.55	66.06	10/11/88	17	26624	88C	3.45 ± 0.26
A754*	0.0528	136.73	-9.49	17/11/90	4	12900	90C	29.25 ± 0.07
Hydra A	0.0522	138.92	-11.88	9/12/89	22	14200	89C	11.5 ± 0.07
A963	0.206	153.55	39.28	12/12/89	20	11400	89C	2.13 ± 0.07
A1060	0.0114	158.59	-27.27	20/12/87	13	29500	87C	24.22 ± 0.05
A1120		162.62	31.07	3/5/94	25	33000	L	< 0.6
A1367	0.0215	175.53	20.03	13/12/89	28	13200	89C	13.50 ± 0.07
A1413	0.1427	175.18	23.67	7/5/88	9	24700	88B	8.01 ± 0.004
MKW4	0.0196	180.48	2.18	30/5/91	12	16800	91D	2.12 ± 0.05
Virgo	0.0038	187.07	12.67	29/6/87	12	4608	87B2	143.1 ± 0.2
Centaurus	0.0109	191.50	-41.30	14/7/89	13	15300	89B	62.67 ± 0.1
Coma	0.0232	194.22	28.22	1/7/87	9	4608	87B2	138.3 ± 0.17
A1651	0.0825	194.25	-3.92	20/6/91	13	13200	L	10.4 ± 0.07
A1689	0.181	197.25	-1.1	3/7/89	13	18700	89B	7.95 ± 0.003
A1795	0.0616	206.64	26.84	23/6/88	10.8	14600	88B	26.18 ± 0.006
A2009	0.153	224.5	21.57	29/6/89	9	19200	L	6.54 ± 0.05
MKW3S	0.0434	229.86	7.89	15/3/89	6	15500	89A	11.51 ± 0.005
A2142	0.0899	239.07	27.38	10/8/88	10	16640	88B	33.36 ± 0.004
AWM4	0.0313	240.70	24.07	23/3/91	7	17900	L	1.98 ± 0.08
A2163	0.1698	243.23	-6.0	19/8/89	6	14300	89B	11.56 ± 0.07
A2199	0.0309	246.73	39.66	9/3/90	14.4	22900	L	30.25 ± 0.004
A2218	0.171	248.9	66.31	12/11/87	10	10000	L	3.2 ± 0.1
A2256	0.0307	256.69	78.71	27/4/87		2800	L	22.05 ± 0.18
A2319	0.0564	289.91	43.84	23/5/90	10.8	17500	L	61.68 ± 0.006
S2246-647	0.2	341.5	-64.7	16/6/89	6.3	19500	89B	5.56 ± 0.06
A2507	0.196	343.56	5.23	8/11/88	25	18900	88C	3.3 ± 0.05
A2634	0.0322	354.0	26.79	8/8/89	8.4	20600	89B	7.26 ± 0.003

Table 6.1: Observation log for the *Ginga* cluster sample.

column as a free parameter. The iron abundance was a free parameter in the fit; the abundances of all other heavy elements floated in unison, however they were poorly constrained.

The results of isothermal fits with the absorbing column fixed at the galactic value are given in Table 6.2. The fluxes in this table are not corrected for the effects of galactic absorption or for the collimator response. As expected, the constraints on absorption were poor. For most of the clusters, the addition of the absorbing column as a free parameter did not result in a significant improvement in the fit. Table 6.3 show the results of allowing the absorption to float for those clusters for which an F-test shows that the fit is improved at > 90% confidence.

In some of the cases (e.g. A2163) the extra absorption is not formally required; in some cases (e.g. A1060) the fit is still not acceptable even with a free absorbing column, so the estimated column is not necessarily meaningful and in other cases (e.g. A496) the measured column is lower than the galactic column and probably reflects a soft component in the spectrum due to a cooling flow.

Many of the cluster spectra were not well fit by an isothermal model (90% confidence limit: $\chi^2_\nu = 1.39$ for 23 degrees of freedom). In these cases more complicated models were fitted to the *Ginga* spectrum: these included models with two isothermal components, models with an isothermal plus a power law component to represent a possible AGN in the cluster, and models containing a power law distribution of emission measures to mimic a cooling flow spectrum (Mushotzky & Szymkowiak 1988). It is also important to note that, of the clusters whose *Ginga* spectra *were* acceptably isothermal, Coma is known to have a non-isothermal spectrum by comparison with previous satellite results (see below), while *ROSAT* observations of A2199, A2142 and A2256 have shown that these clusters also deviate significantly from isothermality. Departures from isothermality in clusters should thus be considered normal.

110

Cluster	kT (keV)	Iron Abundance (solar units)	Galactic Column ($\times 10^{21}$ cm^{-2})	2-10 keV flux ($\times 10^{-11}$ ergs s^{-1} cm-2)	χ^2/d.o.f
A33	$9.76^{+2.8}_{-2.8}$	< 0.57	0.19	0.43	24.9/23
A193	$3.02^{+0.39}_{-0.32}$	$0.29^{+0.29}_{-0.23}$	0.44	6.2	14.1/23
A262	$2.22^{+0.09}_{-0.06}$	$0.49^{+0.10}_{-0.10}$	0.52	2.6	54.0/23
AWM7	$3.37^{+0.37}_{-0.33}$	$0.28^{+0.2}_{-0.15}$	0.88	5.36	16.1/23
Perseus	$5.72^{+0.07}_{-0.07}$	$0.29^{+0.03}_{-0.03}$	1.37	82.5	57.9/23
A478	$6.72^{+0.16}_{-0.15}$	$0.30^{+0.03}_{-0.04}$	1.50	6.31	44.9/23
A483	$8.40^{+2.0}_{-1.6}$	$0.15^{+0.28}_{-0.15}$	0.38	0.41	12.9/23
A496	$4.03^{+0.09}_{-0.09}$	$0.30^{+0.03}_{-0.04}$	0.43	5.8	33.2/23
A520	$8.68^{+1.4}_{-1.1}$	$0.20^{+0.20}_{-0.36}$	0.75	0.64	12.32/23
A644	$6.50^{+0.17}_{-0.18}$	$0.26^{+0.04}_{-0.04}$	0.77	4.3	12.4/23
A665	$6.25^{+0.69}_{-0.60}$	$0.28^{+0.16}_{-0.14}$	0.42	0.72	19.2/23
A754	$9.31^{+0.30}_{-0.27}$	$0.19^{+0.05}_{-0.05}$	0.46	8.6	25.6/23
Hydra A	$3.58^{+0.17}_{-0.17}$	$0.30^{+0.23}_{-0.39}$	0.48	2.3	41.1/23
A963	$6.08^{+1.6}_{-1.4}$	$0.10^{+0.43}_{-0.1}$	0.14	0.44	31.9/23
A1060	$3.19^{+0.07}_{-0.07}$	$0.27^{+0.03}_{-0.03}$	0.5	4.7	103.5/23
A1367	$3.46^{+0.13}_{-0.13}$	$0.20^{+0.05}_{-0.06}$	0.22	2.7	24.1/23
A1413	$8.94^{+0.76}_{-0.65}$	$0.26^{+0.11}_{-0.11}$	0.2	1.7	14.1/23
MKW4	$1.46^{+0.14}_{-0.15}$	$0.77^{+1.8}_{-0.77}$	0.19	0.36	21.8/23
Virgo	$2.76^{+0.05}_{-0.03}$	$0.25^{+0.03}_{-0.03}$	0.25	27.0	332.5/23
Centaurus	$3.42^{+0.07}_{-0.05}$	$0.33^{+0.03}_{-0.03}$	0.8	12.4	42.3/23
Coma	$8.08^{+0.12}_{-0.13}$	$0.17^{+0.03}_{-0.025}$	0.1	30.0	11.9/23
A1651	$5.87^{+0.35}_{-0.33}$	$0.25^{+0.1}_{-0.09}$	0.17	2.2	17.5/23
A1689	$9.73^{+0.67}_{-0.74}$	$0.24^{+0.11}_{-0.11}$	0.18	1.7	18.2/23
A1795	$5.60^{+0.14}_{-0.15}$	$0.23^{+0.04}_{-0.04}$	0.11	5.45	46.6/23
A2009	$6.20^{+0.45}_{-0.40}$	$0.27^{+0.10}_{-0.08}$	0.32	1.40	26.6/23
MKW3S	$2.79^{+0.06}_{-0.05}$	$0.41^{+0.03}_{-0.04}$	0.3	2.21	18.0/23
A2142	$8.41^{+0.20}_{-0.21}$	$0.21^{+0.04}_{-0.03}$	0.38	7.2	11.3/23
AWM4	$2.65^{+0.44}_{-0.34}$	$0.37^{+0.41}_{-0.33}$	0.49	0.42	14.6/13
A2163	$13.0^{+1.1}_{-0.9}$	$0.19^{+0.13}_{-0.12}$	1.1	2.6	15.9/23
A2199	$4.08^{+0.08}_{-0.08}$	$0.26^{+0.02}_{-0.03}$	0.09	6.1	17.9/23
A2218	$6.05^{+1.65}_{-1.23}$	$0.07^{+0.30}_{-0.07}$	0.3	0.66	11.45/23
A2256	$7.11^{+0.66}_{-0.50}$	$0.23^{+0.11}_{-0.10}$	0.37	4.7	17.3/23
A2319	$8.95^{+0.06}_{-0.15}$	$0.19^{+0.03}_{-0.03}$	0.84	1.3	17.2/23
A2507	$9.89^{+1.2}_{-1.6}$	< 0.33	0.55	0.72	34.8/23
S2246-647	$5.83^{+0.36}_{-0.33}$	$0.26^{+0.20}_{-0.16}$	0.5	1.3	25.1/23
A2634	$3.16^{+0.17}_{-0.16}$	$0.29^{+0.09}_{-0.08}$	0.49	1.42	36.0/23

Table 6.2: Results of isothermal RS fits to the cluster spectra

Cluster	kT	Iron Abundance	Measured Column $(\times 10^{21}\,\mathrm{cm}^2)$	χ^2/ν
A478	$6.32^{+0.24}_{-0.23}$	$0.27^{+0.04}_{-0.04}$	$4.2^{+1.2}_{-1.2}$	20.6/22
A496	$4.07^{+0.09}_{-0.07}$	$0.30^{+0.04}_{-0.04}$	< 0.29	27.4/22
A520	$7.43^{+1.9}_{-1.4}$	$0.17^{+0.42}_{-0.17}$	$5.5^{+6.6}_{-5.5}$	9.3/22
A2319	$9.07^{+0.22}_{-0.24}$	$0.20^{+0.04}_{-0.04}$	$0.21^{+0.86}_{-0.21}$	14.6/22
A2163	$12.0^{+1.3}_{-1.2}$	$0.13^{+0.14}_{-0.13}$	$3.3^{+2.0}_{-2.0}$	10.4/22
Centaurus	$3.48^{+0.06}_{-0.07}$	$0.32^{+0.03}_{-0.03}$	< 0.27	30.7/22

Table 6.3: The results of isothermal fits with the absorbing column included as a free parameter for those clusters where this improves the fit at greater than 90% confidence.

6.2 Individual clusters

6.2.1 A33

Arnaud *et al.* (1991b) report the non-detection of this cluster with *Ginga*. From pointing data they obtain a limit $I_x < 0.7\,\mathrm{ct\,s}^{-1}$, significantly lower than that reported here. Whilst the temperature reported in Table 6.2 is what would be expected from the HEAO-1 luminosity (Kowalski *et al.* 1984), a power-law model is an equally good fit to the data and the derived spectral index is $\Gamma = 1.94^{+0.08}_{-0.08}$. When a Local background model is applied to the data the 2–10 keV count rate is $0.73\,\mathrm{ct\,s}^{-1}$. The identification of A33 with the HEAO-1 source thus remains uncertain.

6.2.2 A262

Mushotzky (1992) reports BBXRT observations of A262. The full BBXRT data require an additional component of cool ($kT < 1$ keV) gas in the centre of the cluster. The 2–18 keV *Ginga* spectrum is well fit by a two component thermal model with $kT_{\mathrm{low}} = 1.14^{+0.88}_{-0.51}$ and $kT_{\mathrm{high}} = 3.13^{+17.57}_{-0.41}$. Unfortunately, kT_{high}

is only very poorly constrained. The iron abundances were tied to the same (floating) value and the best fit value was $0.31^{+0.13}_{-0.12}$. If intrinsic absorption is applied to the cool component (this was required by the BBXRT data) there is a slight reduction in χ^2 and the upper limit on T_{high} is reduced but the improvment in the fit is not statistically significant.

The A262 results are a good illustration of the effect of choosing an appropriate confidence interval. If the 1σ error for 1 parameter of interest is calculated ($\Delta\chi^2 = 1$) then the confidence region for the high temperature component is $kT = 3.12^{+0.23}_{-0.18}$. If the 1σ error for 2 parameters of interest is calculated ($\Delta\chi^2 = 2.3$) then the limits are $kT = 3.12^{+4.2}_{-0.27}$.

6.2.3 Perseus

Ginga observations of the Perseus cluster have been reported by Allen *et al.* (1992) who claim that the X–ray spectrum is well fit by an isothermal model with an additional cooling flow component (Johnstone *et al.* 1992); they find no evidence of non-thermal emission from NGC 1275. However, in order to obtain this result, it was necessary to use a cluster redshift of $z = 0.0153$ rather than the value of $z = 0.0182$ determined optically. This corresponds to an energy shift $\Delta E \sim 20$ eV which Allen *et al.* attribute to instrumental effects (they do not attempt to verify this gain shift through the in-flight monitoring of the silver line). The Perseus cluster is sufficiently bright that the Mid layer data ought to yield extra information to constrain any possible non-thermal component which would be contributing at harder energies (Allen *et al.* use only Top layer data). Here models are tested on both the Top and the summed (Top+Mid) data. Figure 6.1 shows the Top layer data fit to the isothermal model described in Table 6.2. The residuals show an excess at both high and low energies.

Models with an isothermal and a non-thermal component are listed in Table 6.2.3. They did not provide an acceptable fit to the Top layer data alone although the fit to the summed data was formally acceptable. Figure 6.2 shows the incident

113
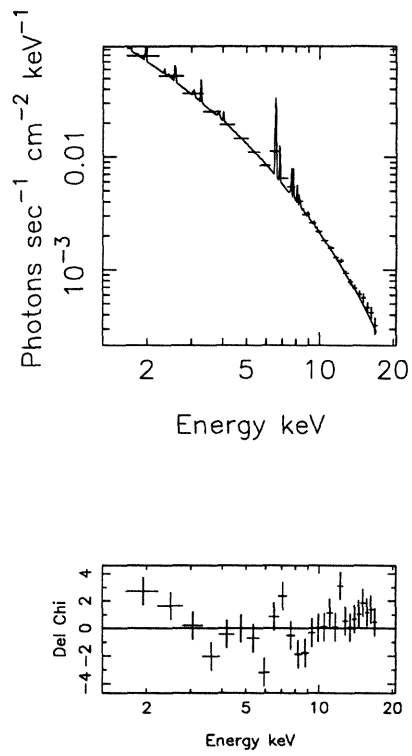
Figure 6.1: The Top layer spectrum of the Perseus cluster fitted to an isothermal model.
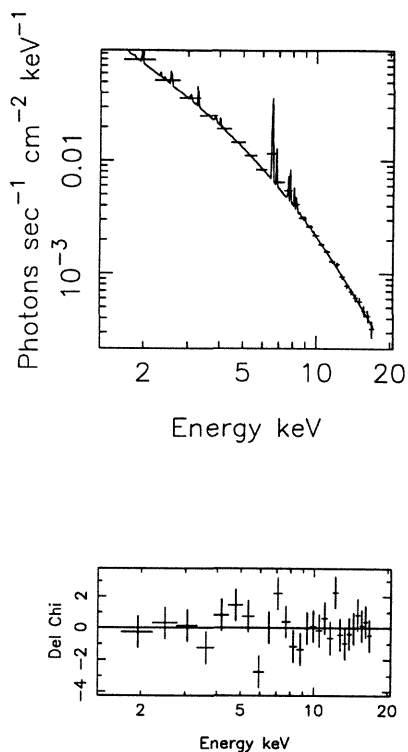
Figure 6.2: The Top layer spectrum of the Perseus cluster fitted to a model consisting of an isothermal component and a power-law component.

spectrum and residuals for this model fitted to the Top layer data alone. It can be seen that the fit is acceptable at hard energies and the badness of fit is caused by residuals around 6 keV.

The best cooling flow model consisted of (isothermal+PLEM) components with T_{high} and T_{iso} floating in unison. The best fitting model on the summed data was statistically acceptable ($\chi^2_\nu = 1.11$) and gave an isothermal temperature of $kT_{iso} = 7.3^{+0.6}_{-1.1}$ keV. The distribution index was then $6.9^{+0.2}_{-0.2}$ and the absorbing column was fixed at the galactic column. This temperature is significantly higher than the value $kT = 6.33^{+0.21}_{-0.18}$ keV of Allen et $al.$ (1992), again suggesting that hard X-ray emission from NGC1275 is present. If the distribution index is fixed at 5 then the isothermal temperature becomes $kT_{iso} = 6.6$ keV and the fit is just

Dataset used	kT (keV)	Γ	N_H (intrinsic)	Iron abundance	χ^2_{min} /d.o.f
Top	$5.59^{+0.5}_{-0.47}$	$2.26^{+0.90}_{-0.63}$	0 (fixed)	$0.36^{+0.06}_{-0.06}$	29.1/21
Summed	$5.43^{+0.49}_{-0.35}$	$2.16^{+0.67}_{-0.62}$	0 (fixed)	$0.36^{+0.06}_{-0.06}$	26.8/21
Summed	$6.17^{+0.44}_{-1.05}$	$3.01^{+2.2}_{-1.6}$	$16.0^{+33.5}_{-16.0}$	$041^{+0.13}_{-0.10}$	24.6/20

Table 6.4: Results of (thermal+non-thermal) fits to the *Ginga* spectrum of the Perseus cluster.

acceptable ($\chi^2_\nu = 1.27$).

6.2.4   A478

This is the only cluster where significant excess absorption is observed. *Ginga* observations of A478 have been reported by Johnstone *et al.* 1992. The best estimate of the Galactic column density is $N_H \sim 2.0 \times 10^{21}$ cm^{-2} (Heiles priv.comm. reported in Johnstone *et al.*) but the existence of a reflection nebula within 20 arcmin of the cluster centre may provide additional absorbing material on small angular scales. As the isothermal model with extra absorption provided a good fit to the spectrum, more complicated models have not been considered here. Johnstone *et al.* use the *Ginga* data in conjunction with the *EINSTEIN* SSS data to constrain a cooling flow model and obtain $M \sim 1000 M_\odot \, \mathrm{yr}^{-1}$ and an absorbing column of $N_H \sim 4.8 \times 10^{21}$ cm^{-2}.

6.2.5   A483

The count rate for this object is slightly lower than that obtained by Arnaud *et al.* (1991b). Here a Universal background model was applied while Arnaud *et al.* preferred a Local model. However the spectral parameters derived here are in complete agreement with those obtained by Arnaud *et al.*
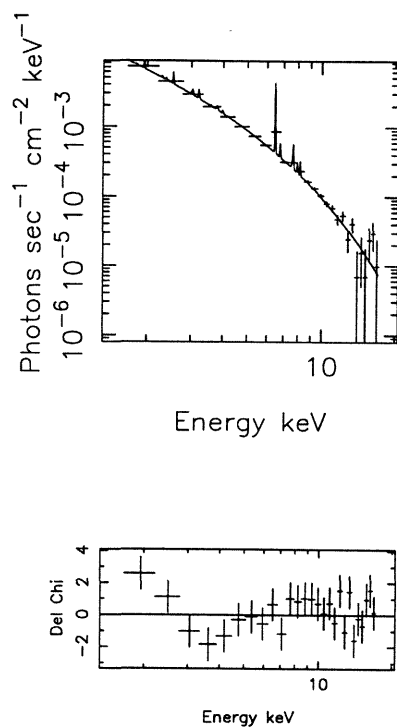
Figure 6.3: The *Ginga* spectrum of A496 fitted to an isothermal model. Excess emission at low energies is clearly seen.

6.2.6 A496

An isothermal model provided a bad fit to the *Ginga* spectrum of this known cooling flow cluster. Figure 6.3 shows the incident spectrum and residuals for the isothermal model; the model fits badly at low energies, in qualitative contrast to the results obtained for A1060 (see below) where a hard tail is apparent in the residuals. An acceptable fit ($\chi^2_\nu = 0.80$) is provided by a PLEM model with the following parameters; $T_{\text{high}} = 4.34$, $T_{\text{iso}} = 4.3^{+1.2}_{-0.06}$, distribution index= $4.2^{+2.6}_{-4.2}$ and galactic absorption. The iron abundance in the cooling flow component was fixed at 0.3 and the iron abundance of the isothermal component was $0.29^{+0.07}_{-0.04}$. The mass flow rate deduced from the normalisation of the PLEM component is $81 M_\odot \text{yr}^{-1}$.

6.2.7 Hydra A

The Hydra-A cluster is known to have a massive cooling flow with $\dot{M} \sim 400\ M_{\odot}\ \mathrm{yr}^{-1}$ (David *et al.* 1990a). An isothermal model was a poor fit to the *Ginga* spectrum and inspection of the residuals revealed excesses as high and low energies. It was not possible to find an acceptable, meaningful fit using a model with two thermal components as the second component was very hard ($kT > 20$ keV). Similarly, attempts to find a solution using a PLEM model also failed. Thus an attempt was made to fit the hard emission using a non-thermal component.

The 10–18 keV spectrum (where X–ray emission from a putative AGN would dominate over the cluster emission) was well fit by a power-law model with $\Gamma = 2.2^{+0.8}_{-0.8}$, *ie.* the slope was poorly constrained but consistent with the value expected from an AGN. Fixing the power-law slope at this value gave values for the cluster temperature and iron abundance of $kT = 3.13^{+0.33}_{-0.32}$ and $0.40^{+0.19}_{-0.12}$ respectively. The inferred luminosity of a power-law source at the redshift of the cluster is $L = 1.3 \times 10^{44}\ \mathrm{erg\,s}^{-1}$. The hard emission may be associated with the Hydra A radio source (see discussion on X–ray emission from Cygnus A and A2634 below).

6.2.8 A1060

HEAO-1 observations of A1060 (the Hydra I cluster) showed that the cluster was strongly non-isothermal (Mitchell & Mushotzky 1980). These authors found that the X–ray spectrum could be adequately fit by either of two models:

1. A model with two thermal components, $kT_1 \sim 2\mathrm{keV}$, $kT_2 \sim 13\mathrm{keV}$.

2. A model with one thermal and one power-law component (which the authors suggest may be due to inverse Compton emission), $kT \sim 2\mathrm{keV}$, $\Gamma \sim 2.2$.
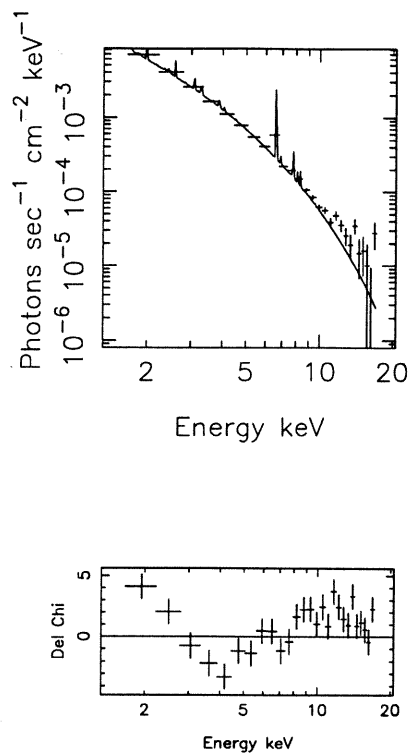
Figure 6.4: Incident photon spectrum and residuals for an isothermal fit to the *Ginga* spectrum of A1060

EXOSAT had insufficient sensitivity to detect any deviation from isothermality (Edge & Stewart 1991a), but Table 6.2 shows that an isothermal fit to the *Ginga* spectrum is not statistically acceptable. Figure 6.4 shows the incident isothermal spectrum and residuals; an excess above 12 keV is clearly visible in the residuals. A1060 is known to have a weak cooling flow of $\dot{M} \sim 18 M_\odot \text{yr}^{-1}$ (Edge, Stewart & Fabian 1992, Singh, Westergaard & Schnopper 1988) which might be expected to cause the low energy spectrum to be non-isothermal.

The *Ginga* spectrum was fit to two-temperature model fits with the iron abundances floating in unison (Table 6.5), thermal + power law models (Table 6.6) and the power-law distribution of emission measures (PLEM) cooling flow model mentioned above (Table 6.7). Since cooling flow models predict a large emission

119

Datasets used	kT_1 (keV)	f_{x_1}	kT_2	f_{x_2}	Iron abundance	χ^2_{min} /d.o.f
$Ginga$(4-30)	$2.61^{+0.15}_{-0.12}$	4.0	> 11	0.76	$0.33^{+0.06}_{-0.05}$	22.0/21
$Ginga$(4-30, 35-42)	$2.61^{+0.15}_{-0.13}$	4.0	> 11	0.75	0.33 ± 0.05	37.0/29
$Ginga$(4-30) + LE	$2.56^{+0.18}_{-1.78}$	3.9	$14.0^{+\infty}_{-4.2}$	0.87	0.34 ± 0.05	37.4/22

Table 6.5: Results of two component thermal fits to the $Ginga$ spectrum of A1060. The iron abundances are tied to the same (floating) value. Unabsorbed fluxes are quoted, in units $10^{-11}\,\mathrm{erg\,s^{-1}\,cm^{-2}}$.

measure at $T < 2$ keV, where the sensitivity of $Ginga$ is poor, the spectral point measured by the $EXOSAT$ LE (Edge 1989) was used in some of the fits.

A two component thermal model provided an acceptable fit to the 2–18 keV $Ginga$ spectrum, but the second thermal component was very poorly constrained. Inspection of Table 6.5 shows that all that may be said about the second thermal component was that it was hard ($kT > 11$keV). Figure 6.5 shows the confidence contours for the temperatures of the two thermal components; the contours are almost vertical, again showing that the hard component is very poorly constrained. In an attempt to better constrain the hard thermal component, data from LAC channels 35–42 were included in the fitting procedure (channels 31–34 inclusive are contaminated by the silver line). Figure 6.6 shows the incident spectum and residuals to a two thermal component model fitted to the $Ginga$ spectrum, including the higher PHA channels; it can be seen that these higher channels add little to the signal but much to the noise. When the LE data is included, the fit becomes worse due to an excess of counts in the LE, above that predicted by the model. The lower bound to the temperature of the thermal component is thus decreased and it appears that a further soft component is necessary.
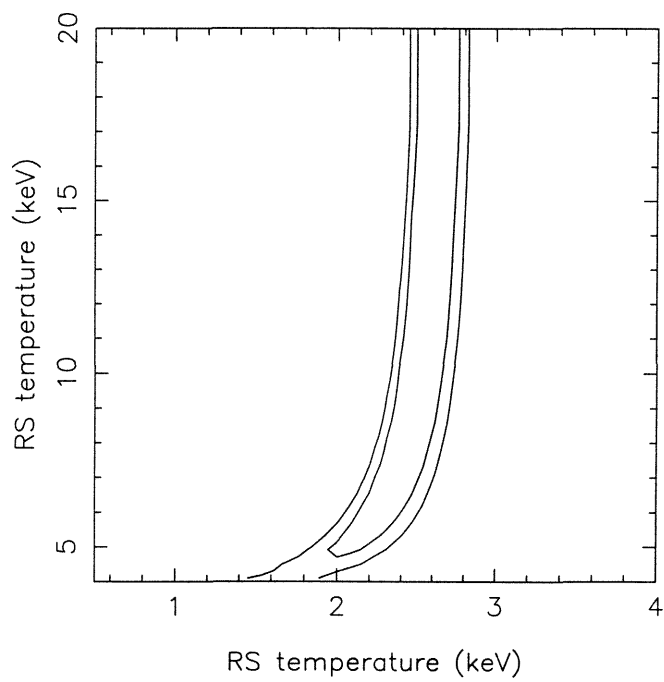
Figure 6.5: Confidence contours for the *Ginga* spectrum of A1060 fit to a two temperature model. The hot component is not really constrained.
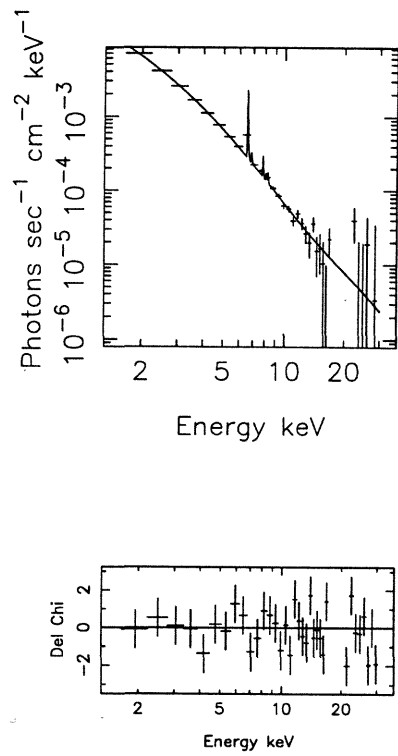
Figure 6.6: Incident photon spectrum and residuals obtained by fitting the *Ginga* spectrum of A1060 (including channels 35-42) to a model with two thermal components.

Datasets used	kT (keV)	f_{x_1}	Γ	f_{x_2}	N_H (intrinsic)	Iron abundance	χ^2_{min} /d.o.f
$Ginga$(4-30)	$2.71^{+0.51}_{-0.15}$	3.7	$2.15^{+0.77}_{-1.38}$	1.1	0 (fixed)	$0.36^{+0.08}_{-0.06}$	20.7/21
$Ginga$(4-30, 35-42)	$2.74^{+0.53}_{-0.17}$	3.6	$2.23^{+0.65}_{-0.10}$	1.1	0 (fixed)	0.37 ± 0.07	35.9/29
$Ginga$(4-30)	$2.65^{+1.2}_{-0.7}$	3.2	$2.5^{+1.7}_{-2.0}$	1.7	$6.4^{+9.3}_{-6.4}$	$0.44^{+0.26}_{-0.15}$	20.4/21
$Ginga$(4-30, 35-42)	$2.67^{+0.90}_{-0.30}$	3.1	$2.6^{+1.4}_{-1.6}$	1.9	7.2 ± 7.2	$0.45^{+0.23}_{-0.16}$	35.3/28
$Ginga$(4-30) + LE	$2.99^{+0.30}_{-0.33}$	3.4	$2.56^{+0.26}_{-0.20}$	1.3	0 (fixed)	$0.36^{+0.08}_{-0.07}$	23.4/22
$Ginga$(4-30) + LE	$2.98^{+0.37}_{-0.36}$	3.4	$2.56^{+0.40}_{-0.37}$	1.3	< 0.3	$0.36^{+0.09}_{-0.06}$	23.43/21

Table 6.6: Results of fitting the $Ginga$ spectrum of A1060 to models with one thermal and one non-thermal component. Unabsorbed fluxes are quoted, in units $10^{-11}\,\mathrm{erg\,s^{-1}\,cm^{-2}}$.

Datasets used	kT_i	f_{x_1}	kT_h	f_{x_2}	Index	Iron abundance	χ^2_{min} /d.o.f
$Ginga$(4-30)	-	-	$4.5^{+1.5}_{-1.2}$	4.7	1.12 ± 0.07	0.3 (fixed)	37.4/25
$Ginga$(4-30	$28^{+\inf}_{-24}$	0.40	3.7	4.4	$2.0^{+0.4}_{-0.3}$	< 1.23	34.2/22
$Ginga$(4-30) + LE	$4.0^{+0.9}_{-0.4}$	3.2	3.6	1.5	$1.31^{+0.94}_{-0.5}$	$0.22^{+0.06}_{-0.05}$	34.2/22

Table 6.7: Results of fitting the $Ginga$ spectrum of A1060 to models with an isothermal and a PLEM component. Unabsorbed fluxes are quoted, in units $10^{-11}\,\mathrm{erg\,s^{-1}\,cm^{-2}}$.

A model consisting of an isothermal and a non-thermal component also provides an adequate fit to the 2–18 keV $Ginga$ spectrum. The best fitting power-law slope is steep ($\Gamma \sim 2.1$) although it is only weakly constrained and is consistent with the value that might be expected if the non-thermal emission is due to an AGN in the cluster or in the field of view. Including the higher energy channels does improve the constraints on Γ and now the slope appears to be too steep to come from an AGN. There is no evidence for intrinsic absorption of the power-law component - only upper limits are obtained and addition of this extra free parameter does not survive application of the F-test. This (thermal + non-thermal) model also gives an acceptable fit when the LE point is included in the fitting procedure (although the power law index becomes very steep), and a much stronger limit on excess absorption is obtained ($N_H < 0.3 \times 10^{21}\,\mathrm{cm^2}$). The steepness of the power law index probably again reflects the existence of additional soft and hard components.

Attempts to model the spectrum with a PLEM model were less successful. One would expect the X-ray spectrum of a simple cooling flow cluster to be described by a model consisting of an isothermal component at temperature T_{iso} and a PLEM component cooling from $T_{high} = T_{iso}$ to some temperature below the detection capability of the instrument. In fact it proved impossible to find such a region of parameter space. The "best" fit to the *Ginga* data of this type gave $T_{high} = 3.7$ and $T_{iso} = 28.2$. Although T_{high} is formally consistent with T_{iso} (see Table 6.7), in actual fact the best isothermal component of the spectrum is just fitting the hard tail and the fit cannot be meaningfully interpreted as the spectrum of a cooling flow. Including the LE data point in the fit seems to make matters worse. In the case the "best" fit is for $T_{high} = 3.6$, $T_{iso} = 4.0^{+0.9}_{-0.4}$, but the χ^2 is formally unacceptable and the high energy residuals remain. (For all the fits in Table 6.7 the iron and other heavy element abundances in the cooling flow component were fixed at 0.3 solar).

For completeness, the *Ginga* data were also fit to a polytropic model. The β parameter was fixed at 0.7, consistent with the value determined by surface brightness fitting the *EXOSAT* LE data. The best fit gave a central temperature $T = 1.36^{+0.22}_{-0.20}$ and a polytropic index of $\gamma = 0.61^{+0.07}_{-0.05}$. Statistically, the fit was excellent ($\chi^2_\nu = 1.01$); unfortunately the resulting polytropic index is not physically meaningful.

In summary, the 0.1–18 keV spectrum of A1060 is complex. The spectrum is not adequately fit by the PLEM representation of a cooling flow. The 2–10 keV spectrum is consistent with a thermal component together with a non-thermal component probably representing emission from an AGN. If the AGN is at the same redshift as the cluster then the inferred luminosity is $L_x = 6 \times 10^{42} \, \mathrm{erg \, s}^{-1}$. The measured LE flux suggests that an additional soft component exists.

6.2.9 Virgo

EINSTEIN imaging observations of the Virgo cluster show that the X–ray emission originated from a region approximately 3° in diameter, centred on M87 (Fabricant & Gorenstein 1983). Analysis of spectral data taken with the HEAO-1 A2 and A4 experiments showed that a a hard, power-law component ($\Gamma \sim 2.5$) was present in the cluster (Lea *et al.* 1981), but the large field meant that the source of the hard X-rays could not be identified. Davison (1978) suggested the existence of a much more extended, hard, component, with the emission at energies > 7 keV centred on M86 and M84. Lea, Mushotzky & Holt (1982) reported *EINSTEIN* SSS observations which showed the existence of cooling gas near the centre and a non-thermal component associated with the nucleus of M87. Comparison of many spectral observations of the cluster from various satellites suggested that the non-thermal emission was variable. *EXOSAT* observations did little to clarify the situation - the data were consistent with the previous limits for hard X–ray emission from M87, and centred to the NW of M87 but the poor sensitivity of the ME to energies above 10 keV made the detection of stricter limits difficult (Edge 1989).

Hanson *et al.* (1990) presented Spacelab-2 coded mask images of the Virgo cluster in the 2–32 keV band. They found that NGC 4388 is the chief source of hard X–rays. The spectrum of the galaxy is consistent with that expected from a Seyfert 2, although the galaxy had been classified optically as a Seyfert 1. The best-fitting spectrum to the Spacelab data required a photon index $\Gamma = 1.5^{+0.9}_{-0.5}$ and an intrinsic column of $2.1^{+2.8}_{-1.4} \times 10^{23}$ cm^{-2}. Assuming that NGC4388 is at the same distance as the cluster the implied luminosity is 10^{42} erg cm^{-2} s^{-1}. Hanson *et al.* detected no hard power-law emission from M87.

Takano & Koyama (1991) utilised scanning data to show that in June 1988 hard X–ray emission was detected from NGC4388 and M87. The latter had a significantly larger photon index than the former ($\Gamma > 1.9$ compared to $\Gamma = 1.3$). The flux from the power-law component in M87 was a factor of 5 higher than the

kT (keV)	f_{x_1}	Γ	f_{x_2}	N_H (intrinsic)	Iron abundance	χ^2_{min} /d.o.f
$2.20^{+0.11}_{-0.10}$	23.2	$1.77^{+0.66}_{-0.90}$	4.04	0 (fixed)	$0.38^{+0.10}_{-0.07}$	21.5/21
$2.20^{+0.18}_{-0.26}$	23.2	$1.77^{+1.11}_{-0.97}$	4.07	$< 9.7 \times 10^{23}$	$0.38^{+0.34}_{-0.07}$	21.5/20
$2.23^{+0.07}_{-0.09}$	24.1	1.5 (fixed)	3.14	$< 4.5 \times 10^{23}$	$0.36^{+0.06}_{-0.04}$	22.1/21
$2.18^{+0.09}_{-0.14}$	22.6	1.9 (fixed)	4.63	$< 3.7 \times 10^{22}$	$0.40^{+0.08}_{-0.06}$	21.5/21

Table 6.8: Results of fitting the spectrum of the Virgo cluster to models with an isothermal and a non-thermal component. Unabsorbed fluxes are quoted, in units $10^{-11}\,\mathrm{erg\,s^{-1}\,cm^{-2}}$.

upper limit set by Hanson *et al.*; M87 must therefore be a variable hard X-ray source.

Thus the *Ginga* observations of the Virgo cluster are contaminated by at least one and possibly more non-thermal sources. Table 6.2 shows that an isothermal model is a very poor fit to the *Ginga* spectrum. The results of models including a non-thermal component are detailed in Table 6.8. If an absorbed power law component is added and the parameters are allowed to float freely then the power-law slope is very poorly constrained, although it is entirely consistent with previous reported values. The intrinsic column is only poorly constrained; if Γ is fixed at 1.9 then the upper limit is reduced to $N_H < 3.7 \times 10^{22}\,\mathrm{cm^{-2}}$, but the data do not require any intrinsic absorption. The inferred iron abundance is relatively insensitive to the assumed power-law slope.

Assuming that the distance of of the Virgo cluster is 15 Mpc, then the implied luminosity of the non-thermal source is $1.26 \times 10^{42}\,\mathrm{erg\,s^{-1}}$ if it is associated with M87. If the non-thermal source is entirely associated with NGC 4388 then the implied luminosity is much higher (as the collimator transmission is lower).

6.2.10 Centaurus

HEAO-1 observations revealed the Centaurus cluster to be non-isothermal (Mitchell & Mushotzky 1980). These authors found that the spectrum could be adequately fit by either:

- 2 isothermal components with $kT_1 = 2.3$ keV, $kT_2 = 8keV$.

- An isothermal component with $kT = 3$ keV and $\Gamma = 2.1$.

The results of an isothermal fit to the *Ginga* data are shown in Figure 6.7. It can be seen that the badness of fit is caused by excess emission at ~ 2 keV. In confirmation of this, adding a second power-law component to the model required a very steep photon index ($\Gamma = 3.4^{+4.3}_{-1.0}$) to obtain a formally acceptable fit.

Adding a second thermal component to the model gave more satisfactory results. The derived temperatures were $kT_1 = 3.59^{+0.13}_{-0.06}$ keV and $kT_2 = 1.04^{+0.57}_{-0.32}$ keV and the fit was excellent ($\chi^2_\nu = 1.05$). The two components were assumed to have the same iron abundance which was constrained to be $0.32^{+0.05}_{-0.03}$.

The 2–10 keV model fluxes were 1.21×10^{-10} erg s^{-1} cm^{-2} for the high temperature component and 4.4×10^{-12} erg s^{-1} cm^{-2} for the low temperature component. If the low temperature component originates from a cooling flow then the inferred mass flow rate is $\dot{M} \sim 26 M_\odot$ yr^{-1}, in agreement with previous imaging results (Edge & Stewart 1991a, Allen & Fabian 1994).
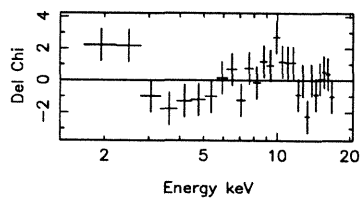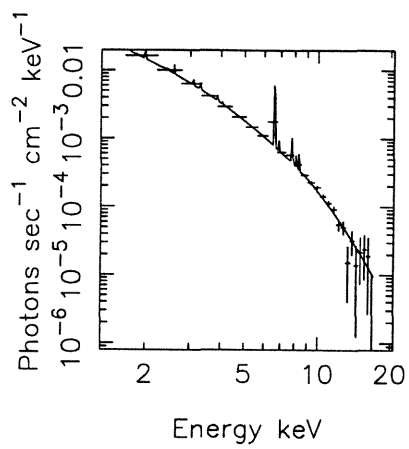
Figure 6.7: Incident spectrum and residuals obtained by fitting an isothermal model to the *Ginga* spectrum of the Centaurus cluster. Excess emission at $kT \sim 2$ keV is evident.

6.2.11 Coma

The Coma cluster (A1656) is the nearest, luminous cluster of galaxies and, as such, has been extensively observed at all wavelengths. Coma has often been described as an archetypal relaxed cluster, although recent optical and X–ray results have challenged this view. Optically, the cluster contains two D galaxies; Fitchett & Webster (1987) analysed the positions and radial velocities of the cluster galaxies and deduced the existence of two or more subclusters. The *EINSTEIN* image showed the cluster to be elliptical in shape (Chanan & Abramopoulos 1984), although it appeared to be smooth and not bimodal. There has been much discussion over the past ten years over the isothermality, or otherwise, of the gas in the Coma cluster. Henriksen & Mushotzky (1986) analysed HEAO-1 and OSO-8 observations of the cluster and claimed that a simple, isothermal model was not a good fit to the data ($\chi_\nu^2 = 2$ for $\nu = 22$). They fitted the data to polytropic models and obtained acceptable fits with a central temperature between 15.5 and 20.5 keV and a polytropic index $1.38 < \gamma < 1.6$. They suggested that this intermediate value of γ might be explained by an isothermal core in the cluster surrounded by an adiabatic region.

EXOSAT observations of Coma have been published by Hughes, Gorenstein & Fabricant (1988) (hereafter HGF) and by Edge (1989). The 45' field of view of the *EXOSAT* ME made possible a series of offset pointings of the outer regions of the cluster. Both of the above authors reach similar conclusions; the temperature of the cluster is higher in the core than it is in the outer regions. In detail, the spectra, and the previous Tenma data (Hughes *et al.* 1988, hereafter H88) were consistent with an hybrid model in which the cluster has an isothermal core with $T = T_{iso}$ for $R < R_{iso}$, with the temperature outside this region falling off polytropically: $T \propto \rho^{\gamma-1}$.

Pointed *Ginga* observations of Coma have been reported in Hughes *et al.* 1993 (hereafter H93). In this paper, data from the top and mid layers of the LAC are summed together to produce the pulse height spectrum. For consistency

Instrument	kT (keV)	FOV (°)	R_{eff} (')	Reference
Tenma	7.5 ± 0.2	3	20	H88
EXOSAT	8.5 ± 0.3	0.75	11	HGF
EXOSAT	7.39 ± 0.7	0.75	22	HGF
Ginga	8.08 ± 0.11	1×2	14	H93

Table 6.9: Results of isothermal fits to various measured spectra of the Coma cluster. Errors are 90% for one interesting parameter.

with the rest of the data in this thesis, here only data from the top layer of the LAC are used hence, although the results are entirely consistent with those in H93, the actual numbers quoted may not be identical. However, in order to facilitate comparison with results in H93 and from previous satellites, the errors quoted *in this section only* are 90% confidence for one parameter of interest $(\Delta\chi^2 = 2.706)$. The results of isothermal spectral fits on the Coma data in Table 6.2 show that the data are statistically well fit by a simple, isothermal model. The motivation for exploring more complex models comes from comparing the *Ginga* results with those from previous satellites. Table 6.9 shows the results of simple isothermal fits to the X–ray spectrum measured by several satellites; although each of the four sets of data gave acceptable fits to isothermal models, each measured a different temperature, with measured temperature decreasing with increasing field of view. Column 4 of Table 6.9 gives the count weighted radius for each instrument. H93 consider the effects of uncertainties in gain and background subtraction on the model parameters and conclude that these increase the total uncertainty on the measured temperature to 0.16 keV and make very little difference to the uncertainty in the iron abundance.

In view of the results from previous satellites, the *Ginga* data were fit to the hybrid isothermal/polytropic models described above. The radius and temperature of the isothermal region were free parameters in the fitting procedure while the polytropic index of the outer region and the X–ray surface brightness parameters were fixed at the values ($\gamma = 1.555$, $R_{core} = 6.'9$, $\beta = 0.60$) used by H88 and HGF. The spectral fitting was performed using the method described in H93;

the cluster was divided into a large number of radial shells. The temperature of each shell was calculated and the normalisation of each shell was determined by weighting by the square of its hydrogen density (assuming a King surface brightness profile) and convolving with the *Ginga* collimator response. The Raymond Smith spectra for the individual shells were summed to give the integrated cluster spectrum. This model gives a slightly improved χ^2 value: 10.5 for 22 degrees of freedom, (*c.f.* 11.9 for 23 d.o.f for the isothermal model), but the reduction in χ^2 is not significant. The best fit values, $T_{iso} = 8.7$ keV and $R_{iso} = 4.3R_{core}$ are consistent with the *EXOSAT* results of HGF at better 68% confidence and with the Tenma results of H88 at better than 90% confidence. Figure 6.8 shows the confidence contours for T_{iso} and r_{iso}. The shape of the contours indicates that an isothermal model cannot be ruled out by the data. H93 show that consideration of gain and background subtraction uncertainties can slightly increase the permitted region of parameter space. Taking into account the *EXOSAT* and *Tenma* results then the "best buy" hybrid model has $T_{iso} = 9.1$ keV and $R_{iso} = 3.33R_{core}$.

For completeness the *Ginga* data were also fit to the polytropic models used by Henriksen and Mushotzky (1986). For $\beta = 0.6$, the best fit value of the central temperature $T_c = 9.0^{+2.8}_{-0.9}$ keV and polytropic index $\gamma = 1.05^{+0.11}_{-0.05}$ (*ie* consistent with isothermal) but this model is not a significant improvement on the isothermal model. Fixing β at a value of 0.76 as used by Henriksen and Mushotzky results in values of $T_c = 8.45^{+2.4}_{-0.4}$ keV and $\gamma = 1.015^{+0.12}_{-0.015}$, significantly different from the revised allowed range of γ determined by Cowie, Henriksen & Mushotzky (1987) of $1.33 < \gamma < 1.43$.

Since the motivation for fitting non-isothermal models to the *Ginga* spectrum came from comparing isothermal temperatures measured by instruments with different sized fields of view, it is natural to compare the iron abundance measured by different instruments. As there is compelling evidence that the X–ray spectrum of Coma is best described by a non-isothermal temperature gradient, it is also necessary to compare iron abundances determined by fitting consistent models. Table 6.10 summarises previous iron abundance and flux determinations for
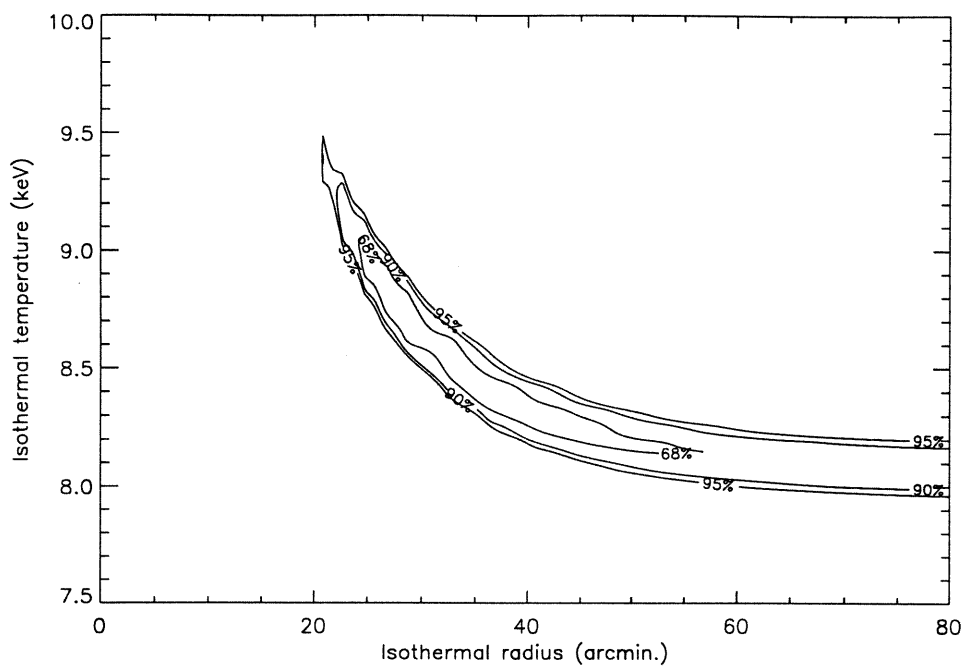
Figure 6.8: Results of fits to an hybrid model consisting of an isothermal core surrounded by a polytropic temperature distribution. The figure shows confidence contours for the temperature, T_{iso}, and radius, R_{iso}, of the isothermal region.

Instrument	2-10 keV flux ($\mathrm{erg\,cm^{-2}\,s^{-1}}$)	Iron abundance
Tenma	3.66×10^{-10}	0.237 ± 0.017
$EXOSAT$(centre)	2.84×10^{-10}	0.231 ± 0.032
$EXOSAT$(off-centre)	0.39×10^{-10}	$0.344^{+0.081}_{-0.146}$
$Ginga$	3.39×10^{-10}	0.247 ± 0.024

Table 6.10: 2-10 keV X–ray fluxes and iron abundance determinations for the best fit hybrid model of the spectrum of the Coma cluster described in the text.

the best-fitting hybrid model described above ($T_{iso} = 9.1 keV$, $R_{iso} = 3.33 R_{core}$. (Note that for consistency with H93, these are determined by fixing the abundance of iron to the abundance of all other heavy elements). It is clear that the measured fluxes increase with the field of view of the instrument, while the iron abundances are all consistent with an uniform value of 0.239 ± 0.013. This suggests that no strong abundance gradients exist in the Coma cluster. H93 use the integrated abundance determinations in Table 6.10 to provide a more quantitative description of the spatial distribution of iron. They find that the minimum iron mass within 3 Mpc is 17% (relative to cosmic abundance), compared with 24% assuming a uniform distribution of iron. This is consistent with the Spacelab observations of the Coma cluster (Watt *et al.* 1992) which fails to show any significant abundance gradient.

Finally, it was possible to obtain limits on non-thermal (power-law) emission from the Coma cluster. There is no evidence for a high energy tail in the X–ray spectrum out to almost 40 keV. The limits to the on-axis power-law emission (flux at 1 keV) are 1.6×10^{-3} photons $\mathrm{cm^{-2}\,s^{-1}\,keV^{-1}}$ for $\Gamma = 1.33$, 7.7×10^{-3} photons $\mathrm{cm^{-2}\,s^{-1}\,keV^{-1}}$ for $\Gamma = 1.77$ and 1.8×10^{-2} photons $\mathrm{cm^{-2}\,s^{-1}\,keV^{-1}}$ for $\Gamma = 2.21$. These values are about an order of magnitude less than the values inferred from baloon-borne hard X–ray experiments (Bazzano *et al.* 1984, Fusco-Fermiano *et al.* 1990) and are insensitive to the assumed absorption for the power-law component.

6.2.12 A1795

The spectrum was well fit ($\chi_\nu^2 = 0.83$) by an (isothermal+PLEM) model with $T_{high} = 6.8$ keV and $T_{iso} = 6.80^{+5.5}_{-0.6}$. The iron abundance in the cooling flow component was fixed at 0.25; the iron abundance in the isothermal component was then $0.27^{+0.10}_{-0.06}$ solar units. The inferred mass flow rate was $\dot{M} = 52^{+88}_{-22}\, M_\odot\,\mathrm{yr}^{-1}$, significantly below estimates from imaging satellites (the values of $\dot{M}$ derived from *EXOSAT* and *EINSTEIN* observations is $\sim 500\, M_\odot\,\mathrm{yr}^{-1}$). Siddiqui (1994 in preparation) also finds a discrepancy between mass flow rates determined using the PLEM model and those determined from the deprojection of surface brightness profiles.

6.2.13 A2163

A2163 is the hottest and most luminous cluster in the sample. *Ginga* and *EINSTEIN* observations of this source have been published by Arnaud *et al.* (1992a); the results presented here are in agreement with the published results. The inferred cluster luminosity is $L_x = 4.5 \times 10^{45}\,\mathrm{erg\,s}^{-1}$. The existence of such a massive cluster has significant implications for cold dark matter (CDM) models of the formation of structure in the universe. Arnaud *et al.* point out that in a CDM model with biased galaxy formation, A2163 would have corresponded to a 4.6σ fluctuation with no baising, or to a 6.9σ fluctuation if the bias parameter $b = 1.5$. They conclude that it is unlikely that the bias parameter is significantly greater than 1.

6.2.14 A2507

Ginga observations of this source have been published by Arnaud *et al.* (1991b), however the results presented in this work challenge the published results. The results shown in Table 6.2 show that an isothermal model is not a good fit to the cluster spectrum. If a simple power-law model is fitted instead then an acceptable

fit is obtained with $\Gamma = 1.93^{+0.06}_{-0.07}$ and the absorbing column fixed at the galactic value ($\chi^2_\nu = 0.81$).

There have been hints from observations in other wavebands that the X–ray source apparently associated with A2507 may be odd. The optical position of A2507 is 22 54 14 +05 14.0 (Abell 1958, 1950 coordinates). The cluster was identified with the *HEAO-1* source H 2256 +05.7 (Kowalski *et al.* 1984). Birkinshaw & Gull (1984) observed the cluster at radio wavelengths and saw a source at > 58 mJY at 10.7 GHz near the cluster centre. Observations at 408 MHz and 1402 MHz suggested a source at 22 54 11.8 +05 14 57. If the observations at the three frequencies were in fact the same source then the spectral index $\alpha^{10.7}_{1.4} \sim -1.1$, which Birkinshaw & Gull point out is very flat for a cluster source. These authors suggest that the *HEAO-1* source was wrongly identified with A2507.

The source in the Rosat All Sky Survey nearest to A2507 was 5' from the optical position and was apparently a point source, subsequently identified optically as an AGN with a $z < z_{cluster}$ (Edge priv. comm.). There is an Ultraviolet-excess galaxy within 10 arcmin of the cluster centre (Takase & Miyauchi-Isobe 1991) and an MCG galaxy at 22 54 +5 42 which is at redshift $z = 0.0249$.

As it seems likely that a non-thermal source is contributing strongly to, and perhaps dominating, the *Ginga* spectrum, A2507 is not included in the sample of clusters in the next chapter.

6.2.15 S2246-647

There is no published redshift for this cluster. The spectral parameters in Table 6.2 assume a redshift $z = 0.2$ (estimated in Kowalski *et al.* 1984). The redshift may be estimated by measuring the observed $K\alpha$ line energy; the 90% confidence interval for the redshift is $0.08 < z < 0.15$, lower than previous estimates.

Table 6.11 summarises the effects of varying the redshift on the derived cluster

z	kT (keV)	Iron Abundance	L_x (erg s^{-1})
0.08	$4.88^{+0.37}_{-0.34}$	$0.34^{+0.14}_{-0.12}$	3.1×10^{44}
0.15	$5.39^{+0.35}_{-0.34}$	$0.35^{+0.19}_{-0.14}$	1.1×10^{45}
0.20	$5.83^{+0.36}_{-0.33}$	$0.26^{+0.20}_{-0.16}$	2.1×10^{45}

Table 6.11: Effect of varying the redshift on the derived cluster parameters for S2246-647.

parameters.

6.2.16 A2634

An isothermal model was a poor fit to the 2–18 keV spectrum of this cluster. When the 2–12 keV spectrum was fit to an isothermal model an acceptable fit was obtained ($\chi^2_\nu = 1.1$), suggesting that a hard tail is present in the spectrum. A power-law component was therefore included in the model. Acceptable fits were obtained with the photon index fixed at 1.7 or 1.9, typical of AGN. For $\Gamma = 1.9$ the gas temperature was $kT = 2.64^{+0.32}_{-0.36}$ keV and the iron abundance was $0.39^{+0.18}_{-0.15}$. Including intrinsic absorption of the power-law source improved the fit but not significantly.

If Γ was allowed to be a free parameter in the fit then it was only very poorly constrained, reflecting the noisiness of the data; including the Mid layer data did not improve the constraints. The model described above with $\Gamma = 1.9$ is thus adopted as the 'best-buy' model for A2634. Assuming that the non-thermal source is associated with the cluster then the inferred 2–10 keV luminosity is $L_x = 1.6 \times 10^{43}$ erg s^{-1}.

The non-thermal source in A2634 may be associated with the central, radio source, 3C 465. De Robertis & Yee (1990) obtained long-slit spectroscopy of the nucleus of 3C 465. They subtracted the extra-nuclear absorption line component and uncovered a weak, high ionisation emission line spectrum with line widths ~ 850 km s^{-1}. The estimated luminosity of the non-thermal nuclear source was

$L = 10^{41.6}\,\mathrm{erg\,s^{-1}}$, and the inferred absolute V magnitude was -15.7 ± 0.6. De Robertis & Yee suggest that 3C 465 may be a 'dead' quasar.

The detection of hard X-ray emission from 3C 465 would be consistent with *Ginga* observations of the Cygnus A cluster/radio source (Ueno *et al.* 1994). Heavily absorbed power-law emission with $\Gamma = 1.98^{+0.18}_{-0.2}$ was detected. The inferred unabsorbed luminosity of the power-law source was $\sim 10^{45}\,\mathrm{erg\,s^{-1}}$, comparable to the cluster luminosity. Ueno *et al.* conclude that the evidence supports the idea that the nucleus of Cygnus A contains an obscured quasar.

6.3 Summary

Cluster spectra are complex; many are not well fit by isothermal models and even those that appear to be isothermal are revealed not to be so by closer inspection. In particular, non-thermal emission appears to be common in clusters and may be associated with subdued nuclear activity in radio galaxies. If the power-law index is allowed to float freely then the resulting value is often fairly steep, $\Gamma > 2$. This may reflect the existence of an additional soft component associated with emission from a cooling flow.

The iron abundance results are discussed more fully in the next chapter.

Chapter 7

Implications of the Ginga

Cluster Results

Overview

The spectral results of the previous chapter are summarised and interpreted in
the context of current models of the chemical evolution of clusters.

7.1   Summary of spectral results

The *Ginga* results provide an excellent sample for studying the spectral properties
of clusters, particularly iron abundances.

Table 7.1 summarises the results obtained from the 'best-buy' models in the previous chapter. Unabsorbed fluxes are quoted and a simple correction for collimator
transmission has been applied. The table also lists the derived X–ray luminosities.
An asterix indicates that the results quoted come from a non-isothermal model;
in these cases the quoted luminosity is the total luminosity if the non-isothermal
component represents cooling flow emission and the luminosity of the isothermal
component if the second component is best fit by a non-thermal model.

Cluster	Isothermal temperature (keV)	Iron abundance (solar units)	2–10 keV Luminosity (erg s^{-1}
A193	$3.02^{+0.39}_{-0.32}$	$0.29^{+0.29}_{-0.23}$	9.9×10^{43}
A262*	$3.13^{+17.57}_{-0.41}$	$0.31^{+0.13}_{-0.12}$	3.2×10^{43}
AWM7	$3.37^{+0.37}_{-0.33}$	$0.28^{+0.2}_{-0.15}$	8.9×10^{43}
Perseus	$6.17^{+0.44}_{-1.05}$	$0.41^{+0.13}_{-0.10}$	9.7×10^{44}
A478	$6.32^{+0.24}_{-0.23}$	$0.27^{+0.04}_{-0.04}$	2.5×10^{45}
A483	$8.40^{+2.0}_{-1.6}$	$0.15^{+0.28}_{-0.15}$	1.5×10^{45}
A496*	$4.3^{+1.2}_{-0.06}$	$0.29^{+0.07}_{-0.04}$	3.1×10^{44}
A520	$8.68^{+1.4}_{-1.1}$	$0.20^{+0.36}_{-0.20}$	1.3×10^{45}
A644	$6.50^{+0.17}_{-0.18}$	$0.26^{+0.04}_{-0.04}$	1.2×10^{45}
A665	$6.25^{+0.69}_{-0.60}$	$0.28^{+0.16}_{-0.14}$	13×10^{45}
A754	$9.31^{+0.30}_{-0.27}$	$0.19^{+0.05}_{-0.05}$	1.1×10^{45}
Hydra A*	$3.13^{+0.32}_{-0.33}$	$0.40^{+0.12}_{-0.19}$	2.2×10^{44}
A963	$6.08^{+1.6}_{-1.4}$	$0.10^{+0.43}_{-0.10}$	1.1×10^{45}
A1060*	$2.71^{+0.51}_{-0.15}$	$0.26^{+0.08}_{-0.06}$	2.2×10^{43}
A1367	$3.46^{+0.13}_{-0.13}$	$0.20^{+0.05}_{-0.06}$	5.6×10^{43}
A1413	$8.94^{+0.76}_{-0.65}$	$0.26^{+0.11}_{-0.11}$	1.6×10^{45}
MKW4	$1.46^{+0.14}_{-0.15}$	$0.77^{+1.8}_{-0.77}$	6.2×10^{42}
Virgo*	$2.20^{+0.11}_{-0.10}$	$0.38^{+0.10}_{-0.07}$	1.5×10^{43}
Centaurus*	$3.59^{+0.72}_{-0.13}$	$0.32^{+0.05}_{-0.03}$	7.3×10^{43}
Coma*	$9.1^{+0.10}_{-0.10}$	$0.22^{+0.02}_{-0.02}$	8.2×10^{44}
A1651	$5.87^{+0.35}_{-0.33}$	$0.25^{+0.10}_{-0.09}$	7.0×10^{44}
A1689	$9.73^{+0.67}_{-0.74}$	$0.24^{+0.11}_{-0.11}$	2.7×10^{45}
A1795*	$6.8^{+5.5}_{-0.6}$	$0.27^{+0.10}_{-0.06}$	9.3×10^{44}
A2009	$6.20^{+0.45}_{-0.40}$	$0.27^{+0.10}_{-0.08}$	1.5×10^{45}
MKW3S	$2.79^{+0.06}_{-0.05}$	$0.41^{+0.03}_{-0.04}$	1.9×10^{45}
A2142	$8.41^{+0.20}_{-0.21}$	$0.21^{+0.04}_{-0.03}$	2.9×10^{45}
AWM4	$2.65^{+0.44}_{-0.34}$	$0.37^{+0.41}_{-0.33}$	1.8×10^{43}
A2163	$13.0^{+1.1}_{-0.9}$	$0.19^{+0.13}_{-0.12}$	3.5×10^{45}
A2199	$4.08^{+0.08}_{-0.08}$	$0.26^{+0.02}_{-0.03}$	2.7×10^{44}
A2218	$6.05^{+1.65}_{-1.23}$	$0.07^{+0.30}_{-0.07}$	9.2×10^{44}
A2256	$7.11^{+0.66}_{-0.50}$	$0.23^{+0.11}_{-0.10}$	2.3×10^{44}
A2319	$8.95^{+0.06}_{-0.15}$	$0.19^{+0.03}_{-0.03}$	1.9×10^{44}
A2634*	$2.64^{+0.32}_{-0.36}$	$0.39^{+0.18}_{-0.15}$	5.1×10^{43}
S2246-647	$5.39^{+0.38}_{-0.34}$	$0.35^{+0.19}_{-0.14}$	1.2×10^{45}

Table 7.1: Summary of the spectral properties of the *Ginga* sample.
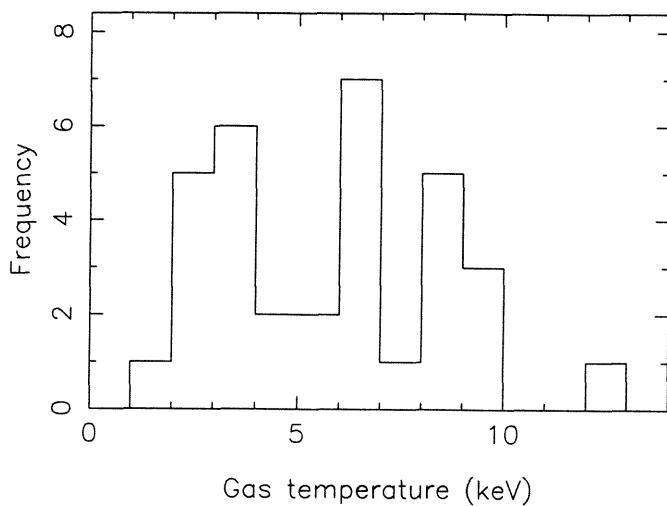
Figure 7.1: Histogram of measured isothermal temperatures.

Figure 7.1 shows the temperatures of the clusters observed by *Ginga*; there is a clustering around 3–4 keV. Figure 7.2 shows X-ray luminosity plotted against isothermal temperature (A262 has been excluded from the figure due to the excessively large error on the temperature). A clear correlation is seen which may be parameterised as $kT = 10^A \times L^B$, with $A = -16.9 \pm 3.1$ and $B = 0.39 \pm 0.07$ although there is substantial scatter and a straight line is a poor fit. The value of B is consistent with the value obtained by Edge & Stewart (1991a) and of Mushotzky (1984) but this is the first time that statistically significant scatter has been observed.

Edge & Stewart (1991a and b) have performed extensive correlations of the X-ray, optical and radio properties of a sample of 33 clusters. Because the *Ginga* sample is not an uniform sample, extensive repetition of the correlation will be avoided.

Of more interest than refining established correlations are the results on iron abundance. Figure 7.3 shows the measured iron abundances. One or two points appear as significant outliers; however there is a large dynamic range of errors in
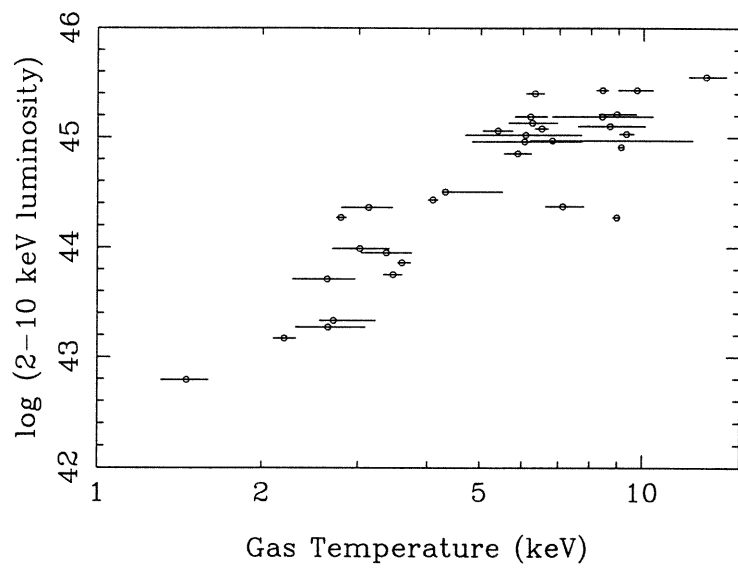
Figure 7.2: X-ray luminosity versus isothermal temperature.
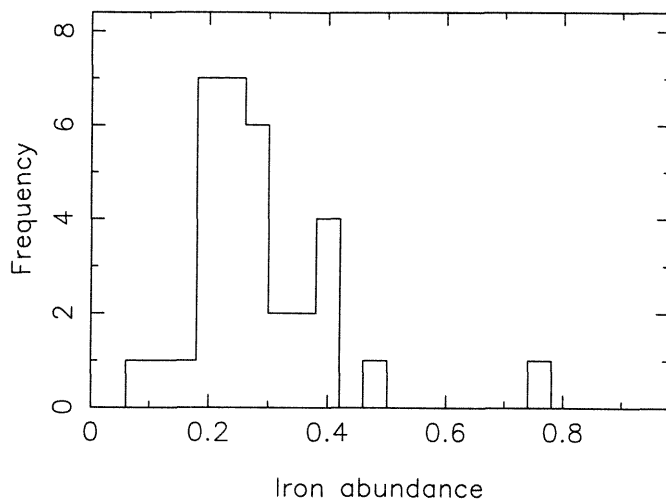
Figure 7.3: Histogram of cluster iron abundances.

the abundance determination and these points should be treated with caution. Figure 7.4 shows the weighted histogram of the iron abundances. There is a clear peak at ~ 0.3 but a significant spread of values exists. The weighted mean abundance is 0.27 ± 0.01 and the hypothesis that all clusters have this mean abundance can be rejected at greater than 99% confidence.

MKW4 is excluded from the analysis in the rest of this chapter as the iron abundance is so poorly constrained.

Figure 7.5 shows integrated iron abundance against temperature of the isothermal part of the cluster spectrum. Applying a Spearman rank correlation to the two parameters yields a value $r_{rank} = -0.71$, showing an anti-correlation significant at greater than 99%. If a straight line is fitted to the data (using errors on both x and y coordinates, (Press et $al.$ 1992)) then it may be parameterised as $Fe = a + b \times T$ with $a = 0.39 \pm 0.03$ and $b = -0.020 \pm 0.004$; however such a straight line is not a good fit.

Figure 7.6 shows the iron abundance plotted against the 2–10 keV luminosity.
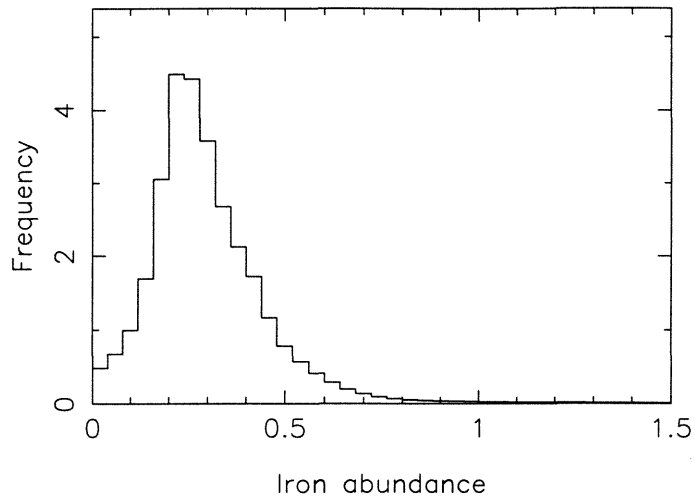
Figure 7.4: Weighted histogram of cluster iron abundances.
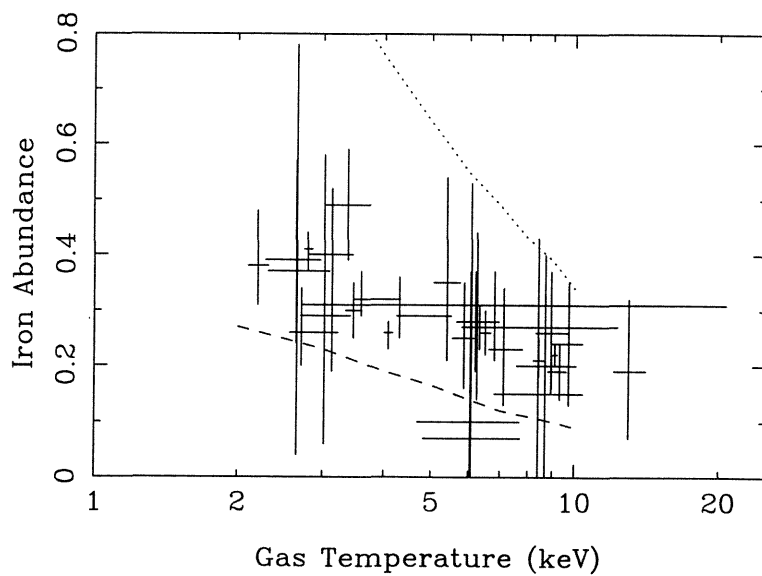
Figure 7.5: Iron abundance versus isothermal temperature. The two curves represents model predictions from David *et al.* 1991b described in section 7.3.
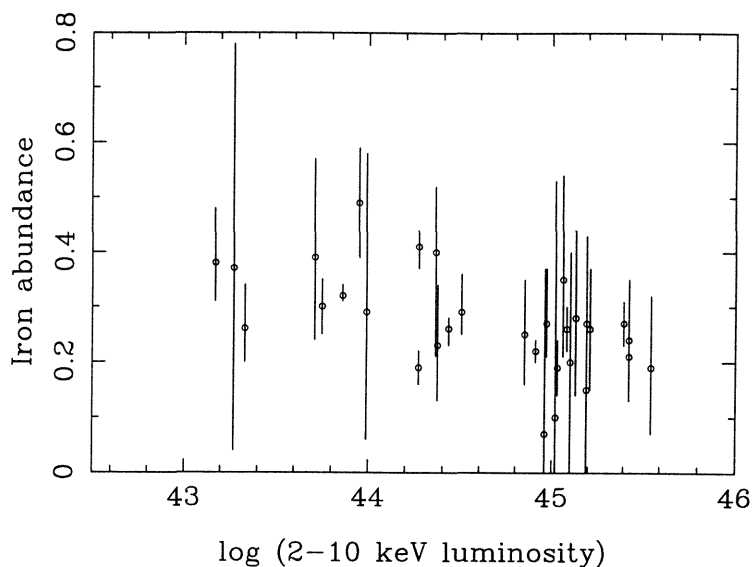
Figure 7.6: Iron abundance versus 2–10 keV luminosity.

There is less scatter and in this instance a straight line *is* an acceptable fit to the data and may be parameterised as

$$Fe = 10^{6.3} \times L_x^{-0.16 \pm 0.2} \tag{7.1}$$

It is known that deficiencies in the atomic data used in the RS code could lead to an apparent trend of abundance versus temperature in the sense observed in the data. For this reason the 'best buy' models summarised in Table 7.1 were fit to the data again with the RS components replaced by an isothermal plasma model derived from the code of Mewe *at al.* (1985, 1986). Temperatures obtained by using the Mewe code were in excellent agreement with those obtained using the Raymond & Smith code. Figure 7.7 shows the Mewe abundances plotted against the RS abundances. The iron abundances were systematically higher for the Mewe code; the mean was 0.33 ± 0.01, $\sigma = 0.1$, but the trend with temperature remained. We can again reject the hypothesis of uniform abundance between clusters and the Spearman rank correlation again indicates an highly significant anti-correlation between abundance and temperature. Thus we conclude that the

144
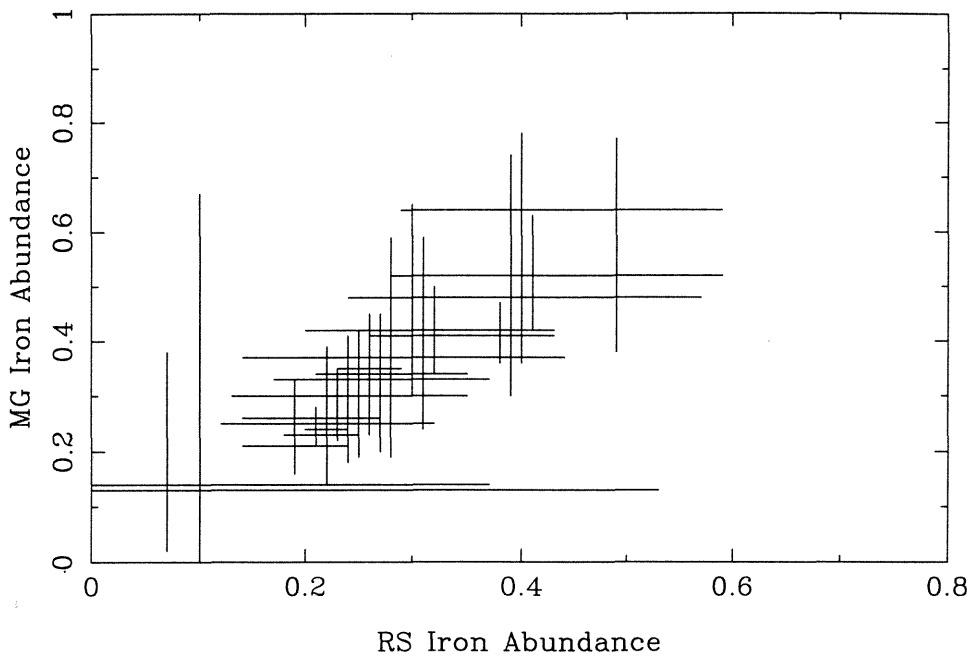
Figure 7.7: Iron abundances derived using the Mewe *et al.* code against iron abundances derived from the Raymond-Smith code.

tendency for richer clusters to have lower integrated iron abundances is real and not an artefact of the atomic data.

7.2 Interpretation of the abundance results

The apparently high abundances in less massive clusters may represent a real difference in iron enrichment or may be a result of a more centrally condensed distribution of iron in these clusters, similar to that reported (somewhat controversially) in the Perseus and Virgo clusters. Since *Ginga* measures the emission weighted spectrum, abundance gradients in poorer clusters would cause the iron enrichment to be over-estimated. The lack of spatial resolution of *Ginga* means that it is in general difficult to rule out the possibility of abundance gradients from *Ginga* data alone. However, as mentioned in the Chapter 6, *Ginga* observa-

tions of the Coma cluster require that the mass of iron within 2 Mpc is not less than 70% of that calculated assuming uniform enrichment (Hughes *et al.* 1993).

BBXRT results (Mushotzky 1992) do not appear to be consistent with strong abundance gradients in either rich clusters or poorer clusters such as Abell 262, although the spatial resolution was poor. Preliminary Asca results find a strong abundance gradient in the Centaurus cluster but not in poorer clusters generally (and none in Perseus !). However, these results *are* preliminary and it is important to remember that the complicated point spread function of the Asca XRT will tend to flatten out any abundance gradients in a quick analysis.

Various pieces of evidence and promising theories on the origin of the ICM and the evolution of clusters exist. Clearly it would be desirable to draw these together into a more coherent whole. Unfortunately the observational data required to constrain and test such models are often not up to the task and (as always) we await new instruments with new capabilites. Among the questions that need to be addressed are:

- How common *are* abundance gradients in clusters ?

- What are the relative ratios of gas mass and stellar mass in clusters and do they change with increasing total mass ?

- How do the answers to the previous question fit into an hierarchical merging scenario ?

- Where do the heavy elements in the ICM originate and how do they get out of the galaxies ?

- What part do cooling flows play in the abundance/merging drama ?

Models of the chemical evolution of clusters also need to include the likely populations of elliptical and spiral galaxies now and in the past.

The answer to the first question is beyond the scope of this work. The current

results have been noted above and the in the discussion that follows it is assumed that strong abundance gradients are uncommon.

A definitive answer to the second question requires accurate surface density profiles out to several Mpc. This will be addressed by *ROSAT* observations but, as yet, not enough have been published to allow a systematic study.

7.3   Models for the enrichment of the ICM

Rich clusters at the present epoch are dominated by elliptical galaxies; hence current iron production in clusters will be from type Ia supernovae (which have long-lived progenitors). The hot ISM of elliptical galaxies is typically 1-10% of the stellar mass; the mass of the ICM is at least comparable to the galactic mass in clusters. Thus the ICM has not originated from elliptical galaxies similar to those observed today.

The mass of iron is a simple product of the measured abundance and the gas mass if there are no abundance gradients. M_{gas}/M_* (where M_* is the stellar mass) inreases with M_{tot}, but iron abundance decreases with increasing temperature (or equivalently M_{tot}). Arnaud *et al.* (1991) and Tsuru (1991) have collated the available gas masses and optical luminosities and both find that the ratio M_{Fe}/M_* is constant and equal to 2×10^{-3}.

The present type Ia supernova rate is given by

$$R_{SN1a} = 0.075 \left(\frac{\tau}{100 \, \mathrm{yr}} \right) \left(\frac{L_B}{10^{10} L_\odot} \right) \tag{7.2}$$

(van den Bergh, McClure & Evans 1987). Nomoto *et al.* have calculated that a type Ia supernova synthesizes $0.6 \, M_\odot$ of iron. If the SN1a rate has been constant over an Hubble time then, assuming a ratio $M_{\mathrm{star}}/L_B = 6$ (Faber & Gallagher 1979), the total mass of iron is estimated as

$$1.5 \times 10^9 M_\odot \left(\frac{M_*}{10^{13} M_\odot} \right) \tag{7.3}$$

147

The integrated mass loss from evolved stars in elliptical galaxies is less than this (Faber & Gallagher 1976), thus the total iron produced by type I SNa, assuming a constant rate, is a factor of 10 below that which is observed.

As the supernovae which are actually observed in elliptical galaxies today cannot have produced the iron observed in the ICM, much attention has been focussed on models in which the iron is ejected during an early wind phase.

At earlier times type II supernovae would be more frequent as the massive stars would be evolving most rapidly. There is also evidence from *EINSTEIN* FPCS measurements of oxygen abundance that type II SN may have contributed to the enrichment of the ICM. The cosmic mass ratio of oxygen to iron is 4.7. The mass ratio of oxygen to iron synthesised by type I SN is 0.18 and by type II SN is 36. Canizares *et al.* 1982, and Canizares, Merkert & Donahue (1988) find that oxygen is overabundant by a factor of 3 relative to iron.

Matteucci & Vettolani (1988) calculated the predicted iron abundance in the ICM by considering the contributions from both type I SN (whose progenitors were assumed to be white dwarfs in binary systems exploding by C-deflagration) and type II SN in elliptical galaxies. They find that most of the iron is actually ejected after the early wind phase and that most of the iron comes from SN with long-lived progenitors. They conclude that the bulk of the gas in clusters must be primordial. The predicted iron abundance in a cluster is only weakly dependent on cluster properties (*e.g* richness, fraction of ellipticals) but depends on the model for galactic chemical evolution. Any variation in iron abundance must therefore be due to variations in the gas mass to total mass ratio. The observed and predicted abundances were in good agreement (although for only 4 clusters were there sufficient data to calculate the model abundance). However, Arnaud *et al.* (1991b) point out that the type I SN rate used is a factor of 3 below the currently favoured value given in Equation 7.2 which would reduce the mass of iron injected into the ICM by a similar factor. The hydrodynamic simulations of David *et al.* (1991a) have cast doubt on the existence of the second wind phase

during which much of the iron is supposed to be ejected.

David *et al.* (1991b,1991a,1990b) have simulated the dynamic and X–ray evolution of the ISM in elliptical galaxies. They find that all elliptical galaxies go through an early wind phase. The iron abundance in the ICM due to galactic winds from elliptical galaxies was found to be

$$(Fe/H) = \frac{f_E f_{Fe}}{1 - f_w} \frac{M_*}{M_{ICM}} \tag{7.4}$$

where f_w and f_{Fe} are the fraction of the original luminous mass of a cluster that are ejected as gas and iron respecitvely. f_E is the fraction of early type galaxies in a cluster. An analogous equation applies to the oxygen abundance. The oxygen abundance remains constant after the early phase during which all the massive stars evolve through the SN phase. The iron abundance changes as iron is injected into the cluster through type I SN or through stripping.

The dotted line on Figure 7.5 shows the predicted abundances for a model with an initial mass function slope, $x = 1$. (The IMF is assumed to vary as $\phi(m) = a \, m^{-(1+x)}$). The galaxies are assumed to retain a solar abundance of iron; this was the "best buy" model of David *el al.* 1991b. It can be seen that this model over-predicts the iron abundance in all clusters and predicts a much steeper variation of abundance with temperature than is actually observed. On the other hand the model with an IMF of $x = 1.5$ (the dashed line on Figure 7.5) does not eject sufficient iron into ICM to account for the observed abundances. Clearly a model with an intermediate value of x could, in principle, reproduce the observed results. Models with a Salpeter IMF cannot supply enough iron through galactic winds to account for the observed results. There are two major caveats to these models:

⊚ The temperature dependence in the model is due to the increased dilution of the SN ejecta by the ICM in richer clusters. If the gas mass to total mass ratio is found not to increase with total mass then this is not valid.

⊚ The models use the relation $f_E = 1.0 - 0.63(T_{ICM}/2\,\text{keV})^{-0.34}$ to give the

fraction of early type galaxies (Edge 1989). If the clusters we observe are the aggregation of smaller sub-units then T_{ICM} and hence the fraction of early type galaxies at the wind epoch will be significantly smaller. (The timescale for enrichment by winds is $\sim 2 \times 10^8$ yr, less than the timescale for merging to form a rich cluster). Alternatively the present population of ellipticals on rich clusters may be the result of ram-pressure stripping by the ICM; again this would imply that the spiral fraction may have been much larger at the wind epoch.

Arnaud *et al.* 1990 claim that the models of David *et al.* successfully explain the metallicity of the ICM but cannot account for the metal content of stars. Arnaud *et al.* (1990) consider a model with bimodal star formation - more massive stars were born at earlier epochs. Only very preliminary results were presented but they were encouraging.

Chapter 8

Conclusions and Future Prospects

Overview

The two halves of this thesis were intended to be largely 'standalone' and Chapters 4 and 7 have summarised the results of the studies of the XRB and clusters respectively. This chapter reiterates the main results and briefly discusses the progress that will be made by the next generation of satellites (beginning with Asca).

8.1   *Ginga* observations of XRB fluctuations

8.1.1   The current state of play

As discussed in Chapter 3, the *Ginga* fluctuation data show no correlation with galactic latitude. As the data were restricted to $|b| > 25°$, this is perhaps not surprising.

The fluctuation data were fit to model P(D) curves in two energy bands, 2–4 keV

and 4–12 keV. The slopes of the inferred source counts were consistent with each other and with an Euclidean slope. The normalisations where consistent with each other and with the normalisation inferred from the Piccinotti *et al.* sample. Thus the differential source counts are consistent with

$$N(S) = 2 \times 10^{-15} S^{-2.5} \left(\text{erg cm}^{-2} \, \text{s}^{-1} \right)^{2.5} \text{sr}^{-1}$$

over the flux range $S_{(2-10)} = 10^{-10} - 5 \times 10^{-13}$ erg cm^{-2}s^{-1}.

The normalisation of the source counts inferred from the *Ginga* fluctuations is a factor $\sim 2 - 3$ above that derived in the 0.3-3.5 keV band from the EMSS if a spectral conversion is assumed which ignores X–ray absorption intrinsic to the sources. An investigation of the limits on the excess variance reveal no evidence for source clustering. It is not possible to explain the discrepancy with the EMSS by increasing the excess variance.

The 2-18 keV spectrum of the fluctuations is best fit by a model including a reflection component, as observed in AGN. There is no significant difference between the properties of fluctuation fields which contain an Abell cluster and those that do not.

The contribution of galactic sources to the fluctuations is $< 10\%$. Clusters of galaxies and BL Lac objects make only small contributions. Model AGN source counts were constructed which assumed that:

1. AGN exhibit pure luminosity evolution of the form $L_x(z) = (1+z)^A L_x(0)$, consistent with optical and soft X–ray data.

2. low luminosity AGN ($L < L_{abs}$ erg s^{-1}) are absorbed by some column C.

There is a region of parameter space around $A \sim 2$, $L_{abs} = 10^{43}$ erg s^{-1}, $z_{max} \sim 2$ and $C \sim 10^{22}$ cm^{-2} where the predicted source counts agree with the observed source counts in both the 2–10 keV and 0.3–3.5 keV band. It is necessary to truncate the models at $L_{min} = 10^{42.5}$ erg s^{-1} in order to avoid overproducing the X–ray background.

These models predict that low luminosiy AGN are the main contributors to the
XRB at flux levels $\sim 5 \times 10^{-13}$ erg s^{-1} cm^{-2} and that the EMSS missed significant
numbers of sources due to intrinsic absorption.

8.1.2 Future Prospects

Asuka (the name means 'Flying Bird' in Japanese) was launched in February
1993. The scientific payload consists of 4 coaligned telescopes feeding into two
CCD cameras (22×22 arcmin field of view), sensitive from 0.5-10 keV and two
Gas Imaging Spectrograms with slightly larger fields of view and slightly harder
responses. Asca has provided the first opportunity to directly image the hard
XRB. If the models described in Chapter 4 and above are correct then it is to be
expected that deep survey observations with Asca will detect significant numbers
of absorbed sources not observed in soft X-rays.

One such highly absorbed AGN, NGC6552, was observed serendipitously (Fukazawa
et al. 1994), but clearly many deep field observations are necessary to determine
whether similar objects are present in sufficient quantities. An exposure time of
50 ksec translates to a flux level of $\approx 3 \times 10^{-14}$ erg cm^{-2} s^{-1} at the 5σ detection
threshold. At this point about half of the 2-10 keV XRB is resolved.

The X-ray Timing Explorer (XTE) will carry two non-imaging instruments cov-
ering an energy range 2-250 keV. While the satellite is designed for temporal
studies it will be able to study the broad band X-ray spectra of hundreds of
AGN and study the energy spectra of the fluctuations (Rothschild 1992).

JET-X, due to be launched on Spectrum X-Γ in 1995, may be considered as
a spectral counterpart of ROSAT. It will have similar angular resolution and
sensitivity to the PSPC, but $\Delta E/E \sim 70$ in 2-10 keV. SODART, which will be
launched on the same satellite will have be sensitive from 0.5-10 keV.

AXAF, due to be launched in 1999, will have 0.5 arcsecond spatial resolution

and will observe at flux levels $\sim$ 50-100 times more sensitive than the *EINSTEIN* Deep Surveys.

XMM, due to be launched in 1999, will be the next satellite to have an effective area comparable to that of *Ginga* (XMM will have $\sim$ 3000 cm^{-2} at 6 keV).

These satellites will provide deep, resolved source counts and should be able to determine the spectra of these sources as functions of L and z. At fainter fluxes they will provide data for fluctuation studies with improved spectral resolution. The energy spectrum of the unresolved background will be better constrained.

Mushotzky (1989) predicts that 'by one year after the launch of AXAF/XMM.......... the problem of the XRB in the 2–10 keV band will be "algebraically solved" ', *ie.* the contributions of all known sources and any residual diffuse emission will have been quantified and will sum to the flux of the XRB.

8.2   *Ginga* observations of clusters of galaxies

As described in Chapter 6, *Ginga* observations have shown that cluster spectra are, in general, non-isothermal. Departures from isothermality may be due to the presence of cooling gas in the cluster or to the presence of a non-thermal source in the FOV/cluster. A continuing frustration in this work has been the fact that the *Ginga* data, while excellent for ruling out isothermal models, have not always been up to the task of distinguishing between or constraining non-isothermal models. There is some evidence that hard X–ray emission from central radio sources is common.

The weighted mean iron abundance determined by *Ginga* is 0.27 $\pm$ 0.01 and there is a clear anti-correlation between iron abundance and gas temperature. This correlation is insensitive to the exact plasma code which is used and is thus considered to be real and not a consequence of poorly understood atomic physics.

The iron abundance results are consistent with models of enrichment by type II supernovae during an early wind driven phase. In these models the temperature dependence comes from the increase of gas mass to stellar mass with increasing total mass, causing greater dilution of the iron in richer clusters and lowering the measured abundance. However, these enrichment models do not successfully account for all the known properties of clusters and should probably still be regarded as preliminary.

8.2.1 Future Prospects

Surprisingly few *ROSAT* cluster observations have been published to date. Eventually it will be possible to compile a large number of results on the gas mass out to distances > 3 Mpc. Even with such a dataset, further optical data are necessary to confirm the result that the gas mass to galaxy mass ratio is higher in rich clusters.

Asca will begin to address the issue of temperature and abundance gradients in clusters but the results will be limited by the point spread function of the telescopes. Preliminary results suggest that abundance gradients are not common, though such a gradient does exist in Centaurus. Asca will be able to constrain the origin of the hard emission seen in many clusters and to constrain the abundance of other heavy elements besides iron.

The improved spatial resolution of JET-X will allow significant progress on temperature and abundance variations in clusters. Knowledge of the temperature profile in clusters is important in determining model-independent cluster masses and in interpreting microwave decrement results for SZ experiments.

The results obtained from JET-X and Asca will be limited by the need to bin up the data spatially to obtain sufficient counts (due to the small effective areas). The large effective area of XMM will enable the determination of spatial variations in the abundance of many heavy elements out to several core radii.

155

8.3 A Final Word

In the Prequel it was stated that there was no strong link between the two scientific topics contained in this thesis. This chapter has slightly weakened this statement. There is an ever present cry of "we need more data" in all branches of X–ray astronomy. The study of the XRB and the study of clusters of galaxies both specifically require 0.5–10 keV spectral imaging data, rather than high time resolution data or just higher resolution spectroscopy.

The high levels of star-forming activity required to produce the iron abundances and the possibility that starburst galaxies may, with evolution, contribute to the XRB, could be regarded as another tenuous link between the two subjects.

And what *is* the contribution of clusters to the X–ray background ? - not very much, based on present evidence.

Appendix A

Some relevant cosmology etc.

A simple derivation of the log N–log S relation for sources of identical power and an outline of the mathematical basis behind the P(D) analysis.

A.1   The log N–log S relation

This section derives the log N–log S relation from a purely kinematic cosmology in the simplified case where all sources have equal luminosity. A more complete derivation is found in chapter 14 of Weinberg (1972) and results from that work are quoted below.

The cosmological principle states that the universe is both homogeneous and isotropic; hence it can be described by a Robertson Walker metric in comoving co-ordinates

$$ds^2 = dt^2 - R^2(t) \left[\frac{dr^2}{1 - kr^2} + r^2 \left(d\theta^2 + \sin^2\theta d\phi^2 \right) \right] \qquad \text{(A.1)}$$

At radial co-ordinate r the element of proper volume is

$$dV = \frac{R(t)dr}{(1 - kr^2)^{1/2}} R r d\theta R r \sin\theta d\phi \qquad \text{(A.2)}$$

So for one steradian of a spherical shell

$$dV = \frac{R^3(t)r^2 dr}{(1 - kr^2)^{1/2}} \tag{A.3}$$

Let there be $n(t)$ sources per unit proper volume at time t, which move apart as the volume expands. The number of sources per steradian is then

$$dN = \frac{n(t)R^3(t)r^2 dr}{(1 - kr^2)^{1/2}} \tag{A.4}$$

Since co-moving number density is conserved

$$dN = \frac{n_0 R_0^3 r^2 dr}{(1 - kr^2)^{1/2}} \tag{A.5}$$

The number of sources per steradian out to radius r_1 is

$$N(r_1) = n_0 R_0 \int_0^{r_1} \frac{r^2 dr}{(1 - kr^2)^{1/2}} \tag{A.6}$$

We wish to consider the number of sources brighter than some flux S

$$S = \frac{P}{4\pi R_0^2 r_1^2 (1 + z)^2} \tag{A.7}$$

(since luminosity distance $d_L = r_1 R(t_0)(1 + z)$).

If we consider a set of sources with the same P then A.7 is a relation between R_0, r_1, z and S. Substituting the r, z relation

$$R_0 r_1 = \frac{c}{H_0}[z - \frac{1}{2}(1 + q_0)z^2] \tag{A.8}$$

in A.7 and A.6 for the case $(k = 0)$ gives

$$S(z) \approx \frac{PH_0^2}{4\pi c^2 z^2}(1 - (1 - q_0)z) \tag{A.9}$$

and

$$N(z) \approx \frac{n_0 c^3 z^3}{3H_0^3}(1 - \frac{3}{2}(1 + q_0)z) \tag{A.10}$$

Now A.9 and A.10 may be combined to eliminate z and yield the $N - S$ relation

$$N(> S) = \frac{n_0 P^{3/2}}{3(4\pi)^{3/2}} S^{-3/2}[1 - 3z] \tag{A.11}$$

or substituting $z \approx (PH_0^2/4\pi S)^{1/2}$

$$N(> S) \approx \frac{n_0 P^{3/2}}{3(4\pi)^{3/2}} \left\{ 1 - \left(\frac{PH_0^2}{4\pi S} \right)^{1/2} \right\} S^{-3/2} \tag{A.12}$$

158

When the effect of the spectrum K-correction is included then A.7 becomes

$$S(\nu_0) = \frac{P(\nu_0(1+z))}{(1+z)(4\pi R_0^2 r_1^2)} \qquad (A.13)$$

For sources with power law spectra, *ie* $S(\nu) \propto \nu^{-\alpha}$,

$$S(\nu_0) = \frac{P(\nu_0)}{(1+z)^{\alpha+1}4\pi R_0^2 r_1^2} \qquad (A.14)$$

This derivation has assumed that all sources have the same intrinsic power; although this premise is known to be false, the derivation is valid provided that the spread in intrinsic source power is small compared to the spread in received power. The more general derivation in Weinberg (1972) does not assume that sources have identical luminosities. The general N-S relation, including the K-correction is

$$N(> S, \nu) = \frac{4\pi}{3} S^{-3/2} \int_0^\infty n(t_0, P, \nu) \left(1 - \frac{3}{2}(\alpha+1)\left(\frac{PH_0^2}{2}\right)^{1/2}\right) P^{3/2} dP \qquad (A.15)$$

where $n(t_0, P, \nu)$ is the number density of sources with luminosities between P and $P + dP$, at frequency ν, at time t_0.

It can be seen that, even in a flat universe, in the absence of evolution $N(> S)$ must increase more slowly than the simple Euclidean result $N(> S) \propto S^{-3/2}$. Thus source counts which appear to follow the Euclidean form must be exhibiting some form of evolution.

A.2   How the fluctuations arise

If there are N sources per steradian then the mean number of sources in a beam of solid angle $\delta\Omega$ is just

$$N' = N\delta\Omega \qquad (A.16)$$

For large N and small $\delta\Omega$, N' follows the Poisson distribution. The expected beam to beam variations in numbers of sources are then

$$\frac{\delta N'}{N'} = (N\delta\Omega)^{-1/2} \qquad (A.17)$$

159

These variations cause fluctuations in the beam to beam radio or X–ray counts. The use of fluctuations to study the confusion noise of unresolved radio sources was developed by Scheuer (1957) for interferometers and by Condon (1974) and Scheuer (1974) for pencil beam antennae. The distribution of fluctuations is characterised by a $P(D)$ (Probability of Deflection) curve. $P(D)dD$ is the differential probability that an observation of radio or X–ray intensity will have a deflection D from the mean.

It is not possible to deduce $N(S)$ from the fluctuation distribution (Scheuer 1957). Instead the $P(D)$ curve corresponding to a model $N(S)$ must be calculated and compared to the observed fluctuations. A brief derivation of the $P(D)$ distribution is given below, following that in Condon (1974) and Scheuer (1974).

A.2.1 From $N(S)$ to $P(D)$

We consider a small element of a detector with solid angle $\delta\Omega$ and response η. If dS is sufficently small then the probability of finding a source in $\delta\Omega$ with flux between S and $S + dS$ is just $N(S)dS\delta\Omega$, The mean number of sources with measured intensity between x and $x + dx$ is then

$$R(x)dx\delta\Omega = N\left(\frac{x}{\eta}\right)\frac{dx}{\eta}\delta\Omega \qquad (A.18)$$

The mean number over the whole detector is given by

$$R(x)dx = \int N\left(\frac{x}{\eta}\right)\frac{dx}{\eta}d\Omega \qquad (A.19)$$

For a simple power law form for the source counts, *ie*

$$N(S) = KS^{-\gamma} \qquad (A.20)$$

then

$$R(x) = K\Omega_e x^{-\gamma} \qquad (A.21)$$

where Ω_e, the effective beam solid angle is defined by

$$\Omega_e = \int [\eta(\theta,\phi)]^{\gamma-1}d\Omega \qquad (A.22)$$

160

$(\eta(\theta, \phi)$ is the 2-dimensional response pattern). The characteristic function of $R(x)$ is

$$r(\omega) = \int_0^\infty R(x)e^{i\omega x}dx \qquad (A.23)$$

(Scheuer 1974).

The characteristic function of $X = \Sigma x$ is

$$\exp(r(\omega) - r(0)) \qquad (A.24)$$

(Scheuer 1957). The characteristic function for $D = X- < X >$ is obtained by multiplying A.24 by the characteristic function for a delta function

$$p(\omega) = exp[r(\omega) - r(0) - i\omega < X >] \qquad (A.25)$$

or

$$p(\omega) = \exp \int_0^\infty R(x)(e^{i\omega x} - 1 - i\omega x)dx \qquad (A.26)$$

$P(D)$ is then just the Fourier transform of $p(\omega)$

$$P(D) = \frac{1}{2\pi} \int_{-\infty}^\infty p(\omega)e^{-i\omega D}d\omega \qquad (A.27)$$

For power law $N(S)$ then equation A.26 for $p(\omega)$ may be integrated by parts to give

$$p(\omega) = \exp[K\Omega_e(-\gamma)!(-i\omega)^{\gamma-1}] \qquad (A.28)$$

$P(D)$ can then be expanded as a power series

$$P(D) = \frac{1}{\pi(\gamma - 1)} \sum_{r=0}^\infty \frac{(t - 1)!\sin t\pi D^r}{(K\Omega_e(-\gamma)!)^t r!} \qquad (A.29)$$

where $t = (r + 1)/(\beta - 1)$.

Condon (1974) shows that the $P(D)$ scales as

$$P[(K\Omega_e)^{1/(\gamma-1)}D] = (K\Omega_e)^{-1/(\gamma-1)}P(D) \qquad (A.30)$$

Thus the shape of the $P(D)$ distribution depends only on γ, while the width of the distribution is proportional to $(K\Omega)^{1/(\gamma-1)}$.

For $\gamma > 2$ the total background diverges, indicating that the source counts must turn over at some flux level. The fluctuations are convergent for $\gamma < 3$. For γ just greater than 2 the fluctuations are dominated by the bright sources. As γ approaches 3 the weak sources dominate.

A.3 Using the computer

Shafer (1983) gives a detailed explanation of the techniques involved in construct-
ing and fitting model P(D) curves on the computer and the reader is referred to
this work for a full description. Here only a few brief details are summarised,

The distribution of intensities was represented by an array of 8192 points. This
was used to calculate the fluctuation distribution using Fast Fourier Transorm
techniques. A sharp cut off at some flux S_{min} was applied and an additional
pure Gaussian component of variance σ_{ex} was convolved with the transformed
fluctuation distribution by multiplying this distribution by a Gaussian. Applying
the inverse transform then gives the model fluctuation distribution.

References

·Abell, G.O., 1958, *Astrophys. J. Suppl.*, **3**, 211.

Abell, G.O., Corwin Jr, H.G. & Olowin, R.P., 1989, *Astrophys. J. Suppl.*, **70**, 1.

Abramopolous, F. & Ku, W., 1983, *Astrophys. J.*, **271**, 446.

Allen, S.W., Fabian, A.C., Johnstone, R.M., Nulsen, P.E.J. & Edge, A.C., 1992. *Mon. Not. R. astr. Soc.*, **254**, 51.

Allen, S.W. & Fabian, A.C., 1994, *Mon. Not. R. astr. Soc.*, **269**, 409.

Arnaud, K.A., 1988, in *"Cooling flows in Clusters and Galaxies"*, ed A. C. Fabian, Kluwer, p31.

Arnaud, K.A., Serlemitsos, P.J., Marshall, F.E., Petre, R., Jahoda, K., Boldt, E., Holt, S.S., Mushotzky, R.F., Swank, J.H. & Szymkowiak, A.E., 1992, In: *Frontiers of X–ray astronomy'*, ed Koyama, K. & Tanaka, Y., Univ. Acad. Press, p481.

Arnaud, M., Lachieze-Rey, M., Rothenflug, R., Yamashita, K. & Hatsukade, I., 1991b, *Astr. & Astrophys.*, **243**, 56.

Arnaud, M., Hughes, J.P., Forman, W., Jones, C., Lachieze-Rey, M., Yamashita, K. & Hatsukade, I., 1992a, *Astrophys. J.*, **390**, 345.

Arnaud, M., Rothenflug, R., Boulade, O., Vigroux, L. & Vangioni-Flam, E., 1992b, *Astr. & Astrophys.*, **254**, 49.

Barcons, X., 1987, *Phys. Rep.*, **313**, 547.

Barcons, X. & Fabian, A.C., 1988, *Mon. Not. R. astr. Soc.*, **230**, 189.

Barcons, X. & Fabian, A.C., 1989, *Mon. Not. R. astr. Soc.*, **237**, 119.

Barcons, X. & Fabian, A.C., 1990, 1989, in *"Two topics in X–ray astronomy. Vol. 2: AGN and the X–ray background"*, Proceedings of the 23rd ESLAB sypmosium, (European Space Agency, Paris), p733

Barcons, X. & Fabian, A.C., 1992, *Ann. Rev. Astr. Astrophys.*, **30** 429

Baum, S.A., 1992, in *"Clusters and Superclusters of Galaxies"*, ed A. C. Fabian, Kluwer, p171.

Bazzano, A., Fusco-Fermiano, R., La Padula, C., Polcaro, V.F., Ubertini, P. & Manchanda, R.K., 1984, *Astrophys. J.*, **279**, 515.

Beers, T.C. & Tonry, J.L., 1986, *Astrophys. J.*, **300**, 557.

Bevington, P.R., 1969, *'Data Reduction and Error Analysis in the Physical Sciences'*, (McGraw-Hill, New York)

Birkinshaw, M. & Gull, S.F., 1984, *Mon. Not. R. astr. Soc.*, **206**, 359.

Birkinshaw, M., 1990, in *The Cosmic Microwave Background: 25 years later*, eds. Mandolesi, N. & Vittorio, N. (Dordrecht; Kluwer), p77.

Birkinshaw, M., Hughes, J.P. & Arnaud, K.A., 1991, *Astrophys. J.*, **379**, 466.

Boldt, E.A., 1987, *Phys. Rep.*, **146**, 215

Boyle, B.J., Griffiths, R.E., Shanks, T., Stewart, G.C. & Georgantopoulos, I., 1993, *Mon. Not. R. astr. Soc.*, **260**, 49.

Bradt, H., Mayer, W., Naranan, S., Rappaport, S. & Spuda, G., 1967, *Astrophys. J. (Letters)*, **161**, L1.

Bregman, J.N., 1992, in *"Clusters and Superclusters of Galaxies"*, ed A. C. Fabian, Kluwer, p119.

Briel, U.G., Henry, J.P., Schwarz, R.A., Böhringer, H., Ebeling, H., Edge, A.C., Hartner, G.D., Schindler, S., Trümper, J. & Voges, W., 1991, *Astr. & Astrophys.*, **246**, L10.

Byram, E.T., Chubb, T.A. & Friedman, H., 1966, *Science*, **152**, 66

Canizares, C.R., Clark, G.W., Markert, T.H., berg, C., Smedira, M., Bardas, D., Schnopper, H. & Kalata, K., 1979, *Astrophys. J. (Letters)*, **234**, L33.

Canizares, C.R., Markert, T.H. & Donahue, M.E., 1988, in *"Cooling flows in Clusters and Galaxies"*, ed A. C. Fabian, Kluwer, p63.

Carr, B.J., Bond, J.R. & Arnett, W.D., 1984, *Astrophys. J.*, **277**, 445.

Carrera, F.J., Barcons, X., Butcher, J.A., Fabian, A.C., Stewart, G.C., Warwick, R. S., Hayashida, K. & Kii, T., 1991, *Mon. Not. R. astr. Soc.*, **249**, 698..

Carrera, F.J., Barcons, X., Butcher, J.A., Fabian, A.C., Stewart, G.C., Toffolatti, L., Warwick, R.S., Hayashida, K., Inoue, H. & Kondo, H., 1993, *Mon. Not. R. astr. Soc.*, **260**, 376.

Cavaliere, A. & Fusco-Fermiano, R., 1978, *Astr. & Astrophys.*, **49**, 137.

Chanan, G.A. & Abramopoulos, F., 1984, *Astrophys. J.*, **287**, 89.

Colless, M., 1989, *Mon. Not. R. astr. Soc.*, **237**, 799.

Condon, J.J., 1974, *Astrophys. J.*, **188**, 279.

Cowie, L.L., Henriksen, M. & Mushotzky, R.F., 1987, *Astrophys. J.*, **317**, 593.

Cowsik, R. & Kobetich, E.J., 1972, *Astrophys. J.*, **177**, 585.

Danese, L., De Zotti, G., Andreani. P., 1992, in *"The X-ray Background"*, eds X. Barcons & A. C. Fabian, CUP, Cambridge, p61

Daly, R.A., 1991, *Astrophys. J.*, **379**, 37.

David, L.P., Arnaud, K.A., Forman, W. & Jones, C., 1990a, *Astrophys. J.*, **356**, 72.

David, L.P., Forman, W. & Jones, C., 1990b, *Astrophys. J.*, **359**, 29.

David, L.P., Forman, W. & Jones, C., 1991a, *Astrophys. J.*, **369**, 121.

David, L.P., Forman, W. & Jones, C., 1991b, *Astrophys. J.*, **380**, 39.

Davison, P.J.N., 1978, *Mon. Not. R. astr. Soc.*, **183**, 39p.

Della Ceca, R., Maccacaro, T., Gioia, I.M., Wolter, A. & Stocke, J.T., 1992, *Astrophys. J.*, **389**, 491.

de Robertis, M.M. & Yee, H.K.C., 1990, *Astr. J.*, **100**, 84.

de Vaucouleurs, G., 1948, *Contrib. Inst. Astrophys. Paris A*, No. 27.

de Young, D.S., 1978, *Astrophys. J.*, **223**, 47.

Dressler, A. & Schectman, S., 1988, *Astr. J.*, **95**, 985.

Edge, A.C., 1989 PhD Thesis, University of Leicester

Edge, A.C., Stewart, G.C., Fabian, A.C. & Arnaud, K.A., 1990, *Mon. Not. R. astr. Soc.*, **245**, 559.

Edge, A.C., 1991, *Mon. Not. R. astr. Soc.*, **250**, 103.

Edge, A.C. & Stewart, G.C., 1991a, *Mon. Not. R. astr. Soc.*, **252**, 414.

Edge, A.C. & Stewart, G.C., 1991b, *Mon. Not. R. astr. Soc.*, **252**, 428.

Edge, A.C., Stewart, G.C. & Fabian, A.C., 1992, *Mon. Not. R. astr. Soc.*, **258**, 177.

Ellis, G.F.R., Skea, J.E.F. & Tavakol, R.K., 1991, *Phys. Lett. B*, **271**, 52

Elvis, M., Soltan, A. & Keel, W.C., 1984, *Astrophys. J.*, **283**, 479.

Eyles, C.J., Watt, M.P., Bertram, D., Church, M.J. & Ponman, T.J., 1991, *Astrophys. J.*, **376**, 23.

Faber, S.M. & Gallagher, 1976, *Astrophys. J.*, **204**, 365.

Faber, S.M. & Gallagher, 1979, *Ann. Rev. Astr. Astrophys.*, **17**, 135.

Fabian, A.C., 1975, *Mon. Not. R. astr. Soc.*, **172**, 249.

Fabian, A.C. & Rees, M.J., 1978, *Mon. Not. R. astr. Soc.*, **185**, 109.

Fabian, A.C., Hu, E.M., Cowie, L.L. & Grindlay, J., 1981, *Astrophys. J.*, **248**, 47.

Fabian, A.C., Canizares, C.R. & Barcons, X., 1989, *Mon. Not. R. astr. Soc.*, **239**, 15.

Fabian, A.C., George, I.M., Miyoshi, S. & Rees, M.J., 1990, *Mon. Not. R. astr. Soc.*, **242**, 14p.

Fabian, A.C., Nulsen, P.E.J. & Canizares, C.R., 1991, *Astron. Astrophys. Rev.*, **2**, 191.

Fabian, A.C. & Daines, S.J., 1991, *Mon. Not. R. astr. Soc.*, **252**, 17p.

Fabbiano, G., 1989, *Ann. Rev. Astron. Astroph.*, **27**, 87.

Fabricant, D. & Gorenstein, P,. 1983, *Astrophys. J.*, **267**, 535.

Feretti, L., Perola, G.C. & Fanti, R., 1992, *Astr. & Astrophys.*, **265**, 9.

Field, G.B. & Perrenod, S.C., *Astrophys. J.*, **215**, 717.

Fink, H.H., Thomas, H.-C., Brinkmann, W., Okayasu, R. & Hartner, G., 1992 in *X–ray emission from Active Galactic Nuclei and the Cosmic X–ray Background*, eds Brinkmann, W. & Trumper, J., MPE report 235, p202.

Fitchett, M. & Webster, R., 1987, *Astrophys. J.*, **317**, 653.

Fitchett, M.J., 1990, in *Clusters of Galaxies*, proc. 4th Space Telescope Science Institute Symposium, eds. Oegerle, W.R., Fitchett, M.J. & Danly, L., p111.

Forman, W., Jones, C., Murray, S. & Giacconi, R., 1978 *Astrophys. J. (Letters)*, **225**, L1.

Fukazawa, Y., Makishima, K., Ebisawa, K., Fabian, A.C., Gendreau, K. & Ikebe, Y., 1994, *Publ. astr. Soc. Japan*, 46L,

.George, I.M. & Fabian, A.C., 1991, *Mon. Not. R. astr. Soc.*, 249, 352.

Giacconi, R., Gursky, H. & Paolini, F., 1962, *Phys. Rev. Lett.* 9, 439.

Giacconi, R., Murray, S., Gursky, H, Kellogg, E., Schreier, E., & Tananbaum, H., 1972, *Astrophys. J.*, 178, 281.

Giacconi, R., Murray, S., Gursky, H, Kellogg, E., Schreier, E., Matilsky, T., Koch, D. & Tananbaum, H., 1974, *Astrophys. J. Suppl.*, 27, 37.

Giacconi, R., *et al.*, 1979a, *Astrophys. J.*, 230, 540.

Giacconi, R., *et al.*, 1979b, *Astrophys. J. (Letters)*, 234, L1.

Giacconi, R. & Zamorani, G., 1987, *Astrophys. J.*, 313, 20.

Gioia, I.M., Maccacaro, T., Schild, R.E., Wolter, A., Stocke, J.T., Morris, S.L. & Henry, J.P., 1990a, *Astrophys. J. Suppl.*, 72, 567.

Gioia, I.M., Henry, J.P., Maccacaro, T., Morris, S.L., Stocke, J.T. & Wolter, A., 1990b, *Astrophys. J.*, 356, L35.

Griffiths, R.E., Tuohy, I.R., Brissenden, R.J.V., Ward, M., Murray, S.S. & Burg, R., 1988, in *Proc. of a Workshop on optical Surveys for Quasi Stellar Objects*, eds. Osmer *et al.*, *Pub. Astron. Soc. Pacific*

Griffiths, R.E. & Padovani, P., 1990, *Astrophys. J.*, 360, 483.

Gruber, D.E., *et al.*, 1984, in *X-Ray and UV emission from Active Galactic Nuclei*, eds Brinkmann, W. & Trumper, J. MPE Report 184, 129.

Gruber, D.E., Rephaeli, Y. & Persic, M., 1992, in *"The X-ray Background"*, eds X. Barcons & A. C. Fabian, CUP, Cambridge, p169

Guilbert, P.W. & Fabian, A.C., 1986, *Mon. Not. R. astr. Soc.*, 220, 439.

Gunn, J.E. & Gott, J.R., 1972, *Astrophys. J.*, 176, 1.

Gursky, H., Kellogg, E.M., Murray, S., Leong, C., Tananbaum, H. & Giacconi, R., 1971a, *Astrophys. J.*, 165, L43.

Gursky, H., Kellogg, E.M, Leong, C., Tananbaum, H. & Giacconi, R., 1971b, *Astrophys. J. (Letters)*, 167, L81.

Hamilton, T.T. & Helfland, D.J., 1987, *Astrophys. J.*, 318, 93.

Hamilton, T.T., Helfland, D.J. & Wu, X., 1991, *Astrophys. J.*, 379, 576.

Hanson, C.G., Skinner, G.K., Eyles, C.J. & Willmore, A.P., 1990, *Mon. Not. R. astr. Soc.*, 242, 262.

Hammer, F., 1991, *Astrophys. J.*, 383, 66.

Hasinger, G., Schmidt, M. & Trumper, J., 1991, *Astr. & Astrophys.*, 246, L2.

Hasinger, G., 1992, in *"The X-ray Background"*, eds X. Barcons & A. C. Fabian, CUP, Cambridge, p229

Hatsukade, I., 1989, PhD, Osaka University.

Hayashida, K., 1989, PhD, University of Tokyo.

Hayashida, K., Inoue, H., Koyama, K., Awaki. H., Takano, S., Tawara, Y., Williams, O.R., Denby, M., Stewart, G.C., Turner, M.J.L., Makishima, K. & Ohashi, T., 1989, *Publ. astr. Soc. Japan*, 41, 373.

Hayashida,K., Inoue, H. & Kii, T., 1992,In: *Frontiers of X-ray astronomy'*, ed Koyama, K. & Tanaka, Y., Univ. Acad. Press, p653.

Henriksen, M.J. & Mushotzky, R.F., 1985, *Space Science Rev.*, Vol 40, 681

Henriksen, M.J & Mushotzky, R.F, 1986, *Astrophys. J.*, **302**, 287.

Holt, S., Kaluzienski, L., Boldt, E. & Serlemitsos, P., 1979, *Astrophys. J.*, **233**, 344.

Hughes, J.P., Gorenstein. P. & Fabricant, D., 1988, *Astrophys. J.*, **329**, 82.

Hughes, J.P., Yamashita, K., Okumura, Y., Tsunemi, H. & Matsuoka, M., 1988, *Astrophys. J.*, **327**, 615.

Hughes, J.P., 1989, *Astrophys. J.*, **337**, 21.

Hughes, J.P., Butcher, J.A., Stewart, G.C. & Tanaka, Y., 1993, *Astrophys. J.*, **404**, 611.

Hughes, J.P. & Birkinshaw, M., 1994, *Astrophys. J.*, **420**, 33.

Iwan, D., Marshall, F.E., Boldt, E.A., Mushotzky, R.F., Shafer, R.A & Stottlemyer, A., 1982, *Astrophys. J.*, **260**, 111.

Jaffe, W., 1992, in *"Clusters and Superclusters of Galaxies"*, ed A. C. Fabian, Kluwer, p109.

Johnstone, R.M, Fabian, A.C. & Nulsen, P.E.J., 1987, *Mon. Not. R. astr. Soc.*, **224**, 75.

Johnstone, R.M., Fabian, A.C., Edge, A.C. & Thomas, P.A., 1992, *Mon. Not. R. astr. Soc.*, **258**, 177.

Jones, C. & Forman, W., 1984, *Astrophys. J.*, **276**, 38.

Kellogg, E.M., Gursky, H., Tananbaum, H., Giacconi, R. & Pounds, K.A., 1972, *Astrophys. J. (Letters)*, **174**, L65.

King, I.R., 1962, *Astr. J.*, **67**, 471.

Kowalski, M.P., Ulmer, M.P. & Cruddace, R.G., 1983, *Astrophys. J.*, **268**, 540.

Kowalski, M.P., Ulmer, M.P. & Cruddace, R.G. & Wood, K.S., 1983, *Astrophys. J. Suppl.*, **56**, 403.

Kowalski, M.P., Cruddace, R.G., Snyder, W.A., Fritz, G.G., Ulmer, M.P. & Fenimore, E.E., 1993 *Astrophys. J.*, **412**, 489.

Lampton, M., Margon, B. & Bower, S., 1976, *Astrophys. J.*, **208**, 177.

Lasenby, A.N., 1992, in *"Clusters and Superclusters of Galaxies"*, ed A. C. Fabian, Kluwer, p219.

Lea, S.M., Reichert, G., Mushotzky, R., Baity, W.A., Gruber, D.E., Rothschild, R.E. & Primini, F.A., 1981, *Astrophys. J.*, ,, 246. 369

Lea, S.M., Mushotzky, R.F. & Holt, S.S., 1982, *Astrophys. J.*, **262**, 24. Rothschild, R. & Primini, F.A., 1981, *Astrophys. J.*, **246**, 369.

Lynden-Bell, D., 1967, *Mon. Not. R. astr. Soc.*, **136**, 101.

Lynds, R. & Petrosian, V., 1986, *Bull. Am. Astron. Soc.*, **18**, 1014

Maccacaro. T., *et al.*, 1982, *Astrophys. J.*, **253**, 504.

Maccacaro, T., Gioia, I.M., Maccagni, D. & Stocke, J.T., *Astrophys. J.*, **284**, L23.

Maccacaro, T., Della Ceca, R., Gioia, I.M., Morris, S.L. & Stocke, J.T., 1991, *Astrophys. J.*, **369**, 314.

Madau, P., Ghisellini, G. & Fabian, A.C., 1994, *Mon. Not. R. astr. Soc.*, L17,

.Madsen, M.S. & Ellis, G.F.R., 1988, *Mon. Not. R. astr. Soc.*, **234**, 67.

Madsen, M.S., Mimoso, J.P., Butcher, J.A. & Ellis, G.F.R., 1992, *Phys. Rev. D*, **46**, 1399.

Makino, F. & the ASTRO-C team, 1987, *Astrophys. Lett. & Comm.*, **25**, 223.

Marshall, F.E., Boldt, E.A., Holt, S.S., Miller, R.B., Mushotzky, R.F., Rose, L.A., Rothschild, R.E & Serlemitsos, P.J, 1980, *Astrophys. J.*, **235**, 4.

Masai, K., 1984, *Astrophys. & Space Science.*, **98**, 367.

Mather, J.C., *et al.*, 1990, *Astrophys. J.*, **354**, L37.

Matteuci,F. & Vettolani, G., 1988, *Astr. & Astrophys.*, **202**, 21.

McHardy, I.M., 1979, *Mon. Not. R. astr. Soc.*, **188**, 495.

McHardy, I.M., Stewart, G.C., Edge, A.C., Cooke, B., Yamashita, K. & Hatsukade, I., 1990, *Mon. Not. R. astr. Soc.*, **242**, 215.

Merritt, D., 1987, *Astrophys. J.*, **313**, 121.

Mewe, R., Gronenschild, E.H.B.M. & van den Oord, H.J., 1985 *Astr. & Astrophys. Supp.*, **62**, 197.

Mewe, R., Lemen, J.R. & van den Oord, H.J., 1986 *Astr. & Astrophys. Supp.*, **56**, 511.

Micela, G., Sciortino, S., Vaiana, G.S., Harnden, F.R. & Rosner, R., 1991, *Astrophys. J.*, **380**, 495.

Mitchell, R.J., Culhane, J.L., Davison, P.J. & Ives, J.C., 1976, *Mon. Not. R. astr. Soc.*, **176**, 29p.

Mitchell, R. & Mushotzky, R., 1980, *Astrophys. J.*, **236**, 730.

Montle, R.E., 1973, M.A. Thesis, Vanderbilt University, Nashville, Tennessee.

Morris, S.L., Stocke, J.T., Gioia, I.M., Schild, R.E., Wolter, A., Maccacaro, T. & Della Ceca, R., 1991, *Astrophys. J.*, **380**, 49.

Murakami, T., Fujii, M., Hayashida, K., Itoh, M., Nishimura, J., Yamagami, T., Yoshida, A., Conner, J.P., Evans, W.D., Fenimore, E.E., Klebesadel, R.W., Spencer, K.M., Murakami, H., Kawai, N., Kondo, I. & Katoh, M., 1989, *Publ. astr. Soc. Japan*, **41**, 405.

Mushotzky, R.F., Holt, S.S., Smith, B.W., Boldt, E.A. & Serlemitsos, P.J., 1981, *Astrophys. J. (Letters)*, **244**, L47.

Mushotzky, R.F., 1984, *Physica Scripta*, **T7**, 157.

Mushotzky, R.F., 1984b, *Adv. Space Res.*, **3**, 10.

Mushotzky, R.F. & Szymkowiak, A.E., 1988, in *"Cooling flows in Clusters and Galaxies"*, ed A. C. Fabian, Kluwer, p47.

Mushotzky, R.F., 1990, 1989, in *"Two topics in X–ray astronomy. Vol. 2: AGN and the X–ray background"*, Proceedings of the 23rd ESLAB sypmosium, (European Space Agency, Paris), p857

Mushotzky, R., 1992, in *"Clusters and Superclusters of Galaxies"*, ed A. C. Fabian, Kluwer, p91.

Mushotzky, R.F., & Jahoda, K., 1992, in *"The X–ray Background"*, eds X. Barcons & A. C. Fabian, CUP, Cambridge, p80

Nandra, K., 1992 PhD Thesis, University of Leicester

Nomoto, K., Thielemann, F-.K & Yokoi, K., 1984, *Astrophys. J.*, **286**, 644.

Nulsen, P.E., Stewart, G.C., Fabian, A.C., Mushotzky, R.F., Holt, S.S., Ku, W. & Malin, D, 1982, *Mon. Not. R. astr. Soc.*, **109**, 1089.

Ohashi, T., Makishima, K., Tsuru, T., Takano, S., Koyama, K. & Stewart, G.C., 1990, *Astrophys. J.*, **365,** 180.

Olive, K.A., Schramm, D.N., Steigman, G. & Walker, T.P., 1990, *Phys. Lett. B*, **236**, 454.

Osborne, J.P., Beardmore, A.P., Wheatley, P.J., Hakala, P., Watson, M.G., Mason, K.O., Hassall, B.J.M. & King, A.R., 1994, *Mon. Not. R. astr. Soc.*, **270**, 650.

Penzias, A.A. & Wilson, R.W., 1965, *Astrophys. J.*, **142**, 419.

Persic, M., De Zotti, G., Boldt, E.A., Marshall, F.E., Danese, L., Franceschini, A. & Palumbo, G.G.C., 1989, *Astrophys. J.*, **253**, L47.

Piccinotti, G., Mushotzky, R.F., Boldt, E.A., Holt, S.S., Marshall, F.E., Serlemitsos, P.J. & Shafer R.A., 1982, *Astrophys. J.*, **253**, 485.

Ponman, T.J., Bertram, D., Church, M.J., Eyles, C.J., Watt, M.P., Skinner, G.K. & Willmore, A.P., 1990, *Nature*, **347**, 450.

Pounds, K.A., Nandra, K., Stewart, G.C., George, I.M. & Fabian, A.C., *Nature*, **344**, 132.

Press, W., Teukolsky, S.A., Vetterling, W.T. & Flannery, B.P., 1992, *Numerical Recipes*, CUP.

Raymond, J.C. & Smith, B.W., 1977, *Astrophys. J. Suppl.*, **35**, 419.

Rees, M.J., 1992, in *"Clusters and Superclusters of Galaxies"*, ed A. C. Fabian, Kluwer, p1.

Reichert, G.A., Mushotzky, R.F., Petre, R. & Holt, S.S., 1985, *Astrophys. J.*, **296**, 69.

Rogers, R.D.& Field, G.B., 1991, *Astrophys. J. (Letters)*, **370**, L57.

Rothenflug, R. & Arnaud, M., 1985, *Astr. & Astrophys.*, 144, 431.

Rothschild, R., Boldt, E., Holt, S., Sermelitsos, P., Garmire, G., Agrawal, P., Riegler, G., Bowyer, S. & Lampton, M., 1979 *Space Sci. Instrum.*, 4, 269.

Rothschild, R., 1992, in *"The X–ray Background"*, eds X. Barcons & A. C. Fabian, CUP, Cambridge, p291

Sarazin, C.L., 1988, *X–ray emissions from clusters of galaxies*, Cambridge University Press, Cambridge.

Schmidt, M. & Green, R.F., 1983, *Astrophys. J.*, **269**, 352.

Sermelitsos, P.J., Smith, B.W., Boldt, E.A., Holt, S.S. & Swank, J.H., 1977, *Astrophys. J. (Letters)*, **211**, L63.

Serlemitsos, P.J., Marshall, F.E., Petre, R., Jahoda, K., Boldt, E.A., Holt, S.S., Mushotzky, R.F., Swank, J., Szymkowiak, A., Kelley, R. & Loewenstein, M., 1992, In: *Frontiers of X-ray astronomy'*, ed Koyama, K. & Tanaka, Y., Univ. Acad. Press, p221.

Scheuer, P.A.G., 1957 , *Proc. Camb. Phil. Soc.*, **53**, 764.

Scheuer, P.A.G., 1974, *Mon. Not. R. astr. Soc.*, **166**, 239.

Schwartz, D.A., 1979, In *X-ray Astronomy: Proc 21st COSPAR*, eds. Baity & Peterson, Pergamon, NY, p453

Schwartz, D.A. & Tucker, W.H., 1988, *Astrophys. J.*, **332**, 157.

Serlemitsos, P.J., Smith, B.W., Boldt, E.A., Holt, S.S. & Swank, J.H., 1977, *Astrophys. J. (Letters)*, **211**, L63.

Setti, G., 1990, in *The Galactic and Extragalactic background radiation*, ed. Bowyer & Leinert, Reidel.

Shafer, R.A., 1983, Ph.D dissertation, University of Maryland, NASA TM 85029

Shanks, T., Georgantopoulous, I., Stewart, G.C., Pounds, K.A., Boyle, B.J & Griffiths, R., 1991, *Nature*, **353**, 6342

Singh, K.P., Westergaard, N.J. & Schnopper, H.W., 1988, *Astrophys. J.*, **330**, 620.

Soltan, A. & Fabricant, D.G., 1990, *Astrophys. J.*, **364**, 433.

Soucail, G., Fort, B., Mellier, Y. & Picat, J.P., 1987, *Astr. & Astrophys.*, **190**, L11.

Soucail, G., 1992, in *"Clusters and Superclusters of Galaxies"*, ed A. C. Fabian, Kluwer, p199.

Stark et al. 1991

Stewart, G.C., Fabian, A.C¿, terlevich, R.J. & Hazard. C., 1982, *Mon. Not. R. astr. Soc.*, **200**, 61p.

Stewart, G.C., Fabian, A.C., Jones, C. & Forman, W., 1984, *Astrophys. J.*, **285**, 1.

Sunyaev, R.A. & Zel'dovich, Y.B., 1972, *Comm. Astrophys. Space phys.*, **4**, 173

Takano, S. & Koyama, K., 1991, *Publ. astr. Soc. Japan*, **43**, 1.

Takase, B. & Miyauchi-Isobe, N., 1991, *Pub. Nat. Astron. Obs. Japan*, **2**, 239.

Tonry, J.L., 1985, *Astr. J.*, **90**, 2341.

Trinchieri, G. & Fabbiano, G., 1985, *Astrophys. J.*, **296**, 447.

Tsunemi, H., Kitamoto, S., Manabe, M., Miyamoto, S., Yamashita, K. & Nakagawa, M., 1989, *Publ. astr. Soc. Japan*, **41**, 345.

Turner, M.J.L., Smith, A. & Zimmermann, H.U., 1981 *Space Sci. Rev.* **30**, 513.

Turner, T.J. & Pounds, K.A., 1989, *Mon. Not. R. astr. Soc.*, **240**, 833.

Turner, M.J.L., Thomas, H.D., Patchett, B.E., Reading, D.H., Makishima, K., Ohashi, T., Dotani, T., Hayashida, K., Inoue, H., Kondo, H., Koyama, K., Mitsuda, K., Ogawara, Y., Takano, S., Awaki, H., Tawara. Y. & Nakamura. N., 1989. *Publ. astr. Soc. Japan*, **41**, 345.

Tsuru, T., 1993, PhD, Kyoto University.

Tyson, J.A., 1984, in *IAU Symposium 78, Astronomy with Schmidt type telescopes*, ed. Capaccioli, Reidel.

Tyson, J.A., Valdes, F. & Wenk, R.A., 1990, *Astrophys. J. (Letters)*, **249**, L1.

Ueno, S., Koyama, K., Nishida, M., Yamauchi, S. & Ward, M.J., 1994, *Astrophys. J. (Letters)*, **431**, L1.

Ulmer, M.P., Cruddace, R.G., Fenimore, E.E., Fritz, G.G. & Snyder, W.A., 1987, *Astrophys. J.*, **319**, 118.

van den Bergh, S., McClure, R.D. & Evans, R., 1987, *Astrophys. J.*, **323**, 44.

Warwick, R.S. & Pye, J.P., 1978, *Mon. Not. R. astr. Soc.*, **183**, 833.

Warwick, R.S., & Stewart, G.C., 1990, 1989, in *"Two topics in X-ray astronomy. Vol. 2: AGN and the X-ray background"*, Proceedings of the 23rd ESLAB sypmosium, (European Space Agency, Paris), p727

Warwick, R.S. & Butcher, J.A., 1992, In: *Frontiers of X-ray astronomy'*, ed Koyama, K. & Tanaka, Y., Univ. Acad. Press, p641.

Watt, M.P., Ponman, T.J., Bertram, D., Eyles, C.J., Skinner, G.K. & Willmore, A.P., 1992, *Mon. Not. R. astr. Soc.*, **258**, 738.

Weinberg,S.,1972, *Gravitation and Cosmology : Principles & Applications of the General Theory of Relativity*, J.Wiley, N.Y

White, N.E. & Peacock, A., 1988, *Mem. Soc. Astr. Ita.*, **59** 7.

White, D.A., Fabian, A.C., Johnstone, R.M., Mushotzky, R.F. & Arnaud, K.A., 1991, *Mon. Not. R. astr. Soc.*, **252**, 72.

White, S.D.M., 1992, in *"Clusters and Superclusters of Galaxies"*, ed A. C. Fabian, Kluwer, p17.

Williams, O.R., Turner, M.J.L., Stewart, G.C., Saxton, R.D., Ohashi, T., Makishima, K., Kii, T., Inoue, H., Makino, F., Hayashida, K. & Koyama, K., 1992, *Astrophys. J.*, **389**, 157.

Wise, M.W., O'Connell, R.W., Bregman, J.N. & Roberts, M.S., 1993, *Astrophys. J.*, **405**, 94.

Wolf,M., 1906, *Astron. Nachr.*, **170**, 211.

Worrall, D.M. & Marshall, F.E., 1983, *Astrophys. J.*, **267**, 691.

Wu, X., Hamilton, T., Helfland, D.J & Wang, Q., 1991, *Astrophys. J.*, **379**, 564.

Zwicky, F., 1933, *Helvetica Physica Acta*, **6**, 110.

Acknowledgements